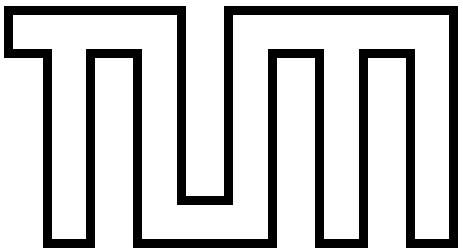

Technische Universität
München

Development of the compact, high resolution particle detection system HI-TREX

PhD Thesis by Christian Berner

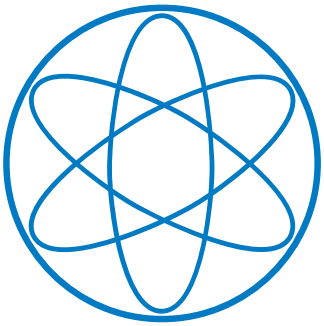

Lehrstuhl E68 für Nukleare Astrophysik

10. März 2020

TECHNISCHE UNIVERSITÄT
MÜNCHEN
Physik-Department ENA Nukleare Astrophysik

Development of the compact, high resolution particle detection system HI-TREX

Christian Stefan Berner

Vollständiger Abdruck der von der Fakultät für Physik der Technischen Universität München zur Erlangung des akademischen Grades eines

Doktors der Naturwissenschaften (Dr. rer. nat.)

genehmigten Dissertation.

Vorsitzender:		apl. Prof. Dr. Norbert Kaiser
Prüfer der Dissertation:	1.	Prof. Dr. Shawn Bishop
	2.	Prof. Dr. Lothar Oberauer

Die Dissertation wurde am 01.07.2020 bei der Technischen Universität München eingereicht und durch die Fakultät für Physik am 14.09.2020 angenommen.

Contents

Zusammenfassung

Transferreaktionen stellen eine einzigartige Möglichkeit dar, die Struktur von Kernen zu untersuchen. In zahlreichen Experimenten mit stabilen Schwerionenstrahlen wurde in den letzten Jahrzehnten die Einteilchenstruktur von astrophysikalisch relevanten Kernen erfolgreich erforscht. Bereits früh erkannte man die Notwendigkeit auch radioaktive, exotische Kerne zur Untersuchung von kosmologischen Vorgängen, wie die der Elemententstehung im Universum zu produzieren. In herausragender Weise kann dies an der HIE-ISOLDE Forschungsanlage am CERN erprobt werden. Eine Reihe erfolgreicher Transferexperimenten in leichten Systemen wurde mit dem Siliziumdetektor TREX, gekoppelt an das Photonenspektrometer MINIBALL durchgeführt. Durch das Energie- und Intensitätsupgrade der ISOLDE-Anlage werden nun erstmals auch Transferreaktionen in schweren Systemen ermöglicht. Dies erfordert einen verbesserten Siliziumaufbau, der in der Lage ist diese schweren, neutronenreichen Strahlen mit Energien von bis zu 10 MeV/u zu detektieren.

Im Rahmen dieser Arbeit wurde das Ein-Neutronen Transferexperiment d(^{134}Sn,p)^{135}Sn bei einer Strahlenergie von 7.3 MeV/u durchgeführt, um die besondere Notwendigkeit einer Anpassung des Siliziumaufbaus zu zeigen. Hierbei zielte das Experiment auf die experimentelle Bestimmung von bisher noch unbekannten, angeregten Zuständen in ^{135}Sn. Es konnte gezeigt werden, dass der die radioaktiven Strahlen begleitende Elektronenuntergrund durch den Einsatz hochsegmentierter, doppelseitiger Siliziumstreifendetektoren stark unterdrückt werden kann. Außerdem wurde die Teilchenidentifikation unter Vorwärtswinkeln gesondert berücksichtigt, sowie die Anforderungen an die Auflösung der Ausleseelektronik. Letztere spielt eine besondere Rolle bei Experimenten in inverser Kinematik, da bei diesen die kinematische Kompression der Transferzustände in Rückwärtsrichtung einen außerordentlich großen Einfluss auf die Unterscheidbarkeit der bevölkerten, angeregten Zustände hat.

Anhand von umfangreichen Simulationen wurde der hochintegrierte Teilchendetektor HI-TREX entworfen. Die Entwicklung der beiden Hauptkomponenten des Systems war eng miteinander verwoben: Die eigens entwickelten, extrem dünnen, AC-gekoppelten, doppelseitigen Siliziumdetektoren und die ASIC-basierte Elek-

tronik, die in der Lage ist, hochauflösend die 1944 Kanäle des Systems auszulesen. Die Einbindung der verwendeten SKIROC2 ASICs erfolgte durch die ebenfalls in dieser Arbeit entwickelte, generische ASIC-Ausleseplattform GEAR. In einem Experiment am Münchner Tandembeschleuniger MLL wurde ein Prototyp für den finalen HI-TREX Aufbau mit einem Schwerionenstrahl erfolgreich erprobt. Die Eigenschaften dieser integrierten Elektronik sind hervorragend: Eine Rauschladungszahl von $7.9 \pm 0.08\,\mathrm{keV}$ wurde gemessen, zusammen mit der Energieauflösung bei einem mit der Ausleseelektronik gekoppeltem Silizumdetektor von $FWHM = 26.9 \pm 0.3\,\mathrm{keV}$.

Der kompakte, hochauflösende Aufbau des Teilchendetektors HI-TREX wurde unter Verwendung von sehr spezialisierter Technologie als einfach zu skalierendes System entwickelt. Dies ermöglicht die vielseitige Verwendung des Detektors in unterschiedlichsten kernphysikalischen Experimenten.

Abstract

Transfer reactions are a unique tool to populate and probe the structure of nuclei. Various experiments studying single-particle properties have been successfully conducted with stable, heavy ion beams throughout the last decades. The necessity of producing radioactive, exotic nuclei for the investigation of cosmological processes, such as the formation of elements in the universe, was recognised early on. The HIE-ISOLDE facility at CERN provides unprecedented capabilities in producing these exotic beams. Whole series of successful transfer experiments with light, radioactive beams have been performed with the TREX silicon detector in conjunction with the γ-detector array MINIBALL. With the advent of the energy and intensity upgrade of the ISOLDE-facility, transfer experiments with medium and heavy systems came into reach. This requires an adapted silicon setup being able to cope with these heavy, neutron-rich beams with energies as high as 10 MeV/u.

Within this work, the necessity of upgrading the silicon detector array was demonstrated in the one-neutron transfer experiment d(^{134}Sn,p)^{135}Sn at 7.3 MeV/u beam energy. The experiment was aiming at the first determination of excited states in ^{135}Sn. Much experience was gained in understanding the electron background accompanying high-Z radioactive beams. It was shown, that the use of highly segmented double sided silicon strip sensors (DSSSDs) solves this issue. The importance of a proper particle identification in the forward laboratory angles was emphasised as well as the need to have a low-noise electronics readout with good resolution, especially in the backward region, in order to account for the kinematical compression of the transfer states in inverse kinematics.

These experiences ensued a thorough analysis of the requirements for a particle detection setup and led with the results of extensive simulations to the upgraded, highly integrated successor HI-TREX. The main upgraded components are closely linked with each other: The silicon detector upgrade utilising newly developed, very thin, AC-coupled DSSSDs and the accompanying custom made, ASIC-based electronics, processing the 1944 detector signals of the system. The integration of SKIROC2 ASICs has been done successfully by the GEneric Asic Readout board GEAR, which also was developed within this work. The back-end integration,

as well as the development of any peripheral components resulted in a working prototype for the full HI-TREX setup, which has been successfully tested at the Munich tandem facility MLL with a heavy-ion beam. The performance of this high-density, integrated electronics is superb: 7.9 ± 0.08 keV equivalent noise charge has been evaluated and in conjunction with a silicon detector an energy resolution of $FWHM = 26.9 \pm 0.3$ keV was achieved.

The highly integrated particle detection system HI-TREX makes use of high-level technological developments and was designed for a generic purpose and hence provides maximum flexibility and scalability for a wide range of nuclear physics experiment.

CHAPTER I

Quest for new development

George Gamow, a nuclear physics pioneer, believed that all the elements were produced in the Big Bang. This was a sensible deduction based on the knowledge of the 1940s. Already in 1952, the discovery of technetium in certain red giant stars [61] refuted Gamov's thesis - at least partially. Technetium is the first chemical element, which has been produced artificially and the lightest element whose isotopes are all radioactive. The isotope with the longest half-live of 4.21×10^6 yr is ^{97}Tc [30]. This short-lived element could not have been made in the Big Bang, so some elements must be produced in stars. Gamov's thesis however was not entirely wrong, as today's mass composition of the universe is roughly 74% hydrogen, 24% helium and only about 2% everything else. Hydrogen, most of the helium and some lithium (and very little beryllium - although only the radioactive isotope ^{7}Be) were produced in the Big Bang Nucleosynthesis [59], and it is only the remaining 2% that Gamov was wrong about.

Todays understanding of elemental formation, that is the processes forming all these 2% of 'heavy' elements is partly depicted in figure I.1. It is nuclear physics that plays a special role in the cosmos; every visible thing in the night sky is driven by nuclear reactions. It is nuclear physics that governs the evolution of stars from birth to their final state and hence provides almost all the energy we receive from the sun. The starting point in elemental formation (the very left point in the Segrè chart) is the fusion of two protons, which requires three of the four fundamental forces acting together against the repulsion of the electromagnetic force: The gravitational force first compresses the hydrogen gas, raising its temperature and thus providing the necessary energy to the protons to tunnel together. Next, the strong force keeps the protons close together, while the weak force turns one proton into a neutron, allowing to form the stable deuterium. Further fusion processes in stars like the

pp-chain, triple-alpha process, CNO cycle and the various shell burning stages then produce all the elements up to ^{56}Fe. Although ^{62}Ni has a somewhat higher binding energy per nucleon ($B_E/A = 8.795\,\text{MeV}$ [30]), it cannot be produced efficaciously in single, or sequential fusion reactions in old stars synthesising heavy elements [82].

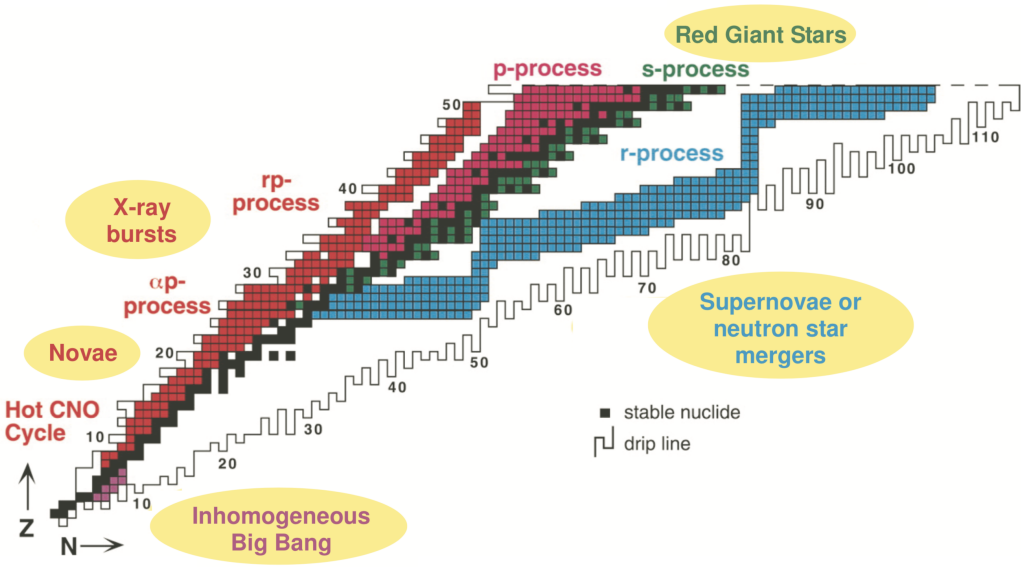

Figure I.1: Excerpt of the Segrè chart with various nucleosynthetic processes indicated. Representative astrophysical environments for the processes are shown as well. Combinations of these processes result in the abundance distribution of the chemical elements we observe today. Figure adapted from [83]

All nuclei heavier than ^{62}Ni have lower binding energies and thus must have been created in different ways than fusion in stars. One process, occuring in asymptotic giant branch stars, is the *s*-process (depicted in green and also in black in figure I.1), a sequence of slow neutron captures and much faster β-decays. It can produce elements up to lead, respectively bismuth. The *s*-process is intimately linked to mixing processes in stars, as the only plausible way to produce the neutrons is the mixing between hydrogen burning and helium burning, as ^{13}C and ^{22}Ne act as strong neutron sources, when immersed in helium rich environments. It is the uncertainties in the (α, n) reactions of these two isotopes, that remain the main limitations to understand mixing processes in stars [79]. A strong evidence for the *s*-process to occur in red giant stars is again the observation of technetium on their surface. However, only about half of the stable elements heavier than iron can be made up in the *s*-process. The others, in particular the isotopes of uranium and thorium being present on earth must have been created elsewhere.

Briefly, the p-process creating the mostly very rare nuclei on the proton-rich side beyond the iron peak needs to be mentioned. Astrophysical sites are core collapse and thermonuclear supernovae. A comprehensive review of the p-process can be found in [75]. However, the contribution of the p-process to heavy element synthesis is about one to two orders of magnitude lower than the *s*- or the *r*-process [9].

This later process of rapid neutron capture is usually denoted as *r*-process. Unlike for the *s*-process, the *r*-process site has not been determined with certainty and a large number of models are therefore discussed in literature. An excellent topical review on the *r*-process nucleosynthesis can be found in [45]. Core-collapse supernovae, neutron star mergers like *GW170817* [1], their ejecta and neutrino-driven winds are only some possible locations of the *r*-process. The presence of strontium in the kilonova *AT2017gfo* emerging the *GW170817* event is the first identification of freshly-synthesised *r*-process elements in an astrophysical site. Furthermore the results suggest that neutron stars comprise neutron-rich matter [96]. The observation of metal-poor stars that preserve the composition of *r*-process events in the early galaxy enables an extraction of the elemental abundance pattern produced by the *r*-process [79].

Nuclear physics plays a crucial role in interpreting the measured abundances and providing a pathway to validate the *r*-process models. The extraction of the isotopic *r*-process abundances to the three peaks as shown in figure I.2 was possible only by high-precision information on *s*-process neutron capture rates [8]. Future, accurate *r*-process nuclear physics experiments would allow to search for additional contributions to the nucleosynthesis beyond the s- and *r*-process.

The double-peak structure in the above figure is direct evidence for the existence of an s- and *r*-process: Isotopes with closed neutron shells have on the one hand a lower neutron capture cross-section than isotopes with 'non-magic' neutron numbers, and on the other hand it is the processes of photodisintegration and neutron capture, which compete. That is, along those shells the (n,γ) $\rightleftharpoons$ (γ, n) rates mostly equilibrate. Therefore, material piles up where the nucleosynthetic paths intersect with the closed neutron shells. As the *r*-process path proceeds far from stability, the β-decay of these overabundant nuclei produces a peak at lower mass number than the *s*-process.

As outlined in [45], nuclear physics quantities needed for *r*-process studies depend on the particular *r*-process model. Usually β-decay properties like decay rates and branching ratios for β-delayed neutron emission, precise information on masses, partition functions describing the spin and parity of low-lying excited states and neutron capture rates are of particular importance. For the very heavy region towards uranium, the knowledge of fission barriers, fission fragment distributions and the properties of neutron induced and β-delayed fission play an essential role for the re-cycling in the *r*-process [5]. While masses and β-decay properties can be obtained with lowest beam intensities and usually sufficient accuracy, reaction studies are

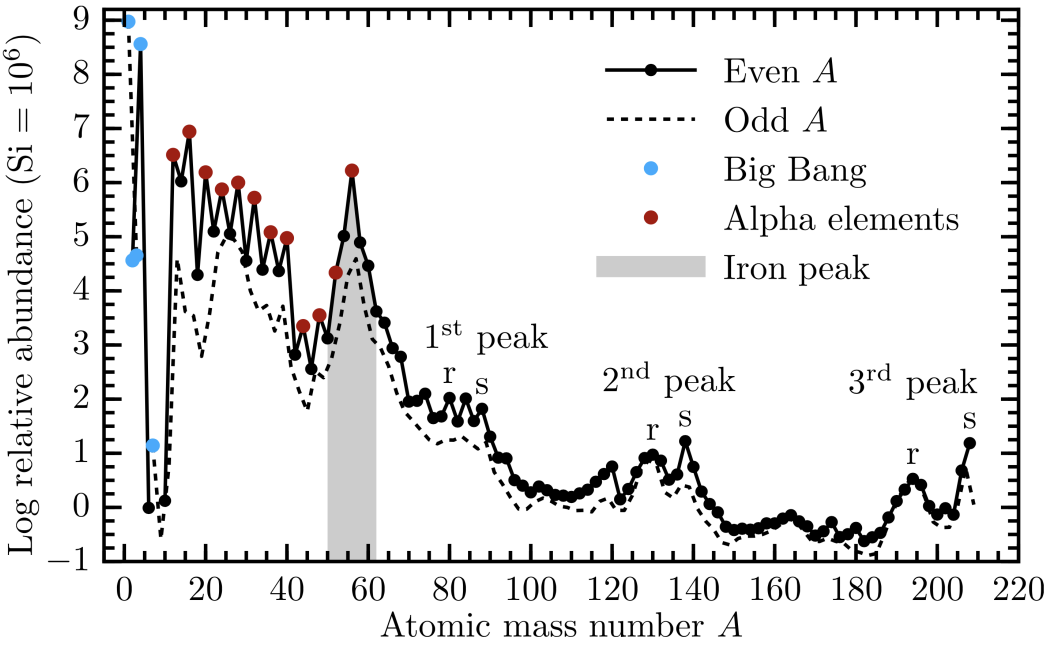

Figure I.2: Solar elemental abundance observed as a function of the mass number A. The main features are the Big Bang abundances of hydrogen and helium that are by far the most abundant elements, the relatively high abundances of the α-elements (elements with integer multiples of an α-particle, formed by α-capture and silicon burning), the iron peak around $A = 56$, and the first, second, and third peaks of the slow and rapid neutron capture processes, respectively. Figure from [45].

much more demanding in terms of radioactive beam intensity and experimental complexity. Direct neutron capture rates on unstable isotopes are due to the lack of a neutron-target, or respectively short-lived radioactive targets not possible. Indirect reaction techniques are required. Surrogate reaction techniques and neutron transfer reactions such as (d,p) have been used in pioneering measurements [46] to probe bound states relevant for the direct capture component of the *r*-process reactions.

The interpretation of the data obtained in transfer reactions is strongly related to theoretical shell models describing the nuclear structure of the produced nucleus. Especially the spectroscopic information on (single-)particle orbits and the extraction of the spectroscopic strength of a transfer reaction allows to draw important conclusions for bound particle levels, which can be used to improve astrophysical reaction rates [11]. Precise nuclear data is essential to predict the specific elements that are created in an observed astrophysical environment, and to connect observed abundances and kilonova features back to astrophysical conditions and constraints on the nucleosynthesis site.

Due to the nature of the *r*-process proceeding far from stability, radioactive beam facilities play an important role to improve the understanding of the processes that shape our universe. While progress has been made at many laboratories, there is still the quest for more intense and varied rare isotope beams reaching for measurements with nuclei directly participating in the *r*-process. With the upcoming next-generation radioactive beam facilities, *r*-process nuclei up to $A \approx 200$ will be within experimental reach. The construction of FRIB at NSCL [67] and FAIR at GSI [33] are two promising fragmentation facilities. Two (future) representatives exploiting the ISOL-technique are HIE-ISOLDE at CERN [26] and ARIEL at TRIUMF [90]. Different approaches like the $N = 126$ factory at ANL [6] try to reach the third *r*-process abundance peak in exploiting multi-nucleon transfer reactions [95]. In any case, new accelerator facilities can only provide a glimpse of new and exciting physics if the instrumentation undergoes the same level of development.

The work done within this thesis, especially the development of HI-TREX can make a small contribution to this demand for new technical developments.

CHAPTER II

Transfer reactions in a theoretical approach

While knockout reactions as (p,2p) or (e,e'p) provide sufficient energy to probe deeply bound nuclear shell structures, in particular the excitation of deep hole single-particle states, a different method is required to test the surface structure of nuclei: "Transfer reactions, the only technique for mapping out the single-particle degree of freedom" [80]. As John Schiffer so aptly put it, transfer reactions provide unique opportunities to populate and probe certain states in nuclei with a structure given by the original nucleus as a core and the transferred nucleon in an orbit around it. One-step transfer reactions, like the one-neutron transfer (d,p) reaction exhibit a strong specificity at moderate projectile energies due to their surface character, which is a consequence of the limited penetration of the e.g. deuteron into the nuclear interior [34]. Direct reactions are characterised by a usually strong overlap of the initial and final wave functions, resulting in a quick ($\lesssim 10^{-22}$s) reaction with a minimum of restructuring processes. Contrarily to compound-nuclear reactions, direct reactions address only little degrees of freedom in nuclear systems and hence provide a very unique tool to investigate single particle nuclear structure [60].

II.1 Transfer reactions in spectroscopic studies

Transfer reactions (single- or multi-nucleon) are direct reactions of the type

$$A + b \rightarrow a + B. \tag{II.1}$$

Generally, this is a very complex many-body reaction. Figure II.1 is visualising this type of reaction by considering that the initial nucleus A can be described as a composed cluster of $a + \nu$. During the reaction, a survives in the final state, whereas

ν gets attached to the nucleus b and forms another composite system B. Such transfer reactions can populate a variety of states in the residual nucleus B, reflected by the kinematics of the outgoing ejectile a. More precisely, it is the Q-values to populate the various excited states in the nucleus B which can be measured directly via the energies of the ejected ion a and, by knowing the ground-state masses of all participating nuclei, the spectrum of the populated excited states can be determined [11].

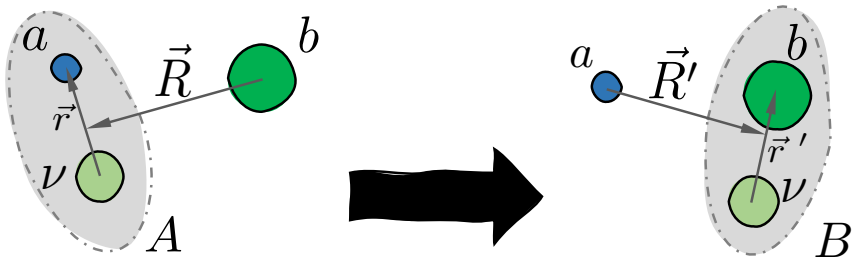

Figure II.1: Schematic representation of a transfer reaction before and after the transfer of mass. For most of the discussion, the transferred particle ν is a single nucleon.

Next to the energy and mass transfer, momentum and angular momentum are exchanged by the projectile and the target nucleus. It is not only the spatial overlap of the wave functions of the projectile and target, which favour a transfer reaction, but also the overlap in momentum space: E.g. in a (d,p) reaction, the neutron will preferably undergo transfer to an unoccupied neutron state only if its momentum (or velocity) in the final state is not too different from its initial one. By examining the angular distribution of the ejectile a (which is a proton in the case of the (d,p) reaction), one can deduce the orbital angular momentum l transferred along with the captured neutron to the largest nucleus. The angular distribution is not sensitive to the value of the total angular momentum $j = l \pm 1/2$. That sensitivity can be obtained in (d,p) reactions using polarised deuteron beams. [34, 78].

The striking correlation of the nuclear structure with the (d,p) angular distribution is the most unique feature of transfer reactions. This correlation is only valid in a limited energy range where the reaction is peripheral. At very high and very low energies, the deuteron penetrates far into the nuclear interior, respectively the Coulomb interaction is dominating the reaction and hence the angular distributions do not provide pronounced nuclear structure information as in the intermediate energy region where the deuteron just reaches the surface of the nucleus but not much beyond [88]. In addition to spectroscopic information on the single-particle orbit for the neutron, the magnitude of the (d,p) cross-section can provide the strength of the single-particle state and thus adds another information to the total

nuclear wave function. In any case the interpretation of transfer data and the linking of angular distributions to nuclear structure needs appropriate theoretical models.

The following theoretical formalism to describe transfer reactions in a quantum mechanical three-body approach is adapted from [39] and [100]. To describe the quantum mechanical state of the nucleus A in the reaction II.1,

$$\Phi_A = C^A_{a\nu}\phi_a\phi_\nu\varphi_{a\nu}(\boldsymbol{r}) + \Phi^C_A \tag{II.2}$$

can be used in general. $C^A_{a\nu}\varphi_{a\nu}(\boldsymbol{r})$ represents the overlap function of the clusters a and ν, each described by their internal wave function ϕ_a and ϕ_ν. $C^A_{a\nu}$ is the spectroscopic amplitude of the normalised relative wave function $\varphi_{a\nu}(\boldsymbol{r})$. In contrast to the other terms of the equation, the part Φ^C_A does not describe the relative motion of the two particles, but represents a more complex configuration.

Accordingly, the following can be written for the state of the nucleus B

$$\Phi_B = C^B_{b\nu}\phi_b\phi_\nu\varphi_{b\nu}(\boldsymbol{r}') + \Phi^C_B. \tag{II.3}$$

The transfer process for the many body problem can thus be described using an appropriate many-body $\mathcal{T}$-matrix operator $\mathscr{T}$, the wave functions of the nuclei A, B, a and b, as well as the relative motion of A and b, χ_{Ab}, and respectively of B and a denoted with χ_{aB} as

$$\mathcal{T}(aB, Ab) = \langle\Phi_B\phi_a\chi_{aB}|\mathscr{T}|\Phi_A\phi_b\chi_{Ab}\rangle. \tag{II.4}$$

Experimentally directly accessible is the magnitude of the (differential) cross section σ which is related to the transition matrix element via

$$\frac{\mathrm{d}\sigma}{\mathrm{d}\Omega} \propto |\mathcal{T}(aB, Ab)|^2. \tag{II.5}$$

In order to reduce the many-body problem to a three-body problem, some approximations can be made: Introducing the eigenstates of two-body Hamiltonians with interactions $V_{b\nu}$ and $V_{a\nu}$ (practically one chooses some real mean-field interactions) approximates the normalised overlap functions $\varphi_{b\nu}(\boldsymbol{r}')$ and $\varphi_{a\nu}(\boldsymbol{r})$. Furthermore, the complicated interactions of all clusters a, b and ν are replaced by two-body effective interactions $V_{a\nu}$, $V_{b\nu}$ and U_{ab}, which do not alter the internal states of the clusters and hence do not take into account any excitation of a nor b. U_{ab} is a complex, optical potential. These approximations lead to the following expression:

$$\mathcal{T}(aB, Ab) = C^{B*}_{b\nu}C^A_{a\nu}\mathcal{T}^{(3)}(aB, Ab). \tag{II.6}$$

The three-body matrix element $\mathcal{T}^{(3)}$ can be expressed either in the post representation

$$\mathcal{T}^{(3)}(aB, Ab) = \langle\chi^{(-)}_{aB}(\boldsymbol{R}')\varphi_{b\nu}(\boldsymbol{r}')|V_{a\nu} + U_{ab} - U_{aB}|\Psi^{(+)}(\boldsymbol{R}, \boldsymbol{r})\rangle \tag{II.7}$$

or the prior representation

$$\mathcal{T}^{(3)}(aB, Ab) = \langle \Psi^{(-)}(\boldsymbol{R}', \boldsymbol{r}') | V_{bv} + U_{ab} - U_{Ab} | \chi^{(+)}_{Ab}(\boldsymbol{R}) \varphi_{av}(\boldsymbol{r}) \rangle. \tag{II.8}$$

$\Psi^{(+)}(\boldsymbol{R}, \boldsymbol{r})$ is the exact solution of the three-body problem of a, b and v with their corresponding interactions, with boundary conditions given by plane waves with the incident momentum in the beam direction, on the $A - b$ coordinate $\boldsymbol{R}$ times the bound wave function $\varphi_{av}(\boldsymbol{R}')$, plus outgoing waves in all open channels. U_{aB} is a suitable potential, arbitrary at this stage, that is used to construct the two-body relative wave function $\chi^{(-)}_{aB}(\boldsymbol{R}')$. This wave function has boundary conditions given by a plane wave, with the final momentum in the direction of the detector, on the $a - B$ coordinate $\boldsymbol{R}'$ plus incoming waves. In the prior form, equivalently, the two- and three-body wave functions have similar meanings; *mutatis mutandis*.

The previous expressions are exact in a three-body model and the post- and prior-form do give identical results as long as the exact solutions of the three-body wave functions are used to evaluate the transfer transition amplitude. In II.6, the structure information contained in the spectroscopic amplitudes C_{av} and C_{bv} is well separated from the reaction mechanism. Using II.5 the cross-section hence factorises into two parts: the single-particle cross-section and the so-called spectroscopic factor S, which is the square of the spectroscopic amplitudes. The spectroscopic factor for the probe in a (d,p) reaction is known and the one for the nucleus of interest is determined by comparing the measured cross-section to the calculation for $S = 1$. The spectroscopic factor can thus be understood as a quantity that links measurements to microscopic theories of nuclear structure.

As no exact solutions to the three-body wave functions are available, approximations have to be made. Each approximation - illustrated in figure II.2- takes into account different complexities of transfer reactions and thus has different scopes.

Distorted Wave Born Approximation (DWBA): The DWBA is approximating the three-body wave function as

$$\Psi^{(+)}(\boldsymbol{R}, \boldsymbol{r}) \simeq \Psi^{(+)}_{DWBA}(\boldsymbol{R}, \boldsymbol{r}) = \chi^{(+)}_{Ab}(\boldsymbol{R}) \varphi_{av}(\boldsymbol{r}). \tag{II.9}$$

This approach treats transfer as a small perturbation of the elastic scattering. Hence, the accuracy of the DWBA depends strongly on the choice of the auxiliary optical potential U_{aB}. Two approaches are usually taken to describe U_{aB}: In the microscopic approach U_{aB} is taken as the expectation value, in the final bound state $\varphi_{bv}(\boldsymbol{r}')$, of the sum of the interactions $U_{ab} + V_{av}$ with the advantage of being completely determined by the two-body interactions of the fragments. However, elastic scattering is hard to reproduce accurately and any effect of break-up channels on the three-body wave function is excluded. In the phenomenological approach, U_{aB} is obtained by fitting the elastic scattering data on the aB channel. It takes into

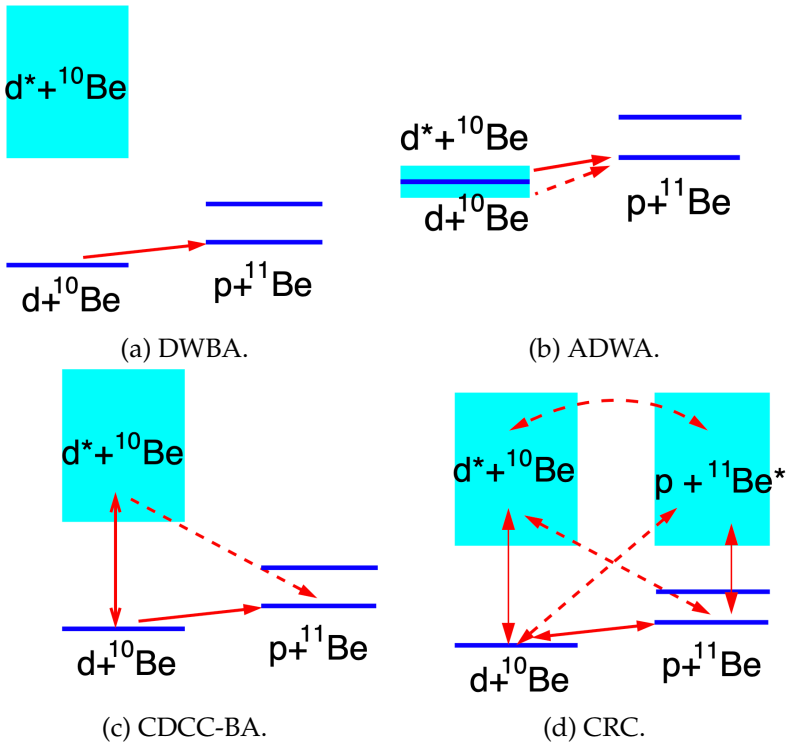

(a) DWBA. (b) ADWA.

(c) CDCC-BA. (d) CRC.

Figure II.2: Comparison of different coupling schemes for the reaction ^{10}B(d,p)^{11}B. The shaded areas represent excited states. The solid arrows indicate single-step reactions in contrast to the dashed arrows, illustrating multi-step transfer reactions. Note, nor any absolute nor relative energy scale may be assumed. Figure adapted from [39].

account the remove of flux by complex reactions such as fusion, but sometimes the experiment lacks of elastic scattering data and hence no fit can be done. In any case, by the use of arbitrary optical potentials, the elastic wave functions are only reproduced asymptotically at large values of $\boldsymbol{R}$ and not necessarily in the radial range relevant for the transfer $\mathcal{T}$-matrix elements.

Adiabatic Distorted Wave Approximation (ADWA): Contrarily to the DWBA, the ADWA's ingredients can be entirely determined from experiment. Only the proton-nucleus and neutron-nucleus potentials are required to calculate the cross-section for a (d,p) reaction. ADWA is valid for weakly bound system such as

the deuteron (binding energy of only $-2.225\,\mathrm{MeV}$) and assumes that the relative coordinate $\boldsymbol{r}$ is 'frozen' at sufficiently high collision energies:

$$\Psi^{(+)}(\boldsymbol{R},\boldsymbol{r}) \simeq \Psi^{(+)}_{ADWA}(\boldsymbol{R},\boldsymbol{r}) = \chi^{(+)}_{Ab}(\boldsymbol{R},\boldsymbol{r})\varphi_{av}(\boldsymbol{r}). \tag{II.10}$$

The ADWA is only valid for small values of $\boldsymbol{r}$ and hence has difficulties in describing both transfer and elastic scattering processes consistently. However, break-up of the deuteron is taken into account as degenerated energy levels.

Continuum Discretized Coupled Channels Born Approximation (CDCC-BA):

$$\Psi^{(+)}(\boldsymbol{R},\boldsymbol{r}) \simeq \Psi^{(+)}_{CDCC}(\boldsymbol{R},\boldsymbol{r}) = \sum_{i=0}^{N} \chi^{(+)}_{Ab,i}(\boldsymbol{R})\varphi_{av,i}(\boldsymbol{r}) \tag{II.11}$$

This *ansatz* approximates the three-body wave function in terms of a basis of states of the relative motion of the $a+\nu$ subsystem. The explicitly included states i correspond in general to a given spin and spin projection. Thus, all relevant bound and discretised continuum states are included in the calculation enabling multi-step transfer reactions via the excited states of the projectile. In order to accurately describe realistic experiments, a very large basis of internal states has to be included, making this approach numerically demanding.

Coupled Reaction Channels (CRC): The CRC method can be understood as a generalisation of the CDCC-BA *ansatz*:

$$\Psi^{(+)}(\boldsymbol{R},\boldsymbol{r}) \simeq \Psi^{(+)}_{CRC}(\boldsymbol{R},\boldsymbol{r}) = \sum_{i} \chi^{(+)}_{Ab,i}(\boldsymbol{R})\varphi_{av,i}(\boldsymbol{r}) + \sum_{j} \chi^{(+)}_{aB,j}(\boldsymbol{R}')\varphi_{bv,j}(\boldsymbol{r}'). \tag{II.12}$$

By incorporating contributions from several mass partitions (ground state and excited states) of both the incoming partition Ab as well as the outgoing partion aB, rearrangement channels are described far better than in the CDCC-BA method. Substituting $\Psi^{(+)}_{CRC}(\boldsymbol{R},\boldsymbol{r})$ into the Schrödinger equation

$$[H-E]\Psi^{(+)}_{CRC} = 0 \tag{II.13}$$

allows to obtain the radial functions $\chi^{(+)}_{Ab,i}(\boldsymbol{R})$ and $\chi^{(+)}_{aB,j}(\boldsymbol{R}')$, which are constituted by a term describing the relative motion between the projectile and the target for each state of the projectile and a second term representing the couplings between the states of the initial and the final partition.

To be complete, the *Fadeev formalism* [32] is treating the three-body scattering problem rather in a rigorous than a heuristic way like does the CRC. Furthermore, *ab initio* approaches have been developed and can be performed for medium heavy nuclei already [40].

Various computer codes exist incorporating the above-mentioned approximations for calculating theoretical solutions to transfer reactions. For better comparison to experimentally measured quantities, differential cross-sections are mostly the output of these codes. The Fresco code [86] is widely used for DWBA and coupled reaction channels calculations. [87] describes the FaCE tool for three body Faddeev calculations with core excitation. An extensive comparison and review on different theoretical implementations to approximate the transfer wave functions can be found in [10].

II.2 Transfer experiments with radioactive beams for nuclear astrophysics

Novae, X-ray bursts and the r-process are strongly influenced by the properties of exotic, radioactive nuclei. Current and future exotic beam facilities are promising opportunities to investigate some of the astrophysical relevant reactions. Transfer reactions help in the understanding of the r-process, whose path is determined by the nuclear structure, the decay and the reaction properties of neutron-rich nuclei [79]. Knowledge of masses, neutron-capture rates, half-lives and β-decay rates are important ingredients in r-process models [69]. The use of (d,p) reactions can lead to improved astrophysical rates in several ways: Spectroscopic strengths of bound levels can be used to calculate the direct neutron capture rate and the extracted Q-values can lead to a determination of the mass of the produced nucleus, which directly affects the r-process path at a given temperature [11].

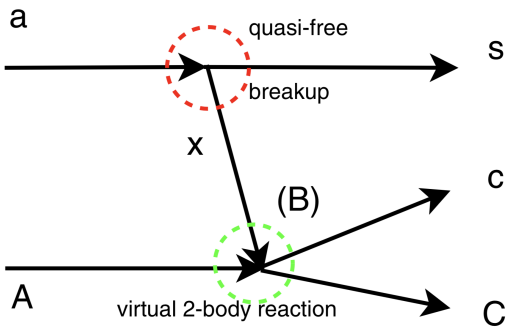

Figure II.3: *Trojan Horse Method*. Figure adapted from [53]

Especially the surrogate reaction (d,pγ) for the neutron-capture reactions to (un)bound states and the *Trojan Horse Method* (THM) are applications of transfer reactions with direct astrophysical importance. The THM involves obtaining

the cross-section at astrophysical energies for the (experimentally not accessible) reaction

$$A + x \rightarrow c + C \tag{II.14}$$

by measuring the reaction

$$A + a \rightarrow c + C + s. \tag{II.15}$$

a contains a significant $s + x$ cluster component in its wave function and x is transferred. One can deduce the energy dependence of the astrophysical process from the THM cross-section as long as the reaction proceeds through the kinematical condition of a quasi-free process, meaning that the cluster s remains spectator to the process and thus the reaction can be regarded as a virtual two-body reaction. Since the three-body reaction occurs at an energy above the Coulomb-barrier, a beneficial feature is the suppression of the Coulomb barrier and (electron) screening effects in the virtual two-body reaction can be omitted. With this method a measurement of the astrophysical $S(E)$-factor at very low energies ($E < 10\,\mathrm{keV}$) was possible [54]. The THM has its greatest success in application to (p,α) reactions but astrophysical relevant (d,p) reactions have been studied as well ([91] and references therein).

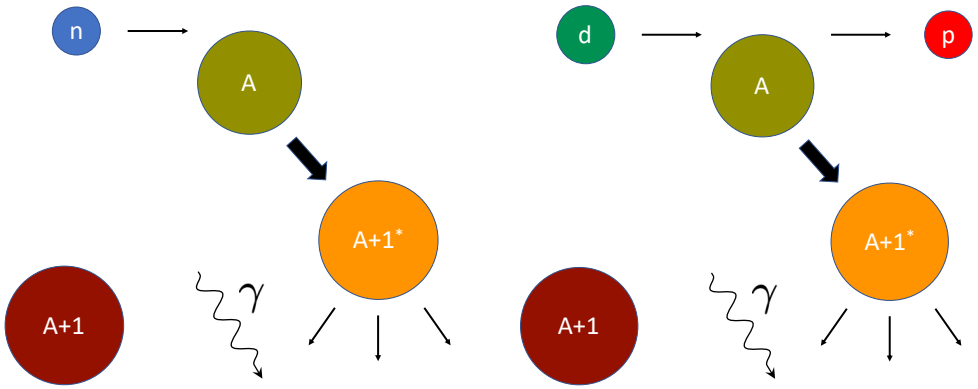

(a) Astrophysical relevant (resonant) neutron-capture reaction.

(b) Direct surrogate (d,pγ) reaction.

Figure II.4: Surrogate reaction method.

The surrogate reaction method is applicable when a resonant neutron capture is more important than a direct capture. This is the case for many exotic nuclei in the r-process with a level density high enough to favour resonant reactions. The resonant (d,pγ) reaction is used to populate the same compound levels as in the (n,γ) reaction and the measurement of the subsequent γ-decay branching ratios

allows to estimate the neutron-capture cross-section. The underlying assumption is that the compound nucleus is sufficiently long-lived and that hence its decay is independent of the entrance channels.

The Hauser-Feshbach formalism is used to express the neutron-capture reaction as

$$\sigma_{\alpha\chi}(E_n) = \sum_{J,\pi} \sigma_\alpha^{CN}(E_{ex}, J, \pi) G_\chi^{CN}(E_{ex}, J, \pi) \tag{II.16}$$

with $\sigma_\alpha^{CN}(E_{ex}, J, \pi)$ being the cross-section for forming a compound nucleus (CN) in the entrance channel $\alpha = n + A$ [31] with an excitation energy E_{ex}, the spin J and the parity π. The exit channel as depicted in II.4a is $\chi = (A+1) + \gamma$ and the $G_\chi^{CN}(E_{ex}, J, \pi)$ describe the branching ratios for the decay of the CN and need to be determined and constrained by experiment.

The probability to form a specific state of the CN in the surrogate reaction shown in II.4b is $F_\delta^{CN}(E_{ex}, J, \pi)$ with $\delta = d + A$. Hence,

$$P_{\delta\chi}(E_{ex}) = \sum_{J,\pi} F_\delta^{CN}(E_{ex}, J, \pi) G_\chi^{CN}(E_{ex}, J, \pi) \tag{II.17}$$

displays the probability that the CN was formed with E_{ex} and decayed into the channel χ. For a (d,pγ) reaction, this quantity can be measured experimentally by relating the total number of surrogate events detected by the outgoing protons N_p to the number of coincidences between the protons and γ-rays $N_{p\gamma}$ as

$$P_{p\gamma}^{exp}(E_{ex}) = \frac{N_{p\gamma}}{N_p}. \tag{II.18}$$

To calculate the cross-section from a surrogate measurement, the spin-parity distribution $F_\delta^{CN}(E_{ex}, J, \pi)$ can be calculated from a suitable theory, or can be modeled to existing nuclear structure information, provided sufficient data exist. A successful application of the reaction (d,pγ) as a surrogate for (n,γ) was demonstrated in [74].

II.3 Experimental approach for investigating transfer reactions

Experimental progress is intimately linked with theoretical interpretation of the data, and *vice versa*, the accuracy of theory's models strongly depends on experimental input. Properly designed experimental setups are crucial to the success of any investigation of transfer reactions and thus in the manifestation of theoretical descriptions and models. The following section is intended to present some experimental approaches to study single nucleon transfer reactions. Exemplarily,

the reaction d(^{132}Sn, p)^{133}Sn, which has been successfully measured by [46] is detailed, as this reaction is later-on used as a 'show-case' reaction for the simulations presented in chapter III.

The choice of the reaction type is strongly influencing the requirements for a setup of detectors, as the 'footprint' of normal and inverse kinematics differs heavily. In figure II.5 an exemplary reaction kinematics can be seen.

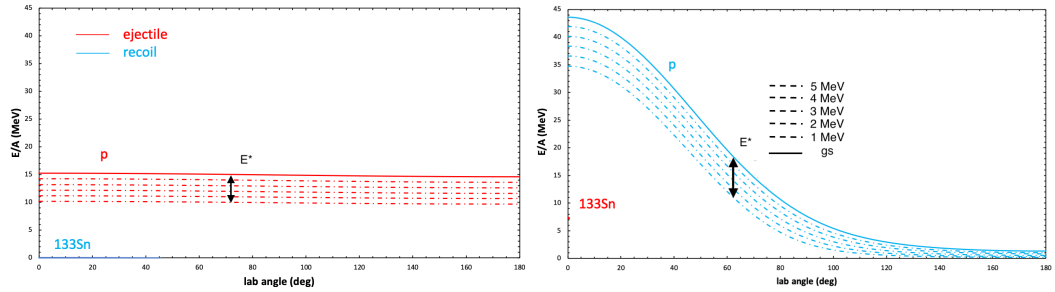

(a) Normal kinematics. (b) Inverse kinematics.

Figure II.5: Kinematics of the d(^{132}Sn, p)^{133}Sn at 7.5 MeV/u. Blue (red) lines correspond to the recoil (ejectile). Dashed lines represend excited states from 1 to 5 MeV being populated in the outgoing nucleus ^{133}Sn.

The kinematic course of the proton distribution is much more pronounced in inverse kinematics and the so-called kinematic compression influences strongly the separation of different excited states in the backward direction ($\theta_{lab} > 90°$) and competes with any trigger and detection threshold required by a detector. Furthermore, a high angular, as well as energy resolution is required over the full angular range as the excitation energy needs to be reconstructed from the measured angles and energies in case the (light) recoil is used to reconstruct the reaction and excitation energies. The measurement of only one of the reaction partners is sufficient, as transfer reactions are missing mass experiments in a well defined twobody kinematics [100]. In principle, it would also be possible to detect the (heavy) ejectile in a transfer experiment in inverse kinematics using e.g a magnetic spectrometer, which would only require a small angular range around the beam-axis in order to guarantee a 4π coverage of the reaction. However, extremely high resolution for angle and momentum are required to distinguish excited states and thus extremely thin targets must be used. The reason for using the inverse kinematics approach for (d,p) reactions is mainly due to the production of radioactive beams, as detailed in section III.1.

With the choice of the bombarding energy, the overall transfer cross-section is influenced, as well as the shape of the differential cross section and thus the

assignment of the orbital angular momentum transfer with some detector array placed in the laboratory system.

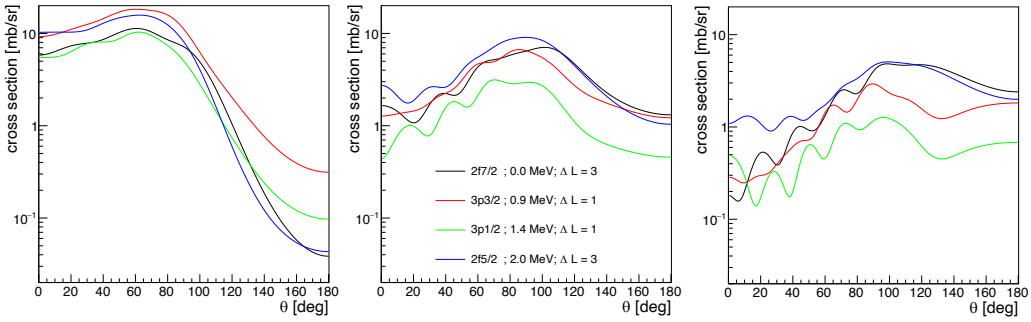

(a) 5.0 MeV/u. (b) 7.5 MeV/u. (c) 10 MeV/u.

Figure II.6: Differential cross-sections for d(^{132}Sn, p)^{133}Sn at various beam energies. Each panel shows calculations for several different l-transfers. The plots are in terms of the laboratory angle θ and have been performed using the DWBA due to its simplicity.

The differential cross-sections in the laboratory frame at various beam energies can be seen in the calculations in II.6. At 5.0 MeV/u the distributions are less distinctive due to the suppressed nuclear component at forward angle parts (small $\theta_{c.m.}$) owing to the Coulomb repulsion between the projectile and the target [24]. Additionally, the general trend of decreasing cross-sections with increasing beam-energy can be nicely seen.

In general, limiting factors in radioactive beam experiments are the intensities (respectively the low cross-sections) and the energy scattering of the beam in the target. Typical targets are deuterated polyethylene foils with a thickness of $\gtrsim$ 0.1 mg/cm^2 (but the thickness is limited to around 1 mg/cm^2 due to energy straggling) and beam intensities of 10^4 particles per second.

To summarise, for transfer reactions in inverse kinematics and especially (d,p) reactions, the measurement of one of the reaction products' energy and angular distribution with high precision is required. Several approaches exist for a detector system to extract meaningful excitation energy values and differential cross-sections:

First, beam-like particles can be detected with a magnetic spectrometer like SPEG at GANIL [13]. The drawback of this method was already discussed. It is the detector resolution, which is needed for heavy ions and which gets at some point impractical for existing detectors.

Second, the detection of target-like recoils can be employed. Solid-state detectors, especially silicon detectors are the means of choice to cover a large angular range with acceptable energy resolution. High segmentation is required to guarantee the

proper reconstruction of excited states. In practice, the target thickness is limiting the resolution for the excitation energy. Furthermore, in forward direction, the kinematic curves from different transfer reaction channels as well as elastic scattering partially overlap, requiring particle identification, usually achieved by measuring the specific energy loss in two or more layers of silicon.

Another approach to detect the light recoils was pioneered with the HELIOS setup at ANL [104]. By use of a magnetic solenoid, no kinematic compression is limiting the measurement, nor an extensively segmented silicon array is required as the protons are focussed onto a detector located around the beam axis and their dispersion is linearly dependent on their energy. However, the acceptance of the spectrometer is limited by its radius and field strength. Furthermore, the placement of auxiliary detector inside the magnetic field is challenging.

The most promising experimental approach to measure transfer still is the coupling of a highly-segmented silicon detector array to a high purity germanium array of γ-detectors. This drastically improves the energy resolution of excited states by exploiting a particle-γ coincidence and helps to assign spins an parities in addition to the information obtained from the measurement of the differential cross section. Measuring γ-rays is always challenging in terms of efficiency and appropriate Doppler-corrections need to be applied.

Transfer experiments with radioactive beams in inverse kinematics are a unique tool to investigate physical properties of various nuclei and processes. The well-established particle-γ-technique has been successfully used to perform one- and two-neutron transfer reactions with the TREX silicon array in conjunction with the γ-array MINIBALL. To cope with the facility developments as indicated in I, the focus of this work was the development of a silicon sensor array, based on the experience with TREX, which can be coupled to MINIBALL at HIE-ISOLDE energies and provides extended resolution and identification capabilities.

CHAPTER III

From conceptual design to detailed setup: Challenges in transfer experiments with radioactive beams

TREX (Transfer at REX) is a versatile silicon detector unit for measuring transfer reactions with heavy, neutron-rich beams at CERN/ISOLDE. Position sensitive ΔE-detectors and unsegmented E-detectors in a compact setup allow for a unique particle identification in 66% of the full solid angle for light reaction products. TREX [14] is optimised for transfer reactions in inverse kinematics and is designed to be used in combination with the MINIBALL [94] detector array.

Whole series of successful experiments have been performed at MINIBALL, using Coulomb-excitation, one- and two-neutron transfer reactions and radioactive ion beams (RIBs) from REX-ISOLDE ranging from ^{6}He to ^{226}Ra. The higher beam intensities of neutron-rich beams like ^{132}Sn and ^{142}Xe enable different physics aspects to be covered together with having higher beam-energies available with the HIE-ISOLDE upgrade which favour larger cross-sections for Coulomb-excitation experiments, a more pronounced differential cross-section pattern in transfer experiments, but also the improved production of highly charged ions will be beneficial for mass measurements, which are of utmost importance for validating nuclear astrophysics scenarios. In the case of reaction studies there is the clear need for an adapted silicon setup being able to cope with heavy, neutron-rich beams with energies as high as 10 MeV/u for ions with $A/q = 4$.

III.1 Beam production: Basic restrictions

Radioactive isotopes for in-beam experiments are typically produced in two different ways: The isotope seperation online (ISOL) technique, or the in-flight method at

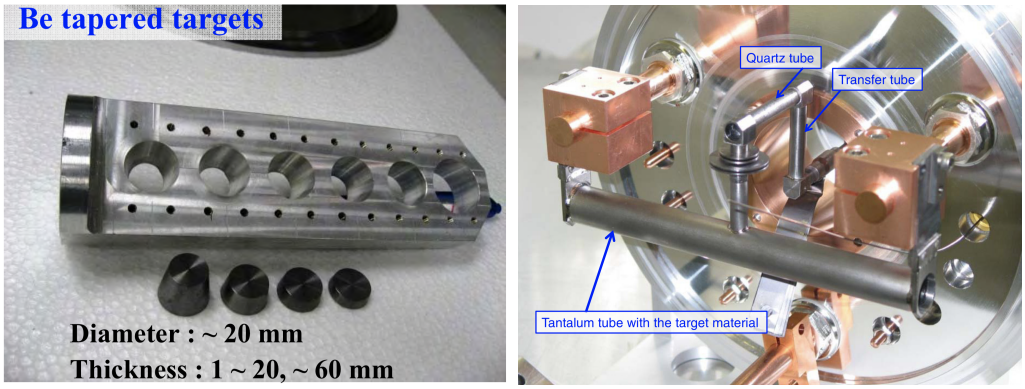

(a) Fragmentation target at BigRIPS facility, RIKEN.

(b) Production target at HIE-ISOLDE facility, CERN.

Figure III.1: Production targets for in-flight production (III.1a) of radioactive isotopes, and ISOL production (III.1b). Pictures adapted from [105, 15].

fragmentation facilities. At those latter facilities a high intensity, stable beam is accelerated to typically several ~ 10 MeV and impinges on a usually thin and low-Z production target, such as beryllium, as the production yield is larger for light materials due to a better ratio of nuclei being present (see fig. III.1a, [66]). The processes which mainly lead to the production of radioactive isotopes are spallation, fragmentation, fission and in some cases fusion as well ([66] and references therein). For in-flight facilities the reaction products have a similar velocity as the beam and are strongly forward focused. Usually a separation device and optional further beam manipulation devices like range bunchers, stopping cells or storage rings, purify the beams being produced. Beneficial over the ISOL-production technique is the 'chemical blindness' [15], i.e. the possibility of producing radioactive ions regardless of their atomic properties. However, the emittance of the beam is poor as the kinematical conditions of the production reactions are dominant. The use of thick production targets together with degraders, enables transfer reactions in a suitable energy range of tens of MeV. Another constraint, which is valid for both the in-flight method and the ISOL-technique, is the limit of half-live of ions accessible (typically $T_{1/2} > 1\,\mu$s), as in both cases the ions need to be transported from the production site to the experiment.

Contrarily to the in-flight technique, the ISOL-technique usually produces beams of good quality in terms of emittance and energy spread, as the radioactive isotopes are produced (nearly) at rest: A light, high-energetic beam (presently 1.4 GeV protons at HIE-ISOLDE) induces various fragmentation, spallation and fission reactions in a very thick (up to 20 cm length) target (see fig. III.1b). The produced isotopes then need to diffuse out of the heated target container and need to be ionised (there

are currently three different ionisation methods exploited at ISOLDE: surface ion sources, plasma ion sources and laser ion sources; for a nice and compact overview please refer to [44]) and accelerated by an applied electrical field of typically 10 kV . . . 60 kV before some mass separation stage with high resolution power is able to select the isotopes of interest. The process of extraction from ISOL targets is delayed by diffusion in the target material and affected by chemical losses. Therefore short-lived isotopes with a reactive nature are typically difficult to extract and thus often only available in reduced quantities/intensities [81].

Recent developments within the *ENSAR2*-project [1] have succeeded in establishing a new type of radioactive plasma ion sources by employing so-called molecular beams. Here, the production of beams of refractory elements can be improved using chemical methods, such as volatile molecular formation with injection of reactive gas in the target and ion source production unit. A new delivery method for ^{34}S chemical was developed at ISOLDE, and the successful production of ^{132}Sn^{34}S^{+} ions is an important step towards the production of ever more exotic nuclei at ISOL-facilities [62].

For an efficient post-acceleration the singly charged ions have to be ionised into a higher charge state. This charge-state breeding is done in two steps: First, the continuous beam from the ISOL-target is decelerated and captured in an RF-cooler-buncher or Penning trap. The cooling is achieved through collisions of the beam with some buffer gas. Continuous accumulation of the ion beam and buffer-gas cooling forms cooled bunches of ions that are prepared for injection into a charge breeder or used to increase the peak-to-background ratio in collinear laser spectroscopy experiments [15]. Second, the charge-breeder ionises the singly charged ions by a highly intense electron beam until the optimum charge state for subsequent post-acceleration is reached. In the case of HIE-ISOLDE the charge state q must fulfil the condition $A/q \leq 4.5$ which is a prerequisite of the REX linac [44]. Typical breeding times reach from a few 10 ms up to 350 ms for the heaviest beams. A schematic of all the different stages during beam-production is depicted in figure III.2.

The basic restrictions for RIB production are the extremely low production cross section of the isotopes of interest, their (in some cases) very short half lives and the overwhelming production of unwanted species in the same nuclear reaction. Hence, the whole beam production process must have a high production rate (mostly accomplished by highest primary beam intensities and target systems capable of depositing multi kW of power), excellent efficiency (throughout the whole production, extraction, acceleration and detection process), high selectivity and short delay times.

[1] European Nuclear Science and Application Research 2 has received funding from the European Union's Horizon 2020 research and innovation programme under grant agreement No 654002

III.2 HIE-ISOLDE: Improvements and constraints

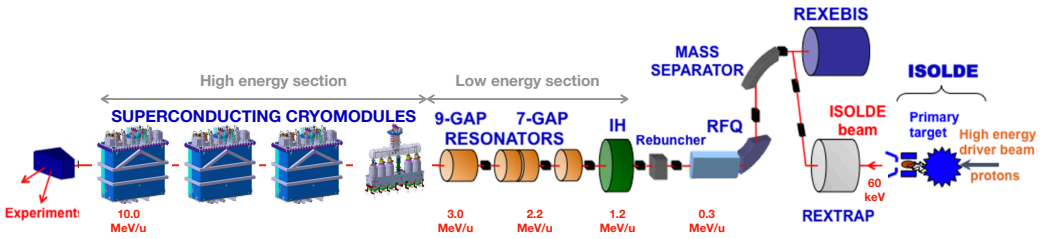

Figure III.2: HIE-linac layout: Singly charged ions are extracted from the primary target, captured in the large-acceptance Penning trap REXTRAP and charge bred in the REXEBIS ion source to A/q ratios between 2 and 4.5. The ions are released via a mass separator (for removal of buffer-gas residuals) into a compact linear accelerator. The 'old' room-temperature linac consists of a Radio-Frequency Quadrupole (RFQ), a rebuncher section, an Interdigital H-type (IH) structure, three seven-gap spiral resonators and a 9-gap IH resonator. This low-energy section provides energies up to 3.0 MeV/u. The high-energy section is part of the HIE-ISOLDE phase II upgrade utilising superconducting cavities for further beam acceleration together with superconducting solenoids for beam manipulation. Figure adapted from [18, 47]

The High Intensity and Energy ISOLDE (HIE-ISOLDE) project is an upgrade of the existing ISOLDE-facility and a pathway towards the future, ambitious EURISOL facility [55] not only in terms of increased energy and intensity, but also in terms of beam purity, the beam's time and optical structure, as well as its energy definition. Developments accompanying the two main upgrades HIE-linac (energy) and change of the primary beam properties (intensity), but which are not of any less importance for this next-generation facility HIE-ISOLDE include developments on the Resonance Ionisation Laser Ion source (RILIS) to selectively ionise the (primary) reaction products of interest, a redesigned RFQ cooler and buncher to increase the limit of ions in the present device, an improved mass separator with higher resolution power (maybe together with a general multi-reflection time-of-flight mass spectrometer), a new EBIS design with higher electron beam energy and density that will give faster breeding times, as well as beam-dump revisions withstanding higher deposited proton power.

The HIE-ISOLDE energy upgrade is divided into three main phases. In the first phase, two cryomodules were added to the existing REX machine increasing the available energies up to 5.5 MeV/u. The second phase added another two high-β cryomodules, increasing the energy up to at least 10 MeV/u (depending on the

A/q-ratio of the ionised radioactive beam). This phase was completed in 2018 and first experiments exploiting the full energy-capability of the HIE-linac have been carried out. In the final phase III, all existing REX accelerating structures after the IH-structure will be replaced with two low-β cryomodules to improve beam quality and ensure that the beam can even be decelerated and its energy is continuously variable between 0.45 and 10 MeV/u [47]. Even cw-beams are under discussion, but probably not advantageous for transfer experiments due to background considerations [76]. In order to save space for the experiments, the roadmap of the LINAC design was to make the machine as compact as possible. Generally, a compromise between the complexity of building a long cryostat and economical aspects of having as much superconducting cavities as possible per cryostat has been made, which resulted in five cavities per cryostat [55]. One additional superconducting solenoid for beam focussing is introduced between each cryostat's cavity 2 and 3, which reduces the overall space of one cryostat and increases the longitudinal acceptance of the machine. Further beam-quality improvements like increased bunch spacing to 100 ns have been validated as feasible. Multi-harmonic bunching together with a chopper structure (to remove satellite bunches) could permit time-of-flight particle identification, extend background-suppression techniques and increase the A/q-resolution of the facility. A comprehensive overview on further developments within the energy upgrade of HIE-ISOLDE can be found in [47].

The intensity upgrade is driven by two main developments: New target material research and efficiency improvement of the ion source and targets has succeeded in many developments by the ISOLDE technical team, which have been adapted by other ISOL-facilities as well. Another way of increasing the beam intensity is now pursued: Increasing the intensity of the primary proton beam by a factor of $\sim$ 3 to 6.7 µA and increasing the beam-energy of the Proton Synchrotron Booster (the injector machine at CERN for HIE-ISOLDE) from 1.4 GeV to 2.0 GeV [25]. In simulations it is found that an increase of a factor of two to five is expected for the fragmentation process, up to a factor of ten for the spallation process and similar production for fission products. Hence, a factor of 30 higher intensity for some of the delivered RIBs is expected [18, 17].

The main improvements of the HIE-ISOLDE upgrade are justified by the physics programme: The increase of beam energy enables new nuclear physics domains to be studied. As the reaction mechanisms evolve significantly from 3 MeV/u to 10 MeV/u, inelastic reaction mechanisms will be favoured with respect to Rutherford scattering, since its cross-section is proportional to $1/(E_{c.m.})^2$ and allows for larger beam current, when the count rate is an issue [76]. With the increase of intensity, a more flexible bunch structure would be very valuable. The rather high instantaneous rates puts severe constraints on the DAQ-system (see sec. III.3 for more details). Basic beam parameters envisaged for the full HIE-ISOLDE upgrade are summarised in table III.1.

Table III.1: Envisaged beam characteristics at HIE-ISOLDE. Values adapted from [47, 18].

Beam parameter	Value or comment
Energy	continuous from 0.45 to at least 10 MeV/u
Beam spot diameter	$< 1 \ldots 3$mm FWHM
Beam divergence	$< 1 \ldots 3$mrad FWHM
Micro-bunch structure	~ 1 ns FWHM with ~ 100 ns bunch spacing
Macro-bunch structure	longer pulse lengths or cw operation
Energy spread	$< 0.1\%$

III.3 TREX with MINIBALL: Experiences and limitations

In this section, the basic limitations of the present TREX setup in combination with MINIBALL for transfer reactions with heavy, neutron-rich beams will be described. General informations about TREX and MINIBALL can be found in section V.1.2.

TREX has been successfully used in light-ion transfer experiments, especially for the discovery of the shape-coexistence in the 'island of inversion' magnesium isotope ^{32}Mg [101] and in the study of quadrupole collectivity around the $N = 40$ shell gap in ^{67}Ni [27].

The first time, that the separation of excited states in a transfer experiment with TREX was not possible simply by the whole silicon-array itself was the two-neutron transfer experiment t(^{72}Zn, p)^{74}Zn at a beam-energy of $E_{beam} = 2.7$ MeV/u (see figure III.3 for more details). The only possiblity to discriminate between states was to gate on the γ-rays detected in MINIBALL with the drawback of reduced statistics. Contrarily to previous one- and two-neutron transfer experiments like with ^{32}Mg or ^{46}Ar, the level spacing is quite close, which is not a surprising feature, as level densities generally[2] tend to increase with $\rho \propto A^{11/6}$ and the level spacing in terms of energy behaves like $\Delta E \propto A^{-5/3}$ for low-lying states in the rotational model.

A technological aspect limiting the performance of the silicon array can be clearly seen in figure III.3b. The price that is paid for using resistive strips in the barrel region is quite high in terms of performance (although under economical aspects, the reduced number of electronics channels using resistive strips was pivotal): First of all, the position resolution that is achieved is dependent on the energy deposited,

[2] For protons and neutrons one finds for the density of states at excitation energy E in the Fermi gas model [103]: $\rho_A(E) = \frac{1}{12a^{1/4}E^{5/4}} e^{2\sqrt{aE}}$. Assuming only rotational excitations ($E = E_{rot} \propto \frac{\hbar^2}{2I}$ with the moment of intertia $I = \frac{2}{5} A R_0^2 (1 + 0.31\beta) \propto A^{5/3}$) and using the direct proportionality of the level density parameter $a \propto A$, the level density evolves for large A (Puiseux series) in the leading member of the series to $\rho \propto A^{11/6}$.

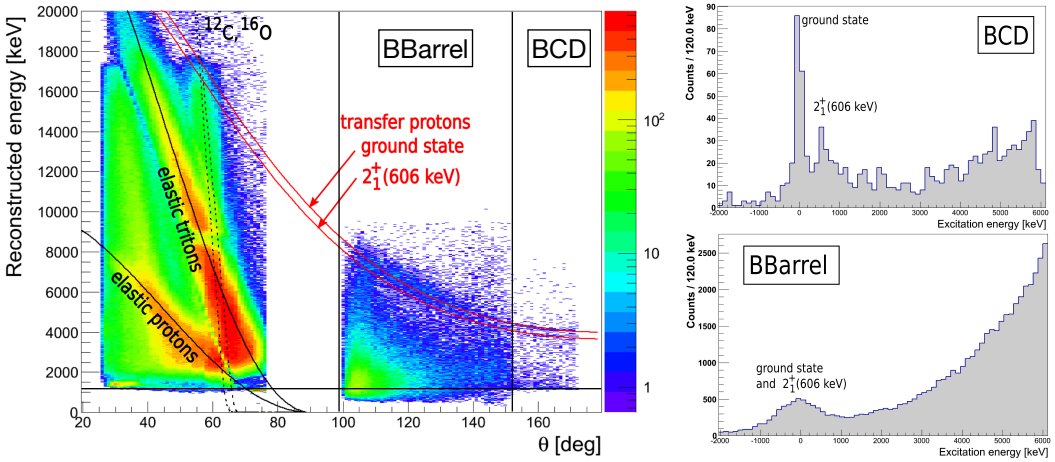

(a) The reconstructed particle energy in the TREX ΔE-E telescopes as a function of the scattering angle θ_{lab} in the laboratory frame.

(b) Detector technology's influence on energy resolution of the excited ^{74}Zn states.

Figure III.3: Two-neutron transfer experiment t(^{72}Zn, p)^{74}Zn at a beam-energy of $E_{beam} = 2.7\,\mathrm{MeV/u}$.
Figure III.3a: In forward direction ($\theta_{lab} < 90°$) the data of the ForwardBarrel is shown. In backward direction between $\theta_{lab} = 98°$ and $\theta_{lab} = 152°$ the BackwardBarrel (BBarrel) data is presented, while the data points beyond $\theta_{lab} = 152°$ belong to the BackwardCD (BCD). Additionally, in forward direction, the identification cuts for the elastics protons and tritons which are obtained from the reaction kinematics are visualised. In backward direction all particles are assigned to transfer protons. The reaction kinematics of the transfer protons to the ground state and first excited 2_1^+ state are superposed. The black, horizontal line indicates the threshold set for the electronics. Picture adapted from [44].
Figure III.3b: Reconstructed excitation energy spectrum of ^{74}Zn from the different detector parts in the backward hemisphere. On top, the double-sided silicon strip detector BCD clearly separates two peaks for the ground state and for the 2_1^+ state. Contrary, in the excitation energy spectra of the BBarrel detector (bottom spectrum), it is not possible to distinguish those two states. The BBarrel detector is a position-sensitive detector made of resistive strips. Picture from [43].

being proportional to $1/E$ [71]. Additionally, the energy threshold of resistive strip detectors is higher than of DSSSDs, as the noise contribution related to the resistance of the strip is in addition [23]. This and the high electron-background as discussed in the next paragraph results in typical thresholds of $> 1.3\,\mathrm{MeV}$, as indicated by the black horizontal line in fig. III.3a. Furthermore, due to the high capacity of

the unsegmented rear side, the TREX resistive strip detectors are very sensitive to electromagnetic pickup and additionally need very long shaping times ($> 1\,\mu s$) and thus impose constraints on the rate-capability of the setup.

Another experience with RIBs, especially heavy and high-energetic ones is the presence of a non-negligible electron background from rather thick targets. As discussed in [44] this is the reason for the high-energetic distribution of the excitation energies in figure III.3b. Additionally, one can nicely see the influence of the different detector technologies: In the barrel detectors, the energy is determined from the large, unsegmented rear side of the detectors. Having such a large solid angle coverage of the rear electrodes together with typical decay times of the preamplifier of $\sim 25\,\mu s$ accumulates many δ-electron signals to a real macroscopic current and induces a huge base-line shift even of the shaped signals. These δ-electrons are produced by the interaction of the RIB with the target. Their intensity scales with the beam intensity and even overproportional with the atomic number Z of the beam. Their energy scales with the beam energy. The pulsed beam-structure at ISOLDE even amplifies this problem disproportionally. Additionally to these δ-electrons, β-electrons from implanted radioactive beam produce some additional background. Contrarily to the resistive-strip detector response to those electrons, the CD-type detectors do not exhibit such a distortion as they are segmented in rings and strips with much smaller solid angle coverage. Hence, the huge amount of δ-electron signals distributes equally among many detector segments and can be discriminated from real heavy-ion detector signals more easily. For more details, please refer to figure III.4.

Despite of the noise-problematic due to detector technology (resistive strips, high capacity) further sources of noise are present with the TREX setup: Preamplifiers being located outside the vacuum chamber require quite long cabling to connect the silicon detectors to further signal-processing electronics. Especially, as these cables are partly unshielded they act in addition to the additional capacity the cable-length introduces, as antenna and pick up noise from the experimental site. Furthermore proper grounding between the various electronics processing modules of TREX and MINIBALL had always been an issue in previous preparations of the experimental campaigns. Some of these current limitations in TREX are significantly amplified towards higher beam energies.

Figure III.5 shows the influence of the beam energy on one-neutron transfer kinematics. With the HIE-ISOLDE upgrade, the beam energy significantly increased to $10\,\mathrm{MeV/u}$. This increase directly translates to the kinematic curves of the transfer protons, as it is shown in III.5a. Especially at backward angles ($\theta_{lab} > 90°$) the increased energy helps in terms of the detection threshold of the detectors, which have been always delicate with TREX. At forward angles however, the energy of the transfer protons increases to such high values, that it is likely that the protons (and elastically scattered deuterons from the target as well) punch through the

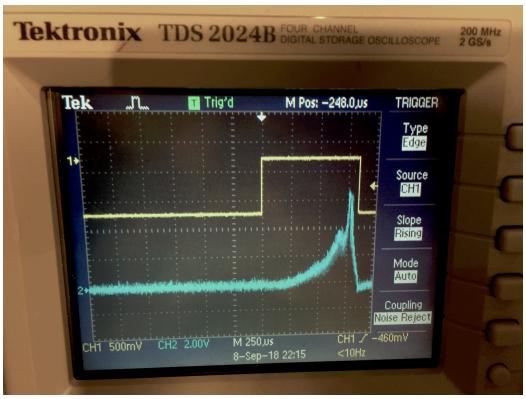

(a) Release-profile of the beam at the MINIBALL target position (blue) together with the EBIS-gate (yellow).

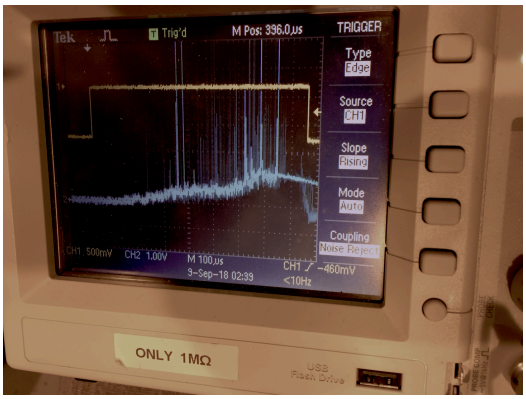

(b) EBIS-gate (yellow) together with the shaped energy signal (blue) in the forward barrel detectors with the beam being attenuated by a factor of 10.

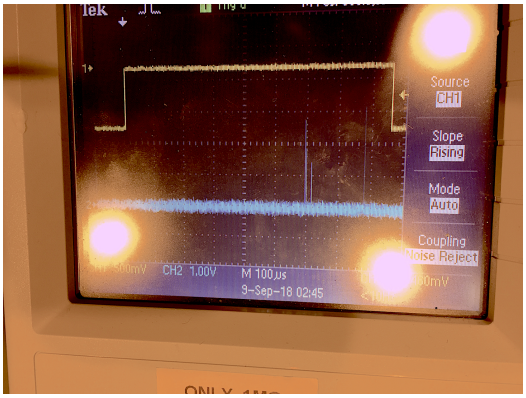

(c) EBIS-gate (yellow) together with the shaped energy signal (blue) in the forward barrel detectors with the beam being attenuated by a factor of 100.

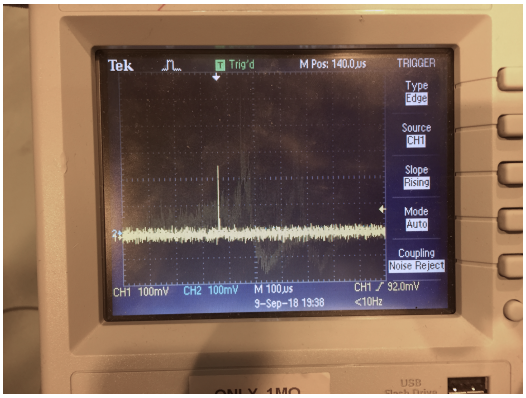

(d) Energy signal in the forward CD detectors with the beam being of similar intensity as in III.4b. Note the absence of a baseline shift.

Figure III.4: Various oscilloscope pictures showing the detector response of a ^{132}Sn-beam with 7.3 MeV impinging on a deuterated polyethylene target. In III.4b the baseline shift due to δ-electrons can be seen. The 'sharp' peaks on-top represent heavy-ion signals introduced in the resistive-strip detector. Some protection feature of the shaper due to the large macrosopic currents being induced, can be nicely seen as a straight (blue) line with constant negative slope (starting at a voltage level > 1 V with respect to the baseline).

whole ΔE-E telescope. This problem is shown in figure III.5b: The ungated ΔE-E spectrum shows data from the forward barrel region of TREX, measured during the

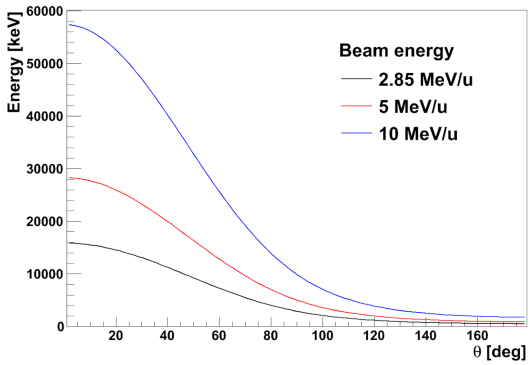

(a) d(^{132}Sn, p)^{133}Sn one-neutron transfer kinematics at three different beam-energies: 2.85 MeV/u, 5.0 MeV/u and 10.0 MeV/u .

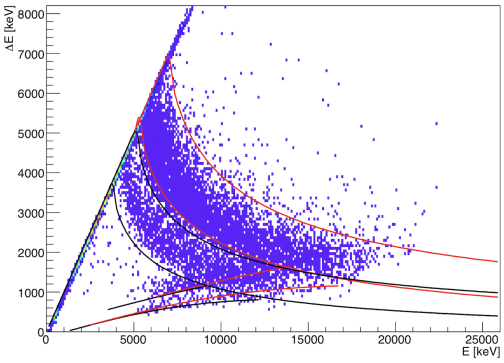

(b) Ungated ΔE-E spectrum acquired during the experiment d(^{134}Sn, p)^{135}Sn at a beam-energy of $E_{beam} = 7.3$ MeV/u (see section V.1).

Figure III.5: Influence of the beam energy in one-neutron transfer experiments. In the two-dimensional spectrum on the right, energy-loss splines, simulated with GEANT4 are shown: The black splines represent the location of transfer-protons in the spectrum, whereas elastically scattered deuterons are located within the red splines. One may note the overlapping of the back-bending splines due to punch-through.

experiment d(^{134}Sn, p)^{135}Sn at a beam-energy of $E_{beam} = 7.3$ MeV/u. Indicated as red and black splines are simulated energy-loss signatures from transfer protons and elastically scattered deuterons, respectively. On the first part of the branch, the particles which are stopped in the E_{Rest}-detector are located, whereas the back-bending branch shows the case that the particles punch-through the whole ΔE-E telescope. As shown, the backbending splines are overlaying and thus prevent particle-identification.

The basic limitations of TREX are summarized as follows:

- Insufficient energy resolution and reconstruction for close-lying states
- Intrinsic (electronics) noise: signal processing electronics and detector technology
- Background problematic: δ- and β-electron background, as well as electromagnetic pick-up
- Insufficient particle identification due to punch-through
- Rate capability of the data acquisition due to bunched ISOL-beam

III.4 Solutions: Trade-Offs and perspectives

For investigation of various effects like the thickness of the detectors or the target, the geometry and shape of the detectors, the beam-spot size, as well as physical aspects like the level density of the excited states for various heavy ions, or the type of transfer reaction, a detailed Monte-Carlo simulation based on GEANT4 [4] was used. With the 'show-case' reaction d(^{132}Sn, p)^{133}Sn at 10 MeV/u beam-energy various effects were studied. The experimentally measured excited states of ^{133}Sn have been simulated together with their corresponding angular distributions: Ground-state ($7/2^-$), 854 keV ($3/2^-$), 1363 keV ($1/2^-$) and 2005 keV ($5/2^-$) [46].

III.4.1 GEANT4 simulation: Thickness, particle identification and background suppression

Addressing the particle identification (PID) capability, various approaches have been evaluated. A naive approach would simply use a much thicker, unsegmented E_{Rest} detector. However, guaranteeing PID requires to completely stop elastically scattered deuterons in this E_{Rest} detector. This would require a silicon thickness of $\mathcal{O}(\sim \text{cm})$. Besides the fact, that such silicon-thicknesses are highly non-standard in industrial manufacturing, this new type of thick sensors would need to be fully characterized (carrier mobility, charge trapping, depletion, ...) before being able to be used in scientific experiments. Another approach would use scintillation detectors, however it was decided to stay with one detector technology. Inside the compact MINIBALL target chamber, space is limited and silicon sensors provide best capabilities for charged-particle tracking and energy measurements.

Extensive Monte-Carlo simulations suggest the construction of a completely new detector array with additional silicon detectors: The most obvious change with respect to the present TREX setup was the approach to use a third layer of silicon, enabling a twofold ΔE-E particle identification method. By simply mounting a second E_{Rest2} in close succession, additionally to the ΔE-E_{Rest} PID cut, a second E_{Rest}-E_{Rest2} cut is possible. In figure III.6, the result of a realistic GEANT4 simulation exploiting the idea of a triple-stack detector setup is shown. The setup comprises a 100 µm thin, segmented ΔE detector followed by two unsegmented 700 µm thick E_{Rest} detectors. The geometry of the detectors, the PCB/protection foil/vacuum chamber/... layout was chosen identical to the existing TREX-setup by means of better comparability (see also figure III.8a).

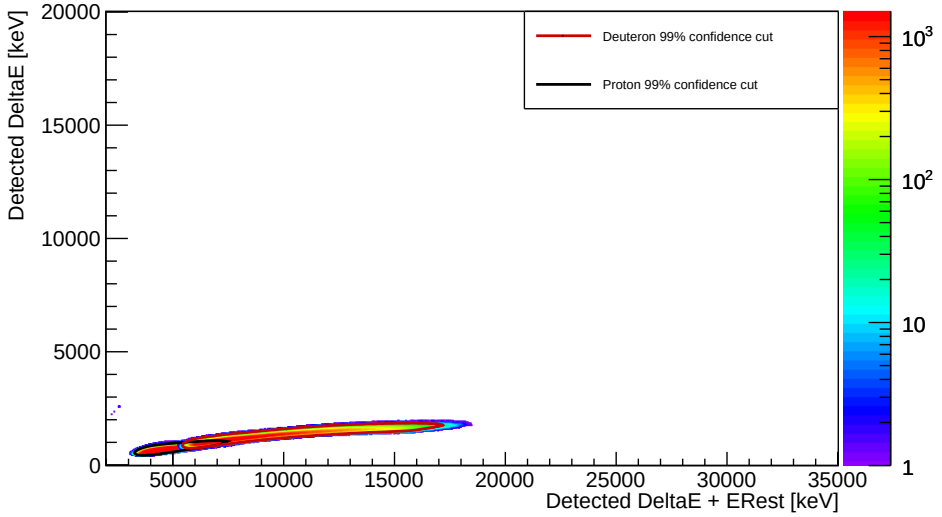

(a) First PID cut using the thin 100 µm, segmented ΔE detector and the first 700 µm thick E_{Rest} detector.

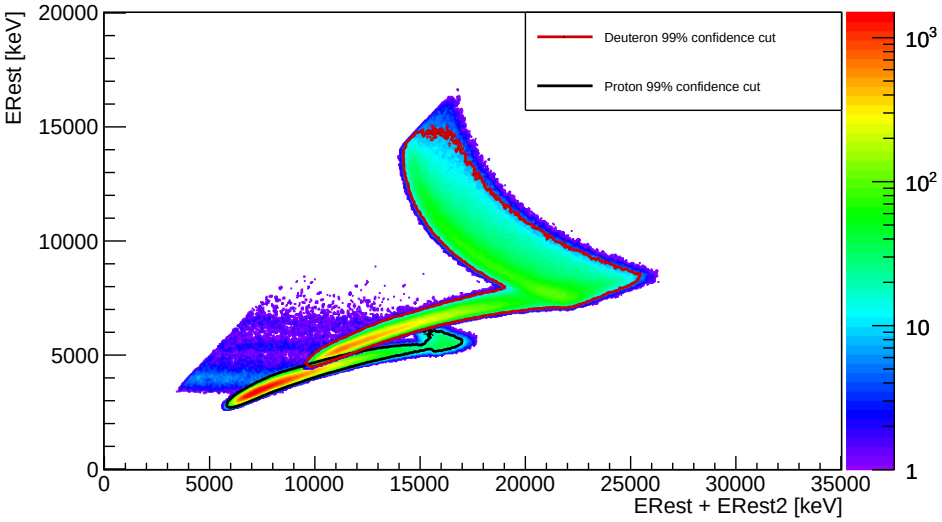

(b) Second PID cut using the first 700 µm thick E_{Rest} detector and the second 700 µm E_{Rest2} detector.

Figure III.6: Addressing the punch-through problematic by using a twofold ΔE-E particle identification method.

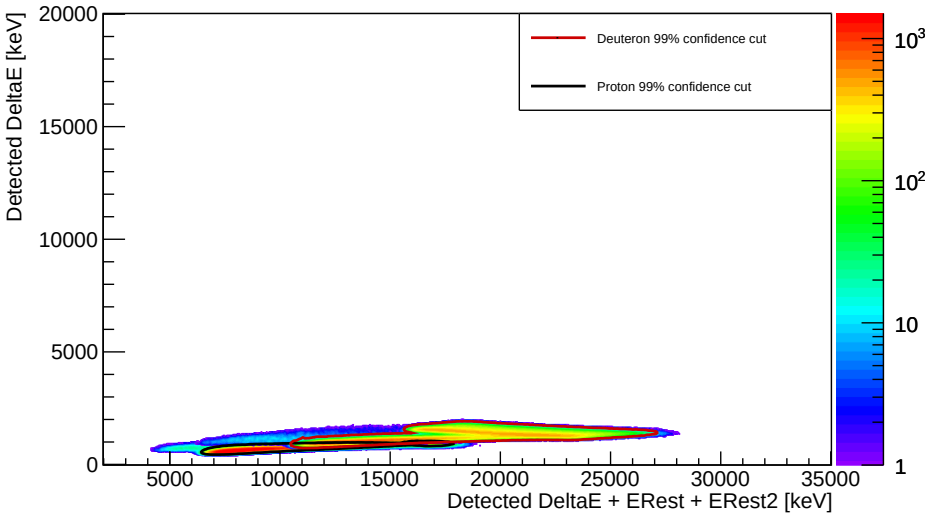

(c) Third PID cut using the ΔE detector and the sum of both E_{Rest} detectors.

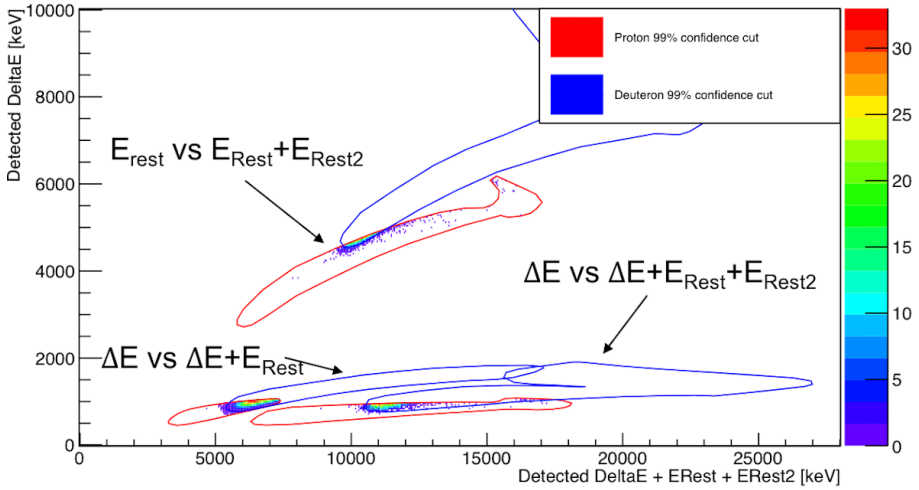

(d) All energy-loss PID cuts, each filled with mis-identified, elastically scattered deuterons.

Figure III.6: Addressing the punch-through problematic by using a twofold ΔE-E particle identification method (cont.). Transfer protons and elastically scattered deuterons from the 'show-case' reaction d(^{132}Sn, p)^{133}Sn at 10 MeV/u beam-energy are shown together with contour lines representing the 99% confidence cuts, used to determine the PID capabilities of the three-layer system. This method reduces the number of mis-identified deuterons as transfer protons to an unprecedented value of $\lesssim 1.2‰$. The horizontal bands visible in III.6b and III.6c are due to particles hitting the edge of the second E_{Rest} detector. These bands can be removed by an appropriate geometrical cut.

The values for the thickness of the detectors was chosen as a trade-off between physics requirements, technical feasibility and economical aspects. For the unsegmented E_{Rest} detectors mainly economical and technological aspects constrained the upper limit to 700 µm thickness. Furthermore it was decided to stick to one E_{Rest} thickness for both detectors by means of simplicity and uniformity. As for the ΔE detectors: their thickness is far more crucial for a successful PID in radioactive beam experiments. Generally speaking, the thinner those segmented detectors are, the lower is the cut-off threshold for low-energetic PID. Especially in one-neutron transfer reactions investigating not only (d,p) reactions, but also for instance (^{3}He,d), (α,t) or (^{7}Li,^{6}He) reactions and in every further type of transfer reaction involving higher-Z nuclei to be detected with the silicon array, the ability to perform PID with low-energetic, heavy ions is a clear advantage. The existing TREX-setup uses 140 µm thick resistive strip detectors. Producing such type of detectors with 100 µm thick silicon (or even less thickness) is technologically possible.

Simulating the punch through particles from the above mentioned 'show-case' reaction d(^{132}Sn, p)^{133}Sn at 2.85 MeV/u, 5 MeV/u and 10 MeV/u beam energy with the existing TREX-setup leads to a number of 42.1% of elastically scattered deuterons lying inside the transfer proton 99% confidence cut. Applying the idea of a two-fold PID (according to figure III.6) with the silicon sensor thicknesses as previously discussed, a deuteron suppression factor of $\gtrsim 350$ in the proton 99% confidence cut can be achieved. The ability to discriminate transfer protons from elastically scattered deuterons is very essential for the forward region of the detector array as the elastics are the dominant background in this type of nuclear reaction.

In further GEANT4 simulations, the influence of the β and δ electrons was investigated closer. A gaussian distribution of electrons with a mean of 1 MeV and a sigma of 500 keV was shot from random angles onto different silicon sensor thicknesses.

In table III.2 the results of the GEANT4 simulation are listed. The energy depositions have been fitted with a landau function and the most probable value (MPV) was extracted. The results clearly prefer 100 µm detectors in terms of background suppression by applying a cut-off threshold. Hence, even highly excited states can be detected in the very backward region down to $\approx$ 200 keV.

Table III.2: Results from the electron simulation with GEANT4.

Silicon thickness	Mean of energy deposition	MPV of landau fit
100 µm	124.4 ± 0.5 keV	62.0 ±0.2 keV
150 µm	167.6 ± 0.8 keV	77.4 ±0.3 keV
300 µm	174.8 ± 0.6 keV	125.5 ±0.6 keV

Next to the background suppression by having simply less energy deposited by

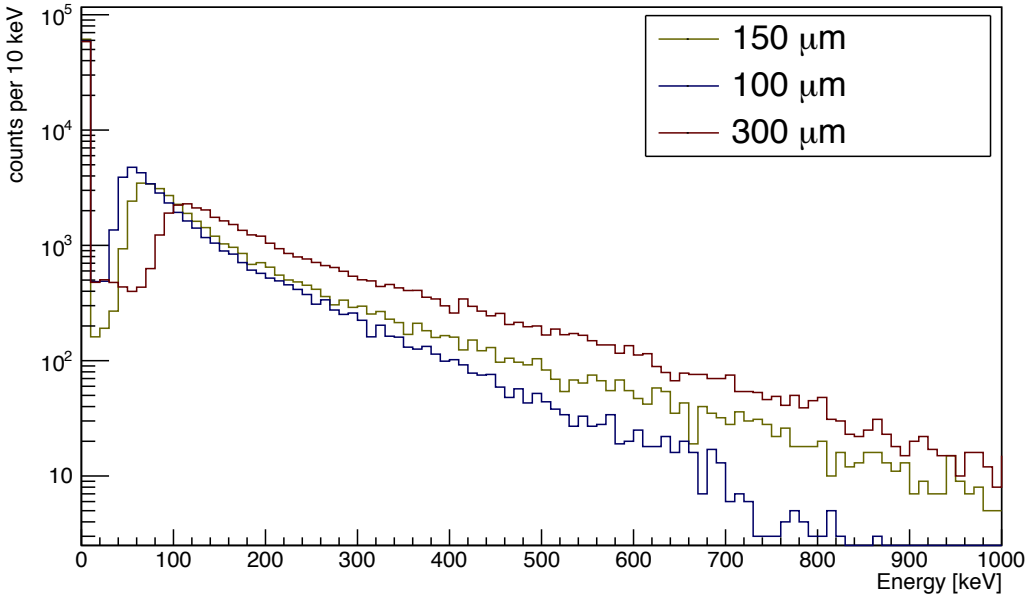

Figure III.7: Energy deposition in 300 µm (red), 150 µm (green) and 100 µm (blue) silicon thickness. An electron source having a gaussian distribution around 1 MeV with a sigma of 500 keV was simulated.

the electrons in the sensors due to a reduced silicon thickness, the idea of having a triple-stack of sensors helps a lot in further electron background suppression: As the electrons undergo multiple scattering processes in the silicon, their energy is not necessarily deposited in one detector-stack mounted in close succession. Hence, by applying an additional E_{Rest}-E_{Rest2} cut for particles having enough energy to punch through both ΔE and E_{Rest} detectors and requiring the energy to be deposited in only one triple-stack, the electron contribution to the energy measured in the ΔE detector can be further reduced.

Further measures and probably the most effective ones against the electron distortions, as described in section III.3 and illustrated in picture III.4d, is the reduction of the physical detector area by increasing the granularity in the silicon-array according to the next subsection III.4.2.

III.4.2 GEANT4 simulation: Granularity and target thickness influence

As the measurement of the energy of the states excited in transfer reactions is done indirectly via the reaction kinematics, the angular resolution in θ is crucial for determining the resolution power in terms of energy of the silicon array (see figure

III.8 for more details). Simulations have been done for both, the current TREX-setup and the upgraded version HI-TREX (see chapter IV for further information). For the further discussion we assumed a compact and symmetric detector geometry as outlined in figure III.9. This is based on trapezoidal double sided silicon strip sensors (DSSSDs) with a granularity of at least 128 (θ) x 8 (ϕ) strips. On the junction side facing the target, p strips on n-bulk Silicon are located orthogonally to the height of the trapezoid. The position resolution of these directly translates to the angular resolution in the polar angle θ. On the ohmic side, the n^+ contacts will be separated using the p/p^+ stop technology. The layout of these ϕ-strips will be a fan-out from the small base of the trapezoid to the larger one, with a constant ratio of the large and small pitches from the bases.

For the reconstruction of excited states in a transfer reaction, the granularity of the detector array plays as an important role as the target thickness. The energy straggling of the beam and the light transfer products in the target is an additional limitation for high Z beams: Assuming 64 Barrel strips, the energy resolution of the ground state in backward direction in the angular bin closest to $\theta_{lab} = 90°$ deteriorates from 86 keV (FWHM) by a factor of ≈ 3 for an increase of the target thickness by a factor of 5 to 0.5 mg/cm^2. These values were simulated for the HI-TREX setup. Note, that the angular/energy resolution has to be as similar as possible over the whole angular range to avoid the strong broadening towards $\theta_{lab} = 90°$ as it is observed for the current TREX setup (compare figure III.8). Without the use of gas targets, the energy straggling on the target carrier material and thus the energy resolution can only be improved by decreasing the target thickness. Hence, a compromise between energy resolution and maximising the statistics with a thicker target has to be found individually for each experiment.

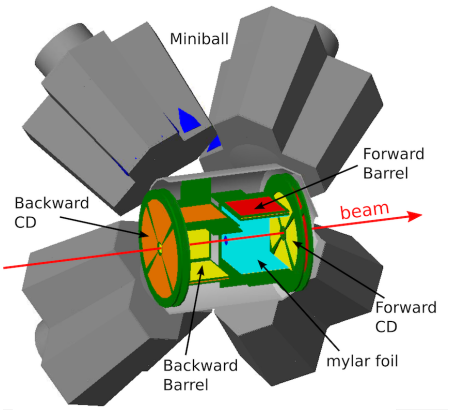

(a) Current TREX setup.

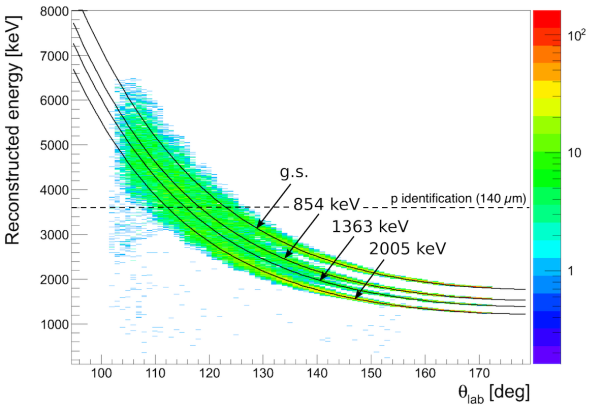

(b) Existing Barrel detector response with 16 strips in θ-direction.

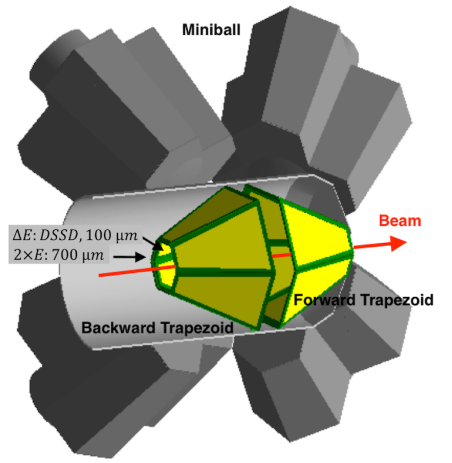

(c) HI-TREX-setup.

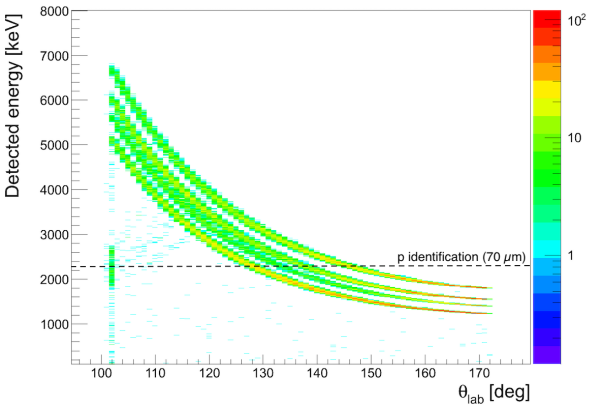

(d) DSSSD segmentation of 128 θ-strips and 8 ϕ-strips.

Figure III.8: GEANT4 simulations of the reaction d(^{132}Sn, p)^{133}Sn at 10 MeV/u beam-energy. A target thickness of a deuterated Polyethylene foil of 0.1 mg/cm^2 was used. The reaction kinematics of transfer protons in backward direction was simulated for the current TREX setup, as well as for the upgraded HI-TREX setup (see chapter IV for more details). The influence of the θ-segmentation on the energy resolution of excited states can be nicely seen. ϕ-segmentation only adds a minor contribution. For illustrative purposes, the proton identification threshold by PID for 140 µm vs 70 µm detector thickness is indicated as a dashed line. Note the almost uniform energy resolution over the whole angular range compared to the strong broadening towards 90° for the current TREX setup.

III.4.3 Geometrical optimisation and basic electronics requirements

The very basic constraint on the new silicon array is the adaptability to the existing MINIBALL γ-array. As the MINIBALL efficiency is the limiting factor in particle-γ coincidence measurements, it was decided to stay with the existing cylindrical target chamber for transfer experiments. Hence, the emphasis in the design phase of the HI-TREX array was set on achieving a compact setup featuring a minimum amount of material. The cylindrical TREX vacuum chamber has an inner diameter of 14 cm and a wall thickness of 2 mm. The volume of the target chamber is basically restricting the geometry of the HI-TREX setup.

As for the γ-ray detection, maximum efficiency for the charged particle detection is envisaged. Altough some constraints need to be made as the silicon array will be positioned inside the vacuum: Enough entrance and exit space at the forward and backward hemisphere for the beam needs to be guaranteed in order not to destroy the silicon membranes by scattered beam. Also, some space for the target mechanics needs to be cleared. Furthermore it is wise to optimise the solid-angle coverage to regions of most interesting physics. As can be seen in figure II.6, for the one-neutron transfer reaction of ^{132}Sn to ^{133}Sn at 10 MeV/u, the most pronounced difference in the differential cross section is expected around $\theta_{lab} = 90°$. Hence certain effort was made to keep the 'blind region' around the target as small as possible. Furthermore, most statistics is expected around this region: the most forward angles are dominated by Rutherford scattering, whereas the most backward angles are suffering from extremely small solid angle coverage in the centre-of-mass system.

Altogether the concept of having a symmetrical, hexagonal arrangement of trapezoidal-shaped detectors was a trade-off between the aforementioned constraints and the following parameters: Maximising the distance of the sensors to the target, together with optimising their placement inside the vacuum chamber in order for the normal of the centre region of the detectors to point directly at the target-direction ensures best angular resolution (this can be seen in the almost uniform resolution over the whole angular range, as depicted in figure III.8d). Furthermore maximising PCB-space is crucial for further signal processing electronics, which needs to be placed close to the sensors. Additional technological limits like the availability of only a 4-inch production line for the development of this new type of detectors, introduces constraints on the maximum detector area available. Detailed SolidWorks [85] CAD-drawings and simulations finally evolved to the setup shown in figure III.9.

The increase in granularity to $\approx$ 2000 readout-channels in the full setup, requires the electronics concept to be reevaluated: the use of standard readout-electronics, placed outside the vacuum chamber is no longer feasible. There is the requirement of a high density readout-system being able to cope with several thousand signals,

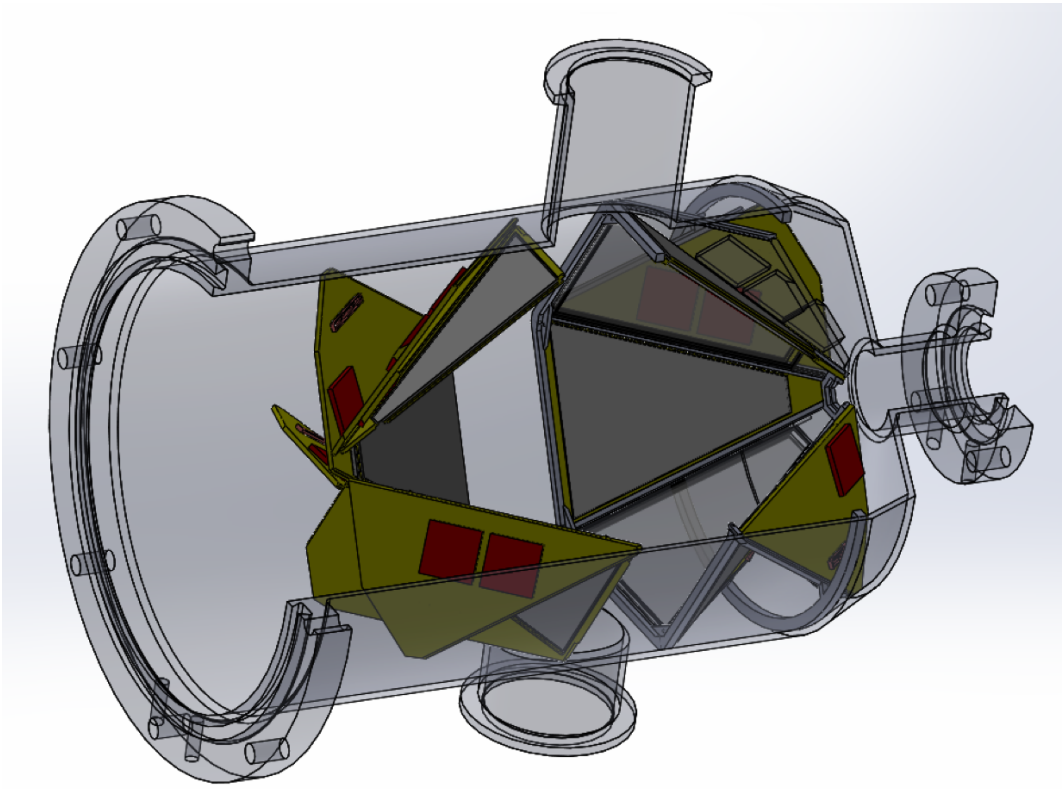

Figure III.9: HI-TREX setup fitted into the existing vacuum chamber of MINIBALL. In grey, the trapezoidal detectors together with the holding structure are shown. Green coloured parts represent PCB-space, whereas the red parts indicate the size of the application specific integrated circuits (ASICs) used for signal processing. The beam is entering from the right side. The top and bottom flange are used for target change and positioning.

while retaining good resolution and throughput and also being cost-effective. The only choice is to use an ASIC-based solution, while some additional constraints like the low material-budget inside the target chamber of MINIBALL limits the amount of possible ASICs drastically. Further constraints are discussed below.

The requirement concerning the equivalent noise charge (ENC) was set to a value below 10 keV, which is challenging but not unfeasible, as in-house measurements with the APV25-S1 ASIC [52] showed an energy resolution of $\sigma_E \approx 5 \ldots 7$ keV. The lack of any precise global trigger at TREX adds another requirement of having a capability of self-triggering to the ASIC demands. Additionally, the trigger-threshold

should be tuneable individually for each channel and should be able to be set as low as possible without triggering on noise.

Minimising externally induced noise, resulting from cable lengths, signal distortions, etc. is therefore very crucial and consequently the ASIC should be put as close to the detector as possible. This however imposes another constraint as on the one-hand side the ASIC has to be radiation hard, or at least radiation tolerant when being operated in very close distance to the target. And, on the other-hand the power consumption has to be as low as possible. To be able to run the ASIC at room temperature in vacuum without active cooling, where mainly radiative cooling and very little conductive cooling via the PCBs or the mechanical holding structure is possible would be the optimum solution.

Moreover, the beam structure at HIE-ISOLDE is governed by the super cycle of the PS-Booster and the charge-breeding in the REX-EBIS resulting in a bunched structure. During a beam-crossing, an instantaneous reaction-rate, which is nearly two orders of magnitude higher than the average rate, needs to be handled, whereas in 99% of the time between two bunch crosses, the ASIC basically can be powered off.

By using very specific ASICs (section IV.2.1), a custom-made readout-electronics (section IV.2.2.1) is mandatory. This guarantees maximum control, optimal integration and usability. This type of frontend electronics was developed simultaneously with the ASIC-development.

As for the backend electronics: the DAQ-integration into the powerful, existing TRB3-system (section IV.2.3) refurbishes joint-efforts in DAQ- & Software-developments which were originally undertaken by the HADES-collaboration. Reusing the existing infrastructure is not only cost-effective, but also ensures future support.

To summarize, the following developments, which are detailed in the following chapter, for HI-TREX have been done:

- Detector development
  - DSSSDs
  - Triple-stack
- Electronics development
  - Very-Front-End: ASICs
  - Front-End: GEAR
  - Back-End: TRB3
  - Peripheral components
- Integrated Setup with auxiliary components

Based on calculations, realistic simulations and experience with radioactive-beam experiments the proposed solutions for an upgrade of TREX to HI-TREX account for new experimental & technological needs accompanying the next-generation RIB-facility HIE-ISOLDE. Together with higher beam energies and intensities the frontiers of nuclear-(astro-)physics experiments are pushed further.

CHAPTER IV

HI-TREX: A highly integrated setup for transfer experiments at REX-HIE-ISOLDE

HI-TREX is the acronym for a highly integrated setup for transfer experiments at REX-HIE-ISOLDE. HI-TREX is the upgraded successor of TREX. As there is a close interplay between a detector and its electronics, the main upgraded components feature two basic developments going hand-in-hand with each other: The silicon detector upgrade and the accompanying custom made electronics. For the first part, the newly developed, very thin, AC-coupled DSSSDs are a technological novelty and many efforts have been made by the sensor supplier CiS in meeting the specifications later-on detailed in this chapter. A concept for the triple-stack setup has been evaluated together with the sensor supplier.

As for the electronics part, the integration of custom-made ASICs has been done successfully by the GEneric Asic Readout board (GEAR), which was developed within this work. The back-end integration, as well as the development of any peripheral components resulted in a working prototype for the full HI-TREX setup.

IV.1 Silicon sensor development

There are various silicon sensor suppliers available on the market. However, most of them produce in large scales for industrial applications. Therefore, the large number of companies reduces to quite a small amount in the present case, as the production of only one or two batches of wafers is not economical for most of them due to the large overhead of R&D. Thereby we are happy having found the supplier CiS, which is interested in developing and producing these new type of DSSSDs, as well as the E_{Rest} detectors, whose thickness is non-standard for industrial production as well.

IV.1.1 Position-sensitive detector development

The basic design decision concerning the detector type for charged particle identification was guided by the experiences gathered in various transfer experiments with TREX at CERN/ISOLDE. The details as described in chapter III led to the decision using DSSSDs instead of the previously used resistive strip type detectors. With the definition of the detector type, further details need to be specified: the type of bulk material and hence the type of implantation, the method of biasing the detector, the pitch and layout of the segmentation, the geometry, bulk-thickness and thickness of the individually processed layers, as well as the coupling of the detector to the readout electronics. As many parameters go hand-in-hand with all the various processing steps, it is in most cases reasonable to specify only upper or lower limits, respectively ranges in which the parameters can be tuned.

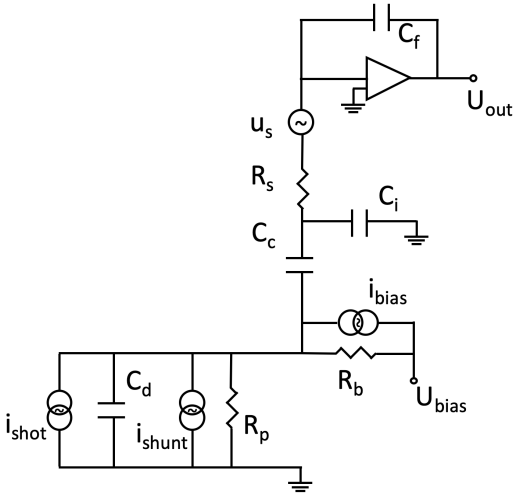

(a) Equivalent circuit diagram for a capacitively coupled detector connected to a charge-sensitive amplifier.

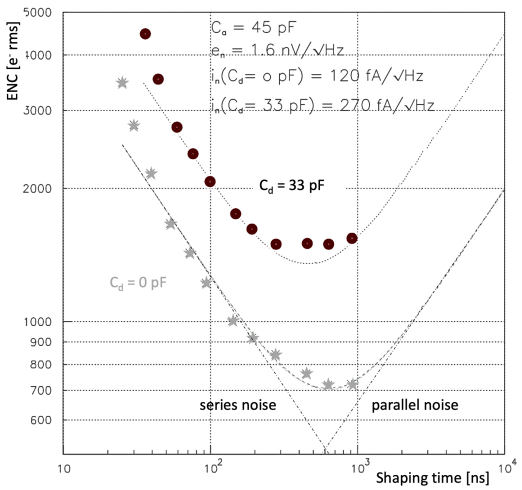

(b) ENC vs shaping time for the SKIROC2A ASIC. Figure adpated from [20].

Figure IV.1: In the equivalent circuit diagram, the detector is represented by the capacitor C_d with a resistor R_p in parallel. Both components introduce noise current sources, as does the biasing network, represented as R_b. The detector is AC-coupled via the capacitor C_c and connected to the input-stages of the charge-sensitive preamplifier by a serial resistor R_s introducing a series voltage noise source, together with a peripheral capacitance of the connection C_i.

General noise consideration in silicon strip detectors: Noise can be considered as a macroscopic result of microscopic random processes. A thorough analysis of noise is quite complex as it is a close interplay of many noise sources: noise in the

basic detector, the front-end ASIC input stages, the current sink for the detector leakage current and the biasing network. Additionally, noise in detector strips cannot be treated individually as neighbouring strips influence each other due to the built-in interstrip capacitances and the shaping time constant of successively used shapers influence the noise performance of a system as well. A comprehensive overview of the various noise sources in silicon strip detectors can be found in [58]. Detailed consideration of each contributing noise source leads to the expression for the equivalent noise charge (ENC [1]) [36, 73]:

$$ENC^2 = \frac{\mathrm{d}i^2}{\mathrm{d}f}\tau a_1 + \frac{\mathrm{d}u^2}{\mathrm{d}f}(C_d + C_i + C_f)^2\frac{a_2}{\tau} + (C_d + C_i + C_f)^2 A_f. \tag{IV.1}$$

The constants a_1 & a_2 are shaper-specific constants. τ represents the shaping time and A_f is a constant expressing the exact $1/f$ power noise spectral density, and does not depend on the filter involved. This low-frequency $1/f$-noise cannot be reduced by changing the shaping time unlike the series voltage noise contribution, which decreases with increasing shaping time. However, low parallel capacitance C_i, C_f, C_d is required for optimal ENC-values, as the parallel current noise contribution from the leakage of the detector is limiting the maximum shaping time. The effect of the shaping time on the ENC and the influence of the detector capacity C_d can be nicely seen in picture IV.1b ($C_i = 45\,\mathrm{pF}$ and $C_f = 6\,\mathrm{pF}$). To summarise: In order to achieve a high signal to noise ratio in silicon detectors following conditions are important:

- Low leakage current $\rightarrow$ high value for the biasing resistor
- Short and low resistance connections to the amplifier $\rightarrow$ reduces peripheral capacitive losses
- Low detector capacitance $\rightarrow$ optimised for the required input capacitance of the preamplifier
- Optimum shaping times $\rightarrow$ need also be matched to the expected hit-rate

AC-coupling preferred due to noise: High leakage current of sensors is the source of shot noise in front-end electronics. High amplifier currents distort signal shape and affect the linearity and dynamic range of analog circuits. Alternative/Capacitive coupling (AC) uses a blocking capacitor in series with the signal between implants and the front-end ASIC and is one possible solution to improve on noise issues, especially after irradiation, as it blocks a constant leakage current from the detector to the amplifier. Furthermore the capacitor decouples the potential of the operating electronics from the detector potential. Integration of coupling

[1] The ENC is a measure of the input charge in e^- into a preamplifier for which the output of the shaper results in a signal-to-noise ratio $S/N = 1$.

capacitances is performed in a standard planar process and is basically done by depositing insulators like SiO_2 or Si_3N_4 (see figure IV.2).

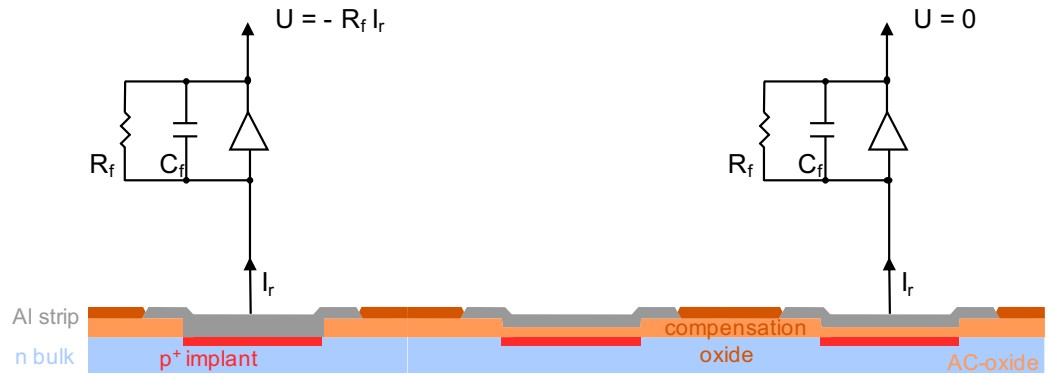

Figure IV.2: Direct and capacitive coupling of electronics to the detector. With direct coupling (DC; left) the detector reverse bias current I_r has to be absorbed by the electronics. With capacitive coupling (AC; right), only the AC part of the detector current reaches the electronics, while the DC part goes into the biasing circuit, in this case via the p^+ implants.

p^+-implanted wafers due to simplicity: The use of *p*-in-*n* type or *n*-in-*p* type detectors defines directly the processing steps during sensor manufacturing, as well as the input polarity of the ASIC preamps, respectively the layout of the strip geometry. The benefit in using *n*-in-*p* type detectors is the missing type-inversion of the bulk material, due to heavy irradiation. The principle source of radiation damage in silicon sensors is from non-ionising energy-loss, which effectively converts the material from *n*- to *p*-type and thus results in increased leakage currents. As shown in [2] *n*-in-*p* type sensors do not show non-gaussian noise effects related to high electric fields, as *p*-in-*n* type sensors after irradiation do. Furthermore their performance is similar to standardly available *p*-in-*n* type detectors. However, these detectors using *p*-bulk material are only currently developed, e.g. for the high-luminosity upgrade of the CMS-tracker at the LHC. Hence, as the expected radiation dose is far below the ones at the LHC-detectors and as the technology is not as well established for producing sensors for heavy-ion detection, the decision made together with CiS was to stay with *p*-in-*n* type detector technology. Furthermore, the resistivity of the *n*-type bulk material together with the overall thickness defines the necessary depletion voltage of the sensor. For HI-TREX, low resistivity material of 800 Ω cm . . . 1200 Ω cm is required to guarantee proper biasing.

Biasing done via poly-silicon: There are two possible ways of biasing the implant-

strips: Technologically more challenging poly-silicon resistors or space-saving punch-through biasing. The two technologies are illustrated in figure IV.3.

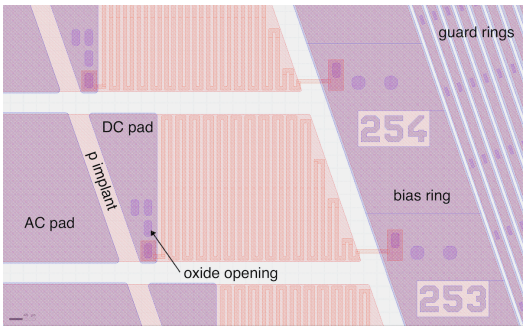

(a) Poly-Silicon resistors (orangeish) as manufactured on the TOP-side (p^+-side) of the HI-TREX wafers. The reddish shaded area depicts the p^+ implant and the blueish colours represent metallisation for the DC- and AC-pads. Oxide openings for contacting the bias to the implant are shown additionally.

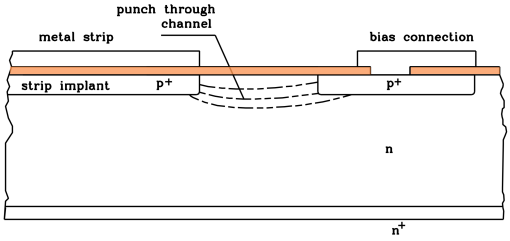

(b) Punch-through biasing structure. The outer (orange) oxide surface voltage adjusts to such a value that the punch-through current flows at finite depth across a potential barrier from the strip to the bias structure. Adapted from [58].

Figure IV.3: The two major types of biasing strip detectors.

Punch-through biasing depends on the potential that is established on the surface of the decoupling oxide. For differing potentials of the metal strip and the biasing electrode (see schematic IV.3b for details), which is the case when a particle has hit a specific strip and thus free charge carriers are generated, a surface voltage gradient will be compensated by the usually uncontrolled surface resistivity of the oxide. This can take a very long time until equilibrium is reached [58]. The delicacy of reducing dead area of the detector together with the simplicity of manufacturing such structures (no additional masks & annealing steps are required) is compensated by the fact, that this type of biasing shows severe increase of leakage current after irradiation, contrarily to sensors biased via poly-Silicon resistors [99]. Poly-silicon resistors on the other hand require additional processing steps: the deposition of the amorphous silicon as well as the annealing of the silicon needs to be done. The last step however needs to be carried out with care, as in the case of the HI-TREX sensors, as described below, the required very shallow implant thickness depends sensitively on the overall annealing time and temperature. Hence this processing step needs to be done before any implantation can be made. This consequently means, that the p^+ acceptors need to be implanted through the already deposited AC-coupling oxide. Furthermore, for a certain resistance of the poly-silicon meanders, a certain length is required which reduces the available active detector area compared to the

space-saving punch-through biasing. The typical value for the sheet resistivity of poly-Silicon meanders as produced for the HI-TREX wafers is $\approx 5\,\mathrm{k}\Omega/\square$. Hence ≈ 1000 squares (or approx. a 0.5 cm long meander with a width of 5 µm) are needed for a biasing resistance of 5 MΩ. Experience with other DSSSDs showed that a biasing resistance value of 5 MΩ . . . 15 MΩ is a good trade-off between low-noise and recovery time of the strip potential at high hit-rates of the strips. A set of guard-rings reduces the field strength at the edge of the detector. Further specification is the minimum/maximum biasing voltage of $20\,\mathrm{V} < U_b < 200\,\mathrm{V}$, which can be handled quite easily in a standard way. Hence, with the (low) resistivity values of the n-bulk material (for values see above) and the thicknesses of 100 µm, 70 µm and 50 µm, U_b is expected to be within 42 V . . . 28 V, 20 V . . . 14 V and 11 V . . . 7 V respectively.

Geometry, strip layout and granularity of the sensors: The trapezoidal geometry of the sensors was chosen according to the requirements described in subsection III.4.3. Further constraint was the need of additional space around the outer detector dimension for etching cavities due to the membrane thickness (greenish area in figure IV.4). Metallisation/implanted areas are shown in blueish colours. Poly-Silicon resistors are depicted orangeish. The straight, greyish lines show the (laser) cutting contours for separation of the detectors. All structures outside these greyish lines are for testing and evaluation of the manufacturing process. The outer dimension of the DSSSD are 60.420 mm (major), 10.643 mm (minor) and 71.640 mm (length). The centres of the active area and the detector outer dimensions do not coincide exactly, because the bias supply on the TOP side is only on the right side of the trapezoid (as shown in IV.4a) and the supply on the BOT side is only on the major side. However, the two vanishing points of the outer dimensions and the active area do coincide, which is the important information concerning angle determination and effective thickness reconstruction in an experimental setup. Generally, the trapezoidal design enables multiple geometrical arrangements in various 4π configurations and thus enables a generic usability of the detectors for a variety of experiments.

The strip layout was chosen perpendicular on the front with respect to the back side. On the junction side (IV.4a), the *p*-implant strips are located horizontally and are parallel to each other. Their length varies from 5.70 cm to 0.89 cm. The ohmic side (IV.4b) features a fan-out of the strips from the minor to the major of the trapezoid, each detector segment being equal in size and having an average length of 6.89 cm.

As for the granularity, the largest pitch is defined by the GEANT4 simulations shown in subsection III.4.2: At least 128 strips in θ-direction, which translates to the TOP side of the wafer are required and in ϕ-direction with a minimum of 8 strips, sufficient results can be expected for transfer experiments with HI-TREX. In the sense of developing a generic detector for many applications, having maximum granularity is beneficial, as the granularity can always be decreased easily by wire-bonding multiple detector segments together. Hence, the minimum pitch is defined

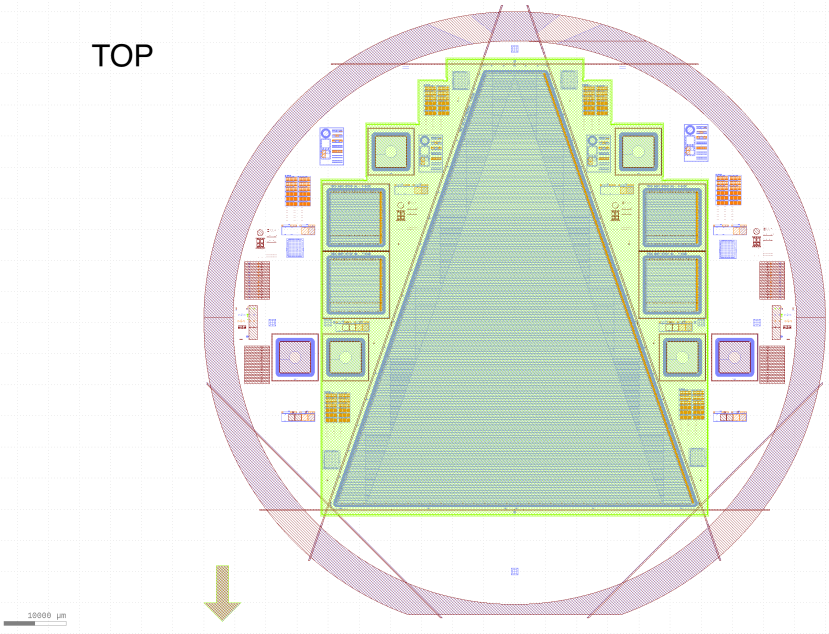

(a) TOP (junction) side of the HI-TREX wafer.

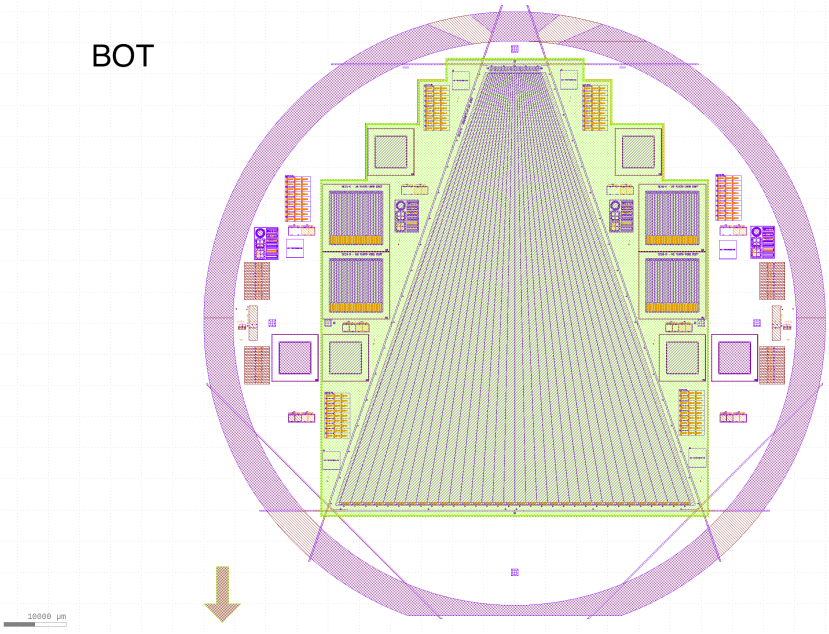

(b) BOT (ohmic) side of the HI-TREX wafer.

Figure IV.4: Layout of the HI-TREX wafer with some masks being shown in different colours. Refer to the text for more details.

by the requirements on the thickness of the dead-layer as discussed later-on: It is the thickness of the metallisation being equal or less than 20 nm, which is required due to energy straggling. The shaping time of the ASICs define the maximum signal propagation time along a strip to be < 30 ns. The approximate strip capacitance of a 70 µm thick detector with an implant width of 250 µm is $\approx 3.7\,\mathrm{pF/cm}$.

Taking into account the measured sheet resistivity of AlSi[2] of $\approx 0.05\,\Omega\,\mathrm{mm^2/m}$, the value for the relative strip resistance amounts to approx. $100\,\Omega/\mathrm{cm}$, which is well within a safety margin of a factor of ≈ 8 for the signal propagation time. Therefore it was decided to process a pitch of 260 µm on the p-side resulting in 266 strips on the front. On the n-side, due to the fan-out of the strips, the pitch on the minor was chosen to be 265 µm (on the major this pitch results in 1766 µm), resulting in 32 strips.

Membrane-thickness: The detailed GEANT4 simulations as shown in section III.4 show the clear preference for the detectors being as thin as possible due to the PID and electron problematic. As sensor thicknesses below 100 µm would be a novelty for AC-coupled DSSSDs and thus requiring much R&D efforts from the sensor supplier CiS, our needs can make good use of their LAT[3] project. Target thicknesses of 100 µm, 70 µm and 50 µm have been specified to be etched from an original wafer thickness of 285 µm.

The achieved uniformity is below ± 1 µm. This superb value is due to the technology being used: The SOI (Silicon On Isolator) technology uses wafer bonding to produce a layered silicon-insulator-silicon substrate. This SOI wafer stack is then used to wet-chemical-etch to the desired target thickness, having the oxide as a very well defined etch-stop and thus guaranteeing a smooth surface for further processing steps after insulator removal. Furthermore, the remaining SOI wafer outside the etching-cavity is required to act as handling wafer for further processing steps, which is crucial due to the thinness of the detectors. Successful pre-tests of the individual processing steps with all three target thicknesses led to the decision on the final DSSSD thickness of being 70 µm, which really is a novelty for AC-coupled, industrially manufactured, double sided sensors.

Entrance window considerations: The entrance window of the detectors is defined - in this case - as the overall inactive layer of the working detector, the particles need to overcome in order to reach the active volume of the sensor. As the ions already loose energy in this dead-layer, the thickness is desired to be as thin as possible, to keep the energy straggling of the particles as low as possible and furthermore enable also measurements of high-Z ions with little energy. On

[2] For the metallisation, not pure aluminum is used, but mixed with a small fraction ($\approx 3\%$) of silicon, which enhances its adhesion compatibility with SiO_2 and reduces electromigration effects.

[3] The project LAT (Large-Area Thinned Radiation Detectors) explores the technology of wet-chemical etching of cavities and was successfully applied to large-area radiation detectors for the first time. The project is funded by the Federal Ministry of Economics and Energy (FKZ: MF 140163).

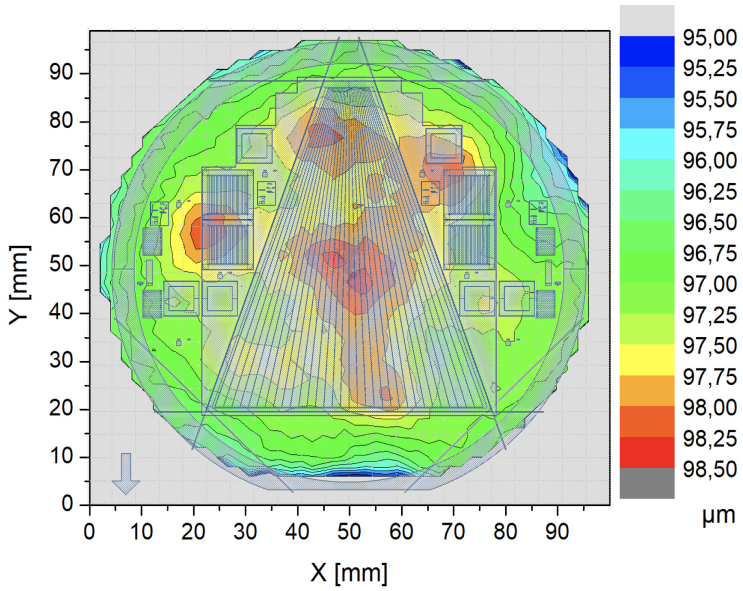

Figure IV.5: Result of the KOH-etching process of a complete wafer with a target thickness of 100 µm. The etching and thickness measurements were done by CiS. The backside metallisation mask, as well as the rough cavity dimensions are superimposed.

the front-side of the detectors, the contributing layers to the overall dead-layer thickness are the p-implant, the AC-coupling insulator, and the metallisation. As the strip-pitch was chosen to match the required relative resistance of the metallisation layer being 20 nm thick, which is close to the minimum possible thickness, the parameters of the oxide thickness and the depth-distribution of the p^+ implant remain to be tuned. As for the decoupling oxide, its maximum thickness is defined by the capacitance of the AC-coupling, which should be able to collect all the generated charge carriers of an event. This means, that the decoupling capacitance C_c should be much larger than C_d: $C_c \gg C_d$ (at least two orders of magnitude). The minimum oxide thickness is defined by the possibility to deposit such thin structures and their resulting uniformity, without introducing so-called pin-holes, which result in a missing AC-DC isolation of the strips. Pin-holes are a fundamental issue for detector operation. However, due to the specific ASIC being used, which has the feature of possible deactivation of the preamplification stage of single channels, scattered pin-holes do not distort the performance of the rest of the detector. Furthermore, the thickness of the oxide noticeably influences the implantation profile of the acceptors, as due to the manufacturing process, the boron acceptors will be implanted through the oxide and need to diffuse into the bulk material and be activated by thermal

annealing. As a shallow profile for the implantation is required, the annealing time is rather short and thus the diffusion and activation of the acceptors needs to happen quite fast. This however requires that most of the boron is already deposited at the boundary between bulk material and oxide. Hence, the maximum possible thickness of the oxide is further constrained. A thickness range from $20\,\mathrm{nm} < d^{Oxide} < 80\,\mathrm{nm}$ has been agreed on with CiS. This leaves the discussion on the overall dead-layer thickness with possible parameters of the implant thickness.

The standard parameters for ion implantation and a reduced annealing time by a factor of 4 for the activation of the acceptors would result in a $d \approx 680\,\mathrm{nm}$ dead-layer due to the implant. Energy loss calculations done with ATTIMA [72] favour a overall entrance window thickness of 200 nm: The energy loss of a proton with 0.5 MeV kinetic energy in an entrance window of 1.5 µm thickness (which is a standard value) amounts to: $E_{loss}^{1.5\,\mu\mathrm{m}}(\mathrm{p}^{0.5\,\mathrm{MeV}}_{\mathrm{SiO_2+Al}}) = 111 \pm 3.7\,\mathrm{keV}$. Contrarily, the reduced thickness of 200 nm results in a reduced energy loss of $E_{loss}^{1.5\,\mu\mathrm{m}}(\mathrm{p}^{0.5\,\mathrm{MeV}}_{\mathrm{SiO_2+Al}}) = 14 \pm 1.3\,\mathrm{keV}$. Achieving implantation profiles with less than 200 nm effective thickness[4] is highly non-standard as well. New methods for the implantation with extremely low energy and very short thermal annealing times were investigated: Plasma-immersion ion implantation with accelerating potentials reaching from 2 kV to 10 kV and boron concentrations from $5E15\,\mathrm{atoms/cm^2}$ to $1E16\,\mathrm{atoms/cm^2}$, as well as rapid thermal annealing variants with peak temperatures up to 1100 °C and plateau times of as short as 5 s have been investigated. The importance of the oxide thickness, as discussed already earlier, was also tested in several different wafer production runs. The exact final parameter still need to be defined. Similar to the effective thickness it was shown in the reactor experiments (see V.2), that a reliably working *p*-*n*-junction can be achieved from a peak-concentration $\gtrapprox 1E19\,\mathrm{atoms/cm^3}$.

Further complication arises from the requirement of extreme homogeneity of the dead-layer. Measurements with an off-the-shelf available DSSSD[5], but also with PIN-Diodes used for the implant-thickness determination as described in the following chapter (for details on the implant thickness, please refer to V.2) have nicely shown the importance of an entrance window with homogeneous thickness: As shown in figure IV.6, the appearance of additional structures in the triple-alpha spectrum, measured with the SKIROC2A ASIC, is related to the thickness fluctuation of the dead-layer of those detectors.

[4] The effective thickness is the thickness of the implantation profile, which contributes to the dead-layer (inactive region) of the detector. From experiments at the FRMII (see section V.2) it was concluded that boron acceptor concentrations $\gtrapprox 1E16\,\mathrm{atoms/cm^3}$ result in inactive material.

[5] W1(DS)-100, Type 9G/2M Silicon detector from Micron Semiconductor with a dead-layer (implant thickness) on the junction side of only 0.1 µm.

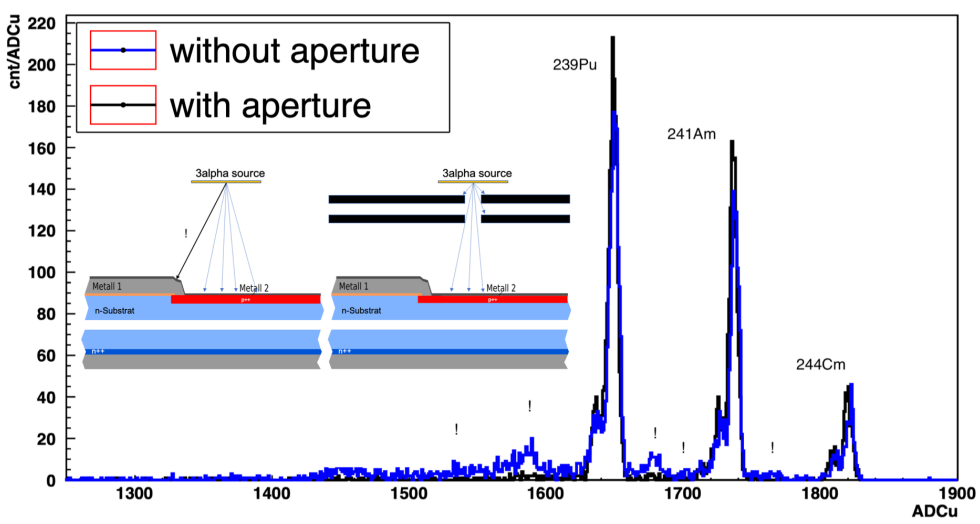

(a) Overlay of 3α-spectra measured with and without an aperture. The influence of thickness inhomogeneities in the spectrum are denoted.

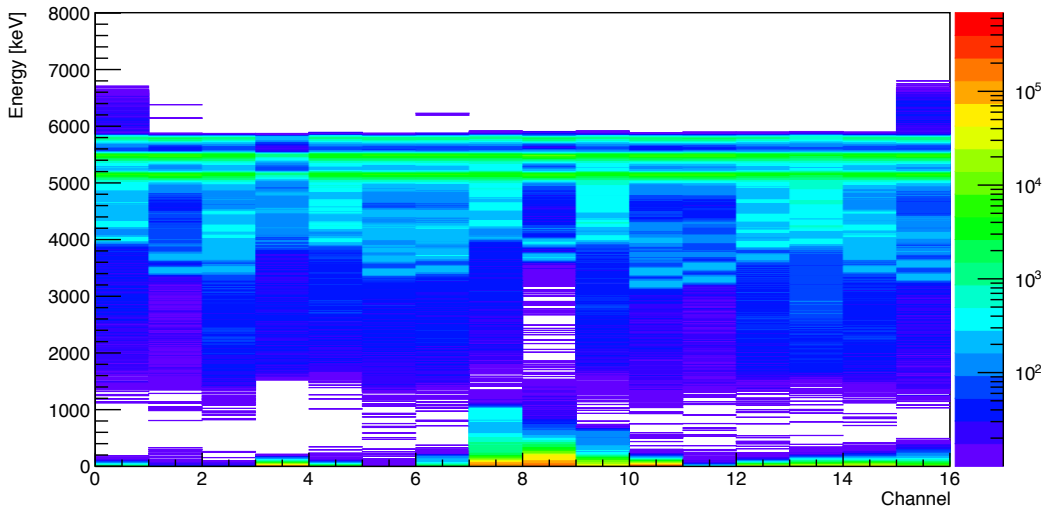

(b) Calibrated energy spectrum measured with a DSSSD, whose metallisation on the p-side is highly inhomogeneous. The enhanced low-energy statistics around channel 8 is due to noise issues in a flat-ribbon cable. Note the presence of additional peak-like structures at energies lower than the 3α source produces.

Figure IV.6: Influence of inhomogeneities in the dead-layer on the measured energy spectra. The appearance of additional peak-like structures so-called satellite peaks in any energy spectra, especially in experiments with low counting-statistics, is very undesirable. In figures IV.6a and, the 3α-spectra of the PIN-diodes used in the experiments of section V.2 are shown. Figure IV.6b shows the response of all 16 strips from the DSSSD used in the experiments of section V.3. All measurements have been performed with the same SKIROC-2A ASIC and electronics readout-chain.

In the case of figureIV.6a, the thick metallisation at the edge of the circular diodes produces the additional structures, as indicated in the inlets of the spectra. In figure IV.6b, it is most likely the metallisation as well: There is no information available on the exact implantation-profile and, as this is a DC-coupled detector there is no contribution from decoupling oxides. However, charge collection by the metallisation is done in a grid-like structure (and not an areal metallisation), which then needs to be quite thick ($\approx 0.5\,\mu m$) in order to guarantee a low relative resistance. It is most likely this grid, which is the reason for the peak-like, additional structures as the integral ratios of the proper 3α-peaks and the additional peaks roughly yield the value of a few percent. This fits to the $\approx$ 3% grid coverage Micron Semiconductor states. Avoiding such effects is an important part in the detector design of the new, highly segmented, thin HI-TREX sensors. Introducing an additional processing step, which enables the deposition of a so-called 'compensation-oxide' needs an additional mask and parameter adjustments, but allows to compensate for the thickness fluctuations due to the implant, decoupling oxide and metallisation structures. The thickness of the compensation-oxide can be tailored to the final overall dead-layer thickness and thus guarantees maximum homogeneity.

Figure IV.7b details the width of the metal strip, which has been chosen to overlap slightly the implant strip in order to reduce high field-gradients in the vicinity of the boundary implant/oxide/bulk material and thus prevents micro-discharges in dry atmosphere [41].

All the efforts, which have been made for the *p*-side concerning the shallow and homogenous entrance window are not required for the *n*-side (ohmic contact) of the detectors as the energy straggling in the bulk material is dominating. This reduces the complexity of the backside-processing in the etched cavities a lot. Hence standard parameters have been chosen, which result in an overall dead-layer thickness on the *n*-side of $\approx 1.0\,\mu m \ldots 1.5\,\mu m$. The isolation of adjacent n^+-contact strips is done by the *p*-stop/*p*-spray technique. Due to fixed and trapped charges in the bulk-oxide interface an inversion layer forms on this boundary, which would shorten the contacts. Using a moderated p-spray technique through an additional mask, introduces a p^+-region which breaks the electron accumulation layer and thus guarantees isolated n-side strips.

Further details on the n-side layout, as well as the dimensions and layout of the biasing structure, bond-pads, fiducials, etc. can be found in the appendix A.

IV.1.2 Constraints for the unsegmented silicon E_{Rest} detectors

Extensive GEANT4 simulations have been performed concerning the punch-through and particle identification problematics. The aforementioned show-case reaction has been used. As touched in III.4 a decision was made to use two 700 µm thick membranes. Although the GEANT4 simulations would favour a setup of one 500 µm

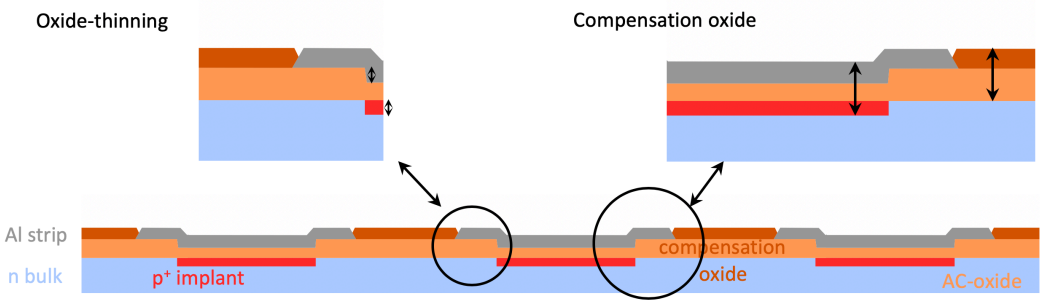

(a) Schematic cross section of the p-side dead-layer structure. Special attention is drawn on the compensation oxide, guaranteeing maximum homogeneity.

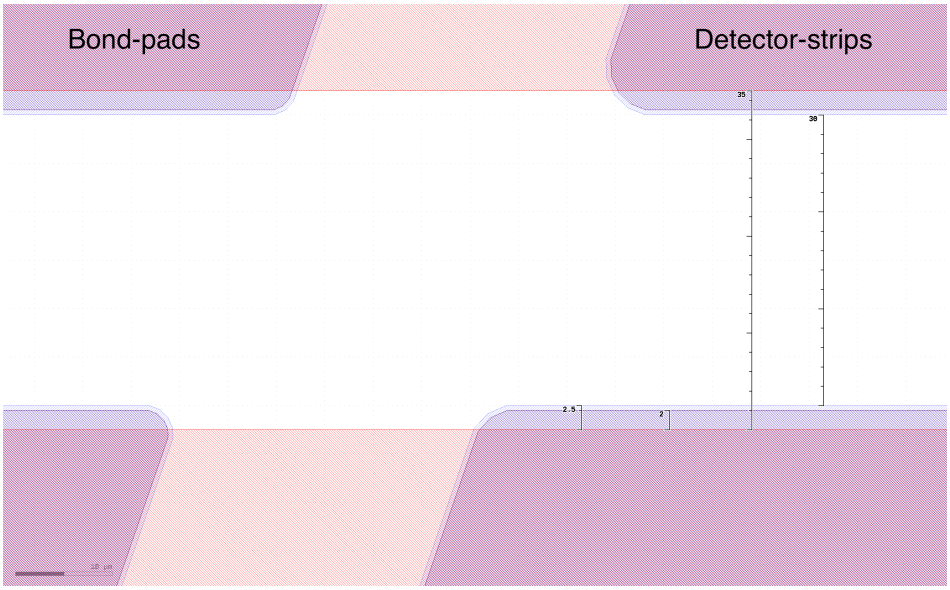

(b) Top-view on the final detector design. Reddish areas show the p-implant. Blue shaded areas represent the metallisation and purple areas the mask for the compensation oxide. Distances are given in µm.

Figure IV.7: Compensation oxide design.

thick and one 1000 µm thick detector mounted in close succession in terms of PID performance, the difference in elastically scattered deuteron-suppression - being in the punch-through energy regime - of only 1.4% compared to the setup using two identical thicknesses of 700 µm was outweighed by the economical benefits having only one wafer thickness, which is by-the-way highly non-standard for industrial applications as well. The detectors will be unsegmented and no special attention needs to be paid to extremely thin entrance window thicknesses or similar efforts

done for the DSSSDs. As the full depletion voltage of these detectors should be $< 200\,\mathrm{V}$, bulk-material with quite high resistivity needs to be used. The reason for constraining the upper value of the depletion voltage lies in the generation and handling of such voltages, the corresponding PCB-design and cabling concept, as well as the space requirement inside the MINIBALL target chamber.

The mounting of the E_{Rest}-detectors will be done 'back-to-back'. This enables the closest possible arrangement on a common PCB, which is required due to the space-restrictions of the target chamber.

IV.2 Electronics development

Compact readout systems for highly segmented silicon detectors are commonly based on advanced application specific integrated circuit (ASIC) technology which allows to minimise electronics noise, space requirements and power consumption. Due to the large overhead in the development and implementation, this technology is mostly used in large scale experiments of particle physics or specialised application of the consumer market.

In typical nuclear physics experiments the requirements are usually significantly different. Different ion species are passing the detectors at a wide range of energy loss. Low energy particles are stopped within the first few micrometer of the sensors and in most cases spectroscopic resolution on the signal amplitudes is required; features which are not covered by default for the ICs developed for tracking of minimum ionising particles (MIPs) in high energy physics.

A new generation of ASICs is currently developed for the versatile application in large scale electromagnetic and hadronic calorimeters (EMCs, HCALs). Going from standard PMT readout to more compact systems like APDs or SiPMs and covering the large dynamic range of electromagnetic showers, these devices much better fit the demands of experiments at HIE-ISOLDE. We have investigated the ROC family developed by the École Polytéchnique in Paris for EMCs and HCALs in next generation linear collider experiments. Their chips are available in different flavours with a set of basic features nicely fitting several requirements in medium-rate heavy ion reaction experiments.

Especially the SKIROC2-CMS and the SKIROC2A with 64 independent channels are under consideration

The basic data-taking processes are schematically indicated in figure IV.8. The charge generated by the silicon detectors is preamplified by the ASICs, filtered, shaped and memorised in an analog way in embedded capacitors. In a parallel ASIC branch a trigger is generated, which can be used to initiate the digitisation of the stored analog values and the successive readout of the data. Data aggregation

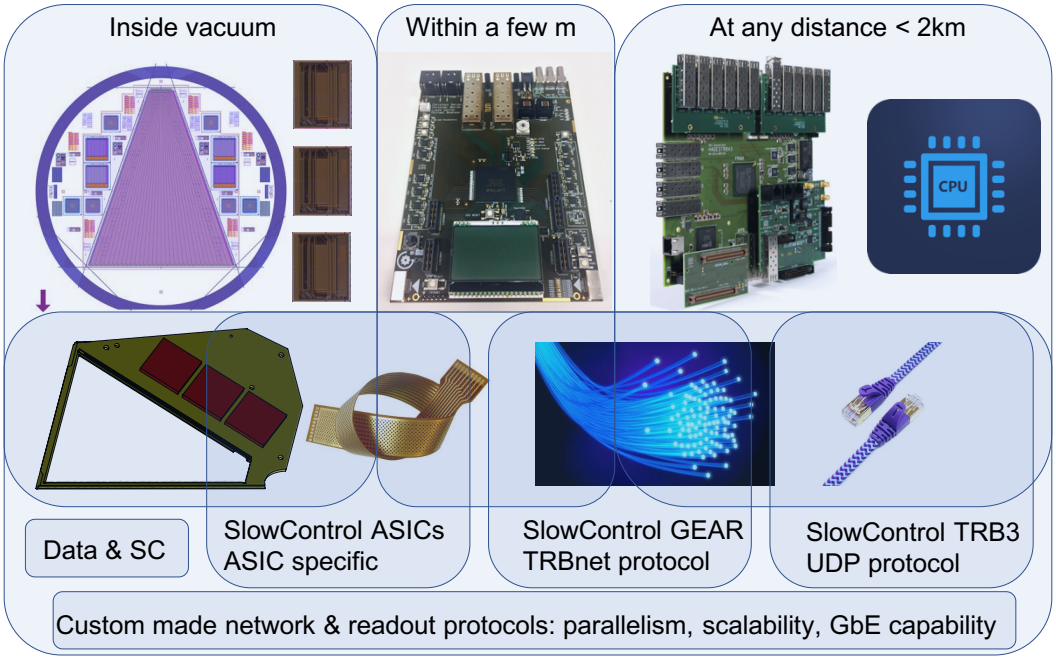

Figure IV.8: Overview on the compontens, which are involved during data taking: The very-front-end Hybrid-PCB hosting the detectors and ASICs, the front-end board GEAR, providing the control of the ASICs and collecting their data, and the back-end platform TRB3 for networking and data storage. Rough distances to the detector are given, as well as the interconnection types between the various data processing modules and the type of data-format.

and ASIC control is done by the generic readout board GEAR and the back-end platform TRB3 is used for networking and data storage.

In the successive sections, the electronics developments done within this work are presented. Starting with the requirements for the very-front-end electronics and outlining the common features of both ASICs, the SKIROC2A and the SKIROC2-CMS, introduces the basics for understanding each ASICs unique working principle. A selective overview on the front-end electronics GEAR highlights some features of the data readout, before the back-end integration is presented.

IV.2.1 Very-Front-End electronics: ASICs

General constraints for the very-front-end electronics (VFE) were already discussed in III.4.3. With the Silicon sensors being newly developed, it is mainly the detector capacitance per strip influencing the overall system performance in terms of ENC

(see IV.1 in section IV.1.1 for more details). The basic requirements for the VFE-ASICs are listed below:

- Sufficient amount of readout-channels per (small) footprint
- Possibility to readout both polarities
- Sufficient charge input range for transfer experiments
- Charge, timing and trigger output
- Low ENC and self-trigger capability
- Input capacity and shaping times matched to typ. silicon strip capacities
- Low trigger threshold and individual threshold control
- Rate capability
- Power consumption
- Easy controllability via SlowControl
- Possible digitisation directly on-chip

Of the more than 20 ASICs that were shortlisted, only the AGET-ASIC (developed by CEA Saclay) [7] and the SKIROC2-ASIC family met the above-listed requirements. An incomplete list with some specifications of the shortlisted ASICs can be found in the appendix in C. Finally it was decided to use the SKIROC2-ASICs, as for a properly working AGET readout, their whole (proprietary) system needs to be purchased, which then would mean a reduction in flexibility. The drawback when using the ASICS developed by OMEGA Microelectronics is the need to use two slightly different ASIC versions: The SKIROC2A (originally developed for the future ILC experiment) [22] and the SKIROC2-CMS (prototype ASIC for the CMS-tracker upgrade) [16], as the SKIROC2A ASIC is only capable of positive polarity input, whereas the SKIROC2-CMS ASIC can handle both polarities but with the drawback of missing rate-capability and corresponding trigger generation, as well as the way of measuring high input-charges by a time-over-threshold (TOT) method. Further basic differences are listed in table IV.1.

In short, the basic working principle of both ASICs is as follows: 64 parallel channels preamplify, filter and shape the charge signal generated by the detector. An implemented switched capacitor array (SCA) memorises the analog information of charge and/or time. Both SKIROC chips feature a multiplexed, analog output, as well as a fully digitised output, buffered in the embedded 4 kbytes RAM. The energy/charge measurement is 14 bits wide thanks to a low gain (Gain = 1) and

Table IV.1: Basic differences of the front-end ASICs SKIROC2A and SKIROC2-CMS. TOA denotes time-of-arrival and is used to do the time-stamping of individual events. SCA is an abbreviation for switched capacitor array and is used to store voltage levels in an analog way.

measurement	input range/polarity	shaping τ^{slow}	shaping τ^{fast}
	SKIROC-2A		
Energy (ENC $<$ 6 keV)	$+0.4\,\mathrm{fC} \ldots +10\,\mathrm{pC}$	180 ns	30 ns . . . 120 ns
Time ($\sigma^{TDC} < 100$ ps)	16 common gains		4 settings
15 SCA static buffer		gain1 and 10	gain 10
	SKIROC2-CMS		
Energy (ENC $<$ 8 keV)	$\pm 0.4\,\mathrm{fC} \ldots \pm 10\,\mathrm{pC}$	10 ns . . . 150 ns	1.25 ns . . . 9 ns
TOA & TOT ($\sigma < 25$ ps)	48 common gains	16 settings	8 settings
13 SCA roll buffer		gain 1 and 10	gain 6

a high gain (Gain = 10) shaper and a 12 bit Wilkinson ADC. The threshold of the trigger is adjustable on all the 64 channels thanks to a common 10 bit DAC and can be optimised channel by channel by 64 individual 4 bit DACs. Only a +3V3-supply line is needed as all the reference signals are made from an internal bandgap voltage reference. The integrated power management optimised for bunched beams allows to shut down individual stages (even analog ones (!)) during acquisition, conversion or digitisation of events and thus enables the use of both chips in vacuum without cooling: When power pulsed, the SKIROC2A-chip has a power consumption of only 25 µW per channel (0.5 % duty cycle). But attention has to be paid, when using this nice feature, as the chip needs to recover its correct operating voltage values fast enough after being switched on again. Hence, external decoupling capacitors need to be chosen appropriately. At least 100 µs recovery time are required having no external decoupling at all. Additionally, in pulsed beam experiments, the digital buffer of the ASICs, together with the embedded analog memory, allows to cope with very high instantaneous rates, as dead-time basically is limited by the internal switching between two SCA-cells to 70 ns. Both ASICs have the same footprint and a similar data structure. This data-format uniformity is advantageous for the interface board GEAR (see next subsection IV.2.2). The readout system is based

on an asynchronous token-ring protocol and all critical data lines are doubled for redundancy.

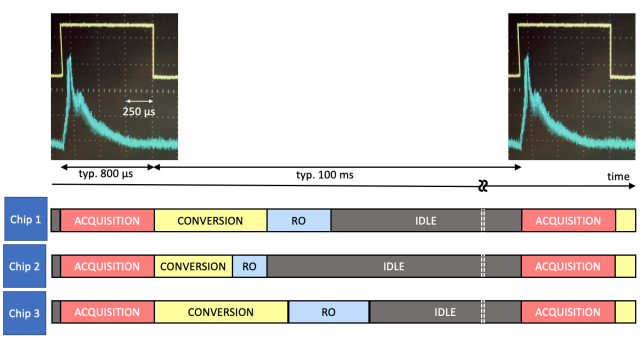

(a) Basic DAQ schematic for three ASICs. Typical time scales of the beam-structure and the release curve of the ^{134}Sn beam (as presented in III.4a) are shown. RO denotes read-out.

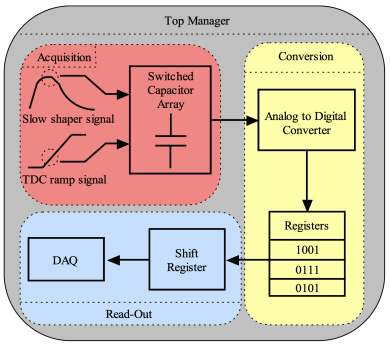

(b) General data flow in one ASIC to the GEAR-board, which controls the read-out. Adapted from [28].

Figure IV.9: Data acquisition (DAQ) schematic of the SKIROC-ASICs. The three basic parts of the DAQ consist of the acquisition of analog data, the conversion and digitisation and the read-out by the front-end electronics (GEAR).

Although up to 256 ASICs can be daisy-chained and thus the amount of readout-lines is reduced, in the setup for HI-TREX it was decided to not use this feature in order to guarantee maximum data-throughput having individual control and readout-lines for each ASIC.

A complex digital machine drives the whole system on chip: Several modes are available to ensure sequencing in the chip (see figure IV.9). During the acquisition mode, the digital control starts the analog core and drives the 15 depth analogue memories in terms of SCAs and the trigger to memorise the data when a signal occurs over the individually adjustable threshold. During the conversion mode initialised by the front-end board GEAR, the values stored in the analog memory are digitised using a multi-channel 12 bit Wilkinson ADC and finally shifted as Gray-decoded values into the internal 4 kbyte SRAM. It is the firmware (FW) of the GEAR board again, which initialises the read-out of the data and empties the ASICs memory. As the fill-level of the SCAs can be different from ASIC to ASIC, the conversion and read-out process can take different times as only the SCA-cells are read during conversion with a voltage level which is over the set threshold. The basic design decision for the SKIROC2 chips was to have a multi-purpose readout-chip which embeds as many useful features as possible. For instance, the preamplifier stages of individual channels can be deactivated, or an internal test capacity of 3 pF can be switched to each of their inputs for calibration purposes, not to mention

the control of various modes of operation, the activation and deactivation of their corresponding stages and the control of all the testing-outputs. Hence there is a several hundred bits long configuration for each ASIC which needs to be loaded via SlowControl properly. The implementation of this SlowControl-loading is done on basis of the TRB3-platform and the GEAR board.

In the following two paragraphs, the basic working principle of the two ASICs is presented and the main differences are further detailed.

IV.2.1.1 SKIROC-2A

The Silikon pin Kalorimeter Integrated ReadOut Chip (SKIROC) is a 64-channel front-end chip, designed in AMS 0.35 µm SiGe technology. Its analog part, shown in the schematic IV.10 has been designed to handle a dynamic range from 0.1 MIP (0.4 fC) to 2500 MIPs (10 pC).

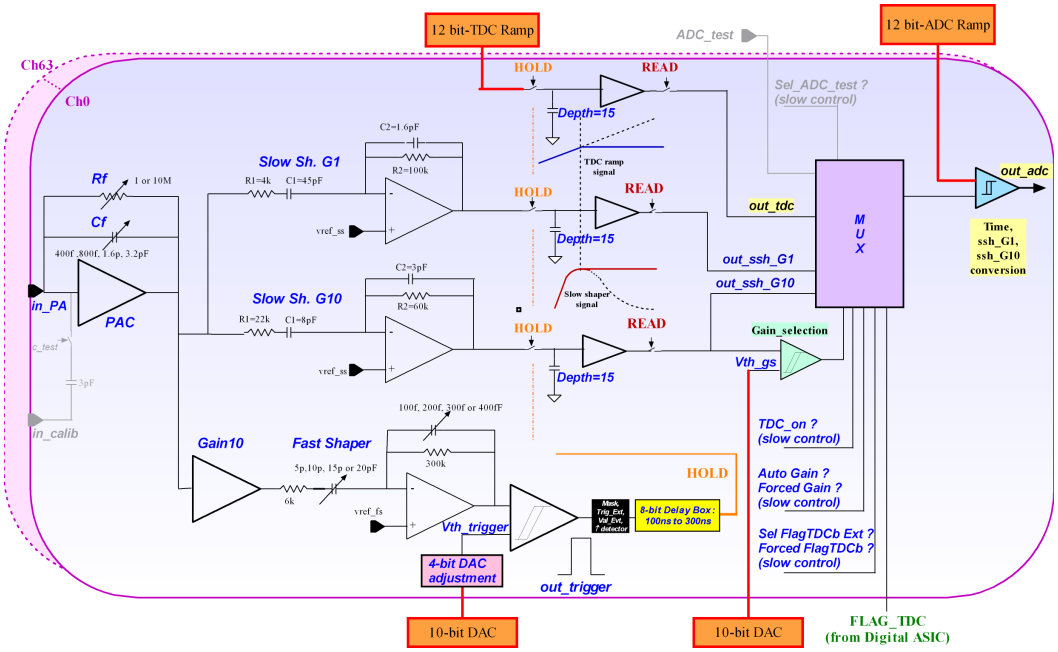

Figure IV.10: Simplified analog core of the SKIROC2A ASIC. The schematic was kindly made available by [21].

The chip has been optimised for an input detector capacitance of 20 pF (compare figure IV.1b). Each channel is made of an input charge preamplifier. A common gain can be set by changing the feedback capacitor C_f using SlowControl parameters. The gain thus can be varied within a factor of 15 as the inverse of C_f determines the gain of the charge integrating preamplifier. The role of the preamplifier is to convert

a current pulse, corresponding to a charge, into a voltage step. This preamplifier is the most critical part of the chip. I must be as low noise and low power as possible. It uses a typical cascode structure: a transconductance amplifier followed by a current buffer and an output voltage follower. This structure maximises the open loop gain and thus in conjunction with the feedback network helps to tailor the amplification to the overall dynamic range design of the ASIC. A compensation capacitance C_c has been added to avoid oscillations of the amplifier at certain gain settings. There are two preamplifier outputs: one is sent to the slow shapers, representing the energy-branch of the ASIC and the other one to the fast shaper, representing the timing-branch correspondingly.

The goal of the shapers is to filter certain noise contributions. All shapers in the SKIROC2A use a standard $C_1R_1R_2C_2$ inverting shaper. To ensure a good shaping behaviour, C_1R_1 must be equal C_2R_2, as otherwise the shaper will filter less noise, or its gain bandwidth product will be degraded. In such a $CRRC$ configuration, the peaking time of the shaper is equal to the constant time $\tau = C_1R_1 = R_2C_2 = 180\,\text{ns}$ in the case of the slow shaper branch. The fast branch has tuneable shaping time parameters and is followed by a low-offset discriminator to trigger-down to 0.1 MIP equivalent input charge. The threshold adjustment by the aforementioned DACs is done at this point. The discriminator output is sent to a delay-cell providing the wired-OR of all 64 channels as $HOLD$ signal for the slow shaping branches as well as an undelayed signal as a trigger-output to a pin of the ASIC. The $HOLD$ signal is used to store the peak-values (if the tuneable delay is properly set) of both shaped signals, as well as the TDC ramp amplitude corresponding to the time of the event in the embedded capacitor array (15 capacitors per channel; each capacitor has a capacity of 500 fF) simply by opening a corresponding switch. Additional coarse time stamping is performed by a 12 bit Gray-counter, which simply is incremented each clock cycle of the $Slow\_Clock$ and memorised when a (delayed) OR trigger signal occurs, which corresponds to a hit-over-threshold in any of the 64 channels. This time-stamp is referred to as Bunch Crossing ID (BCID) in the data-structure of the SKIROC-2A shown in the appendix D.

This whole process happens, when the DAQ-mode 'acquisition' is active. The subsequent 'conversion' phase then selects the stored analog values to be converted depending on a SlowControl setting: Either both slow shaper outputs are selected, or one charge and one timing information from the TDC-ramp can be chosen to be digitised. This is done by an analog multiplexer and a Wilkinson ADC, whose resolution can be selected depending on the required rate-capability to be 12 bit or 10 bit. The ADC can convert 64 charge or time values in 100/25 µs (12/10 bit). When the SCA is completely full, 2x15 runs are needed to convert the complete buffered information. The maximum conversion time hence is 3.0 ms/0.75 ms. When a conversion is over the data are stored on-chip in the embedded RAM and a new one can start. As soon as the 'conversion' process is finished, the chip signals the

front-end electronics, that data are ready to be read out. As analog values can be stored, the 'acquisition' phase can start immediately over again and thus can run in parallel to the 'readout' phase.

IV.2.1.2 SKIROC-CMS

SKIROC2-CMS is a chip derived from SKIROC2A, designed as a protoype-ASIC for the high granularity silicon tungsten calorimeter (HGCAL) chosen by the CMS collaboration to replace its endcaps fo the phase 2 upgrade. SKIROC2-CMS is a pin-pin compatible variation of the SKIROC2A chip tailored to CMS needs. It keeps the same basic architecture with some modifications and accelerations mainly to the analog core, shown in figure IV.11: The preamplification stage is optimised for 50 pF input capacitance and now features dual-polarity inputs with feedback capacitors and resistors available for both polarities. The peaking time of the slow shaping branches can now be tuned from 5 ns to 80 ns using SlowControl parameters. The fast shaping branch was accelerated as well: 0.625 ns $< \tau <$ 5 ns. The analog memory was modified to run continuously at 40 MHz and provide waveform sampling, which can be used to study pulse-shape variations. The depth of this 'rolling' SCA was reduced to 13, although only 11 SCAs store meaningful analog values due to the way the 'rolling' SCA was implemented.

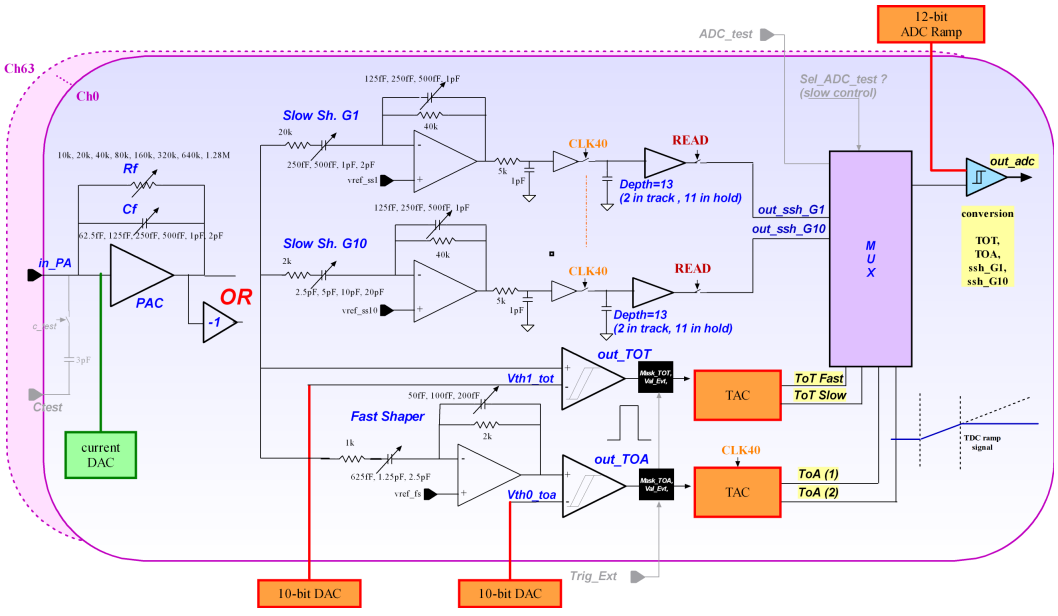

Figure IV.11: Simplified analog core of the SKIROC2-CMS ASIC. The schematic was kindly made available by [21].

Next to the nominal rolling mode of the SCA, there is the possibility for a custom control of the SCA, managed by an external trigger and two LVDS-lines denoted as *RxRollClock* together with some SlowControl setting. It is the falling edge of this *RxRollClock* which performs the hold of the signal in the SCA. It is this special mode which will be used for the measurements with HI-TREX. In the timing branch, two discriminators provide time-of-arrival (TOA) and time-over-threshold (TOT) informations, thanks to a TDC based on a time-to-amplitude converter (TAC) with a step of 25 ps [92]. The TOT feature is especially helpful for signals saturating the preamplifier. The TOT discriminator is directly connected to the preamplifier output. A fast ramp (for non-linearities study; 50 ns ramp) and a slow ramp (for the entire input charge range up to 10 pC; 500 ns ramp) are implemented. TOT data are memorised into the feedback capacitance of the integrator; the rising edge of the discriminated signal start it and the falling edge correspondingly stop the slow and fast ramps. An individual 10 bit DAC is implemented for this type of charge measurement. Drawback of this method is the lack of up to 11 analog storage possibilities as compared to the charge measurement via the 13-depth SCA. The time measurement via the TOA is quite simple: after the fast-shaping branch, the signal is sent through a fast discriminator providing the start signal of the TAC ramp (35 ns long). Subsequently, the falling and also the rising edge of the internal 40 MHz clock sample the ramp-amplitude and memorise the value for further analysis. As can be seen in the data-structure shown in appendix D.2, the relevant data mapped in the memory by the TOA branch is the digitised TAC ramp (both edges), the hit-bit in each channel which has seen a signal over the TOA-threshold and the global timestamp value, which simply is a global counter running at 40 MHz, denoting the time of the TOA hit since the acquisition was started. When using the SKIROC2-CMS in the custom roll-mode, the hit-information is meaning-less, as well as the global timestamp and the TOA/TOT values only represent the first external trigger and not the whole 11 possible events are mapped to the embedded memory. Details on how the timestamping is done in the HI-TREX setup will be detailed later-on in the firmware-section IV.2.2.3.

There are a few more differences, e.g. like replacing the open-collector data output line running at nominal 5 MHz in the SKIROC2A with a 40 MHz LVDS line. However for further details and differences (like on the signalling standard of the input and output ports (3.3 V CMOS is extensively used)) the corresponding data sheets should be consulted.

IV.2.2 Front-End electronics: GEAR

A newly developed data acquisition (DAQ) system is described which will be used for the HI-TREX setup: GEAR. The design of this GEneric Asic Readout board is sufficiently generic and scalable such that it should have numerous applications

either for the MINIBALL silicon detectors, the neutron depth profiling instrument at the FRMII or elsewhere within nuclear physics experiments in general. The DAQ system was implemented using field-programmable gate arrays (FPGAs) and built with off-the-shelf components. The back-end integration provides the networking hardware and is based on the successfully used TRB3 platform with programmable FPGAs. The software for the DAQ system is mostly written from scratch and is steadily evolving. The design philosophy, the basic components of the GEAR and their aims are presented in the following.

IV.2.2.1 Design concept of the GEAR and basic tasks of the central FPGA

The design of the GEAR was guided by three major decisions:

- Guaranteeing full flexibility for ASIC control
- Providing the appropriate infrastructure for interfacing the back-end
- Hosting of the power supply for the ASICs
- Allocating enough connectivity for generic purposes

To accomplish this, FPGAs were used as they can be programmed via the Very High Speed Integrated Circuit Hardware Description Language (VHSIC Hardware Description Language; VHDL) to basically represent nearly every digital logic as long as the input/output, clock and voltage requirements of the FPGA are met and as long as the amount of functional, logical elements is enough. These basic logical elements are usually represented as a lookup-table (LUT) with one flipflop. For the central FPGA on the GEAR board we have chosen the ECP5UM-85F-8BG756C from Lattice Semiconductor, which offers 84000 LUTs and 365 input/output pins which offer far enough space for required logic. Furthermore there is more than 8.1 Mbit of dedicated memory available, as well as 156 18 bit multipliers, 4 PLLs (phased-locked loops) for clock generation and 4 high-speed SerDes (Serializer-Deserializer) ports with up to 3.2 Gb/s throughput each, all available in quite a small package (756 caBGA; $27x27$ mm) with comparably low power consumption.

The FPGA is responsible for controlling the ASICs, setting their proper Slow-Control values and gathering their data for further processing in order to meet the back-end data-format requirements. Details on how this is done can be found in the following firmware-section. Furthermore, it provides the necessary clocks in a synchronous way to the ASICs, timestamps all events with higher clock-speed than the ASIC is doing, ensures that the SKIROC2-CMS can be used properly in the custom roll-mode, triggered by the SKIROC2As and offers due to the modularly written VHDL-code that the system can be scaled easily. It was decided to keep maximum control of the ASICs and hence provide for every testing or configuration

pin of the ASIC a dedicated FPGA-port. This results in the possibility to read-out 3 ASICs per GEAR board, which is by the way a kind-of native number, as there are 3 ASICs located on the Hybrid-PCB. Hence for each detector-PCB, one GEAR board is required.

Another decision was to use only 2 out of the 4 possible SerDes connections, due to space constraints and the need of only using one for all the data-transport and communication with the TRB3. Furthermore, the voltage supply of the individual banks in the FPGA was defined according to the need and layout of the ASIC lines to 2.5 V for LVDS signalling and 3.3 V for LVCMOS signalling for the single-ended lines respectively. There are a few lines, which can be used in a so-called emulated LVDS ('LVDSe') mode, by simply changing the values of a resistor network located close to these ports and thus can provide both, 2.5 V LVDSe signalling standard and single-ended 3.3 V LVCMOS. Nonetheless, as the FPGA firmware can be changed quite easily and as the bank-voltages can be adapted by choosing an appropriate value for a resistor soldered near the voltage regulators, there is still the whole flexibility of the GEAR board prominent.

IV.2.2.2 Further basic PCB-components

Next to the central FPGA, a second FPGA although smaller in terms of logic density (4320 LUTs) and space (68 IOs; $7x7$ mm) is equipped on the GEAR board: the MachXO2-4000HC-6QN84I. This FPGA acts in a watch-dog function for the central FPGA, enabling a remote restart, even by cutting the power of the central FPGA, as the MachXO2 is always powered. It initiates the power-up sequencing implemented on the board to meet all the required timings for the ECP5UM and auxiliary voltage regulators: The voltage regulators, which are all low-dropout regulators (LDOs) and which are always powered are the MachXO2 supply and the STM32 (microcontroller) supply, as well as an auxiliary supply for some possible add-on. Further bias-generating devices always powered are a 5.5 V boost charge pump, required to guarantee the lowest possible drop-out of the LDOs, and to provide the input voltage for a high-precision voltage reference generator, needed for the internal DACs of the STM32. The MachXO2 enables the LDOs for the SerDes-core of the ECP5UM and the bank voltages. When their power is applied successfully, the actual ECP5UM-core is powered up together with some more auxiliary FPGA-components. Finally, the ECP5UM can control the four different LDOs for the SKIROC2-ASICs. It was decided to have a own voltage supply and corresponding lines (also on the Hybrid-PCB; detailed in section IV.3) for each of the different bias-requiring parts of the ASIC: One for all the preamplifiers, one for the analogue core of the ASICs, one for the complex digital machine implemented and one for the memory supply. This guarantees the best performance of the ASICs in terms of ENC and cross-talk.

Furthermore, the MachXO2 provides generic connections to the microprocessor,

the central FPGA and some spare lines to the add-on connectors. It furthermore connects to the two photocouplers with 50 MHz baud-rate and $\approx$ 3.8 kV isolation voltage. Hence, e.g. synchronisation with systems at arbitrary potentials can be done via this couplers.

The already mentioned microprocessor (STM32F767ZI) is mounted underneath an embedded LCD display and can be used for data display and debugging. It features 12 bit DACs, which can be used as a on-board pulse-form generator and thus enable an internal calibration of the ASICs with arbitrary (programmable) pulse-shapes. SPI-busses connect directly to the ECP5UM and to a 1 Mbit F-RAM, serving as a non-volatile memory for data-transfer between the microprocessor and the central FPGA. Quadrupel bus buffer gates ensure that no simultaneous access to the F-RAM from the ECP5UM and the STM32 is possible.

The connectivity of the GEAR board is another important feature. For HI-TREX it is advantageous due to mounting issues to have all necessary connectors to the back-end and power supply located on only one side of the PCB: Two RJ45 connectors for trigger, clock and some spare options, one SFP-glass fibre connector establishing the data-link from the GEAR-endpoint the the TRB3-backend and one spare SFP connector, the power supply connector delivering 1.5 V and 3.6 V as well as the three Lemo-connectors for the photocouplers. The connection to the ASICs, as well as to possible add-on boards, which can be mounted on the top-side connectors, is done by board-to-board mezzanine type connectors providing enough density, low resistance for the ASIC-power lines and enough rate-capability per pin. 240 spare pins are available on the top-side connectors for mounting of any auxiliary add-on board. Further connectors allow for fast inter-GEAR-board communication via coaxial cables, in case any setup requires interconnections without involving the back-end. E.g. a Master-Slave communication between the microprocessors via SPI can be implemented quite straightforwardly.

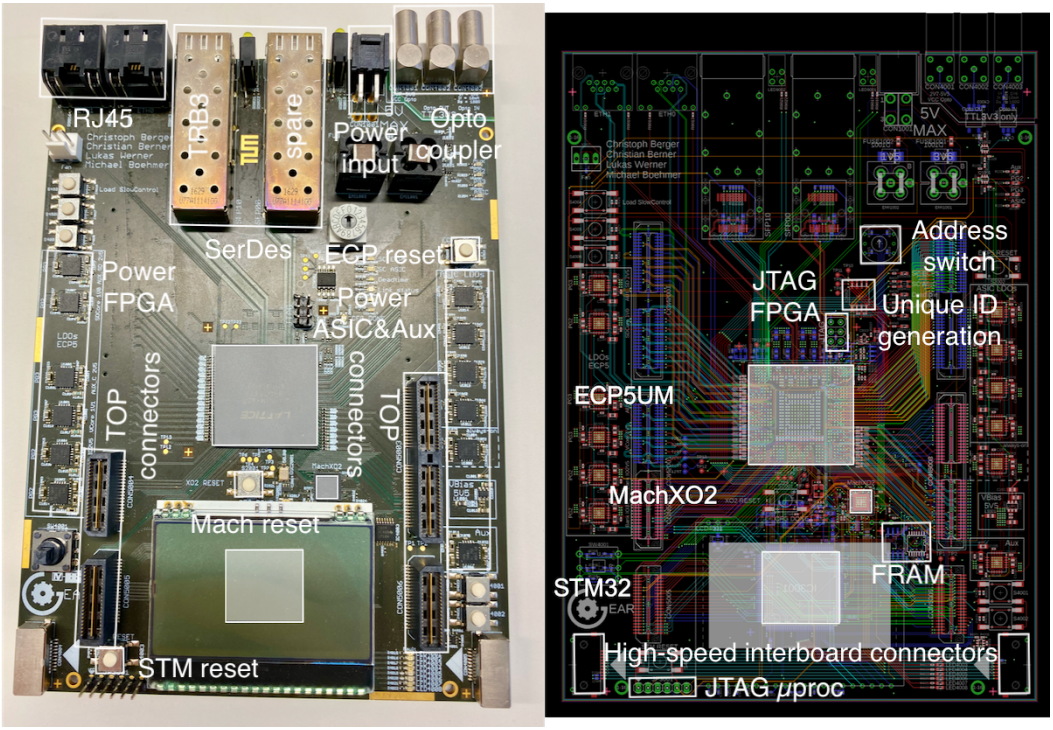

Figure IV.12: Photograph (left) and schematic (right) of the GEAR board. The main ICs are indicated with shaded areas. Further basic PCB-components are labeled. For details, please refer to the text. Note the compact dimensions (12.4 cm$x$17.0 cm) of the 8 layer PCB.

IV.2.2.3 Basic FW features

The basic data handling process of the firmware (FW) is shown schematically in figure IV.13. The FW implements all the basic tasks as already specified: ASIC integration, data processing and back-end interfacing. Three independent ASIC-branches have been implemented, which can be read out stand-alone. The difference between the SKIROC2-CMS branch and the SKIROC2A branch is mainly in the Transmission and Acquisiton/Conversion module. There are of course many more modules implemented taking care of e.g. the wrapping of the SlowControl data for the ASICs, which is sent via the well-defined TRBsc SlowControl registers and needs to be sorted into correct order for providing the bitstream, which the ASICs are expecting via SPI. Another modules take care of proper reset and clock handling, provide communication with auxiliary components such as the microprocessor or the MachXO2, another ones control the modes of operation of the data-transmission of the ASICs which can be changed to parallel or sequential, or simply take care

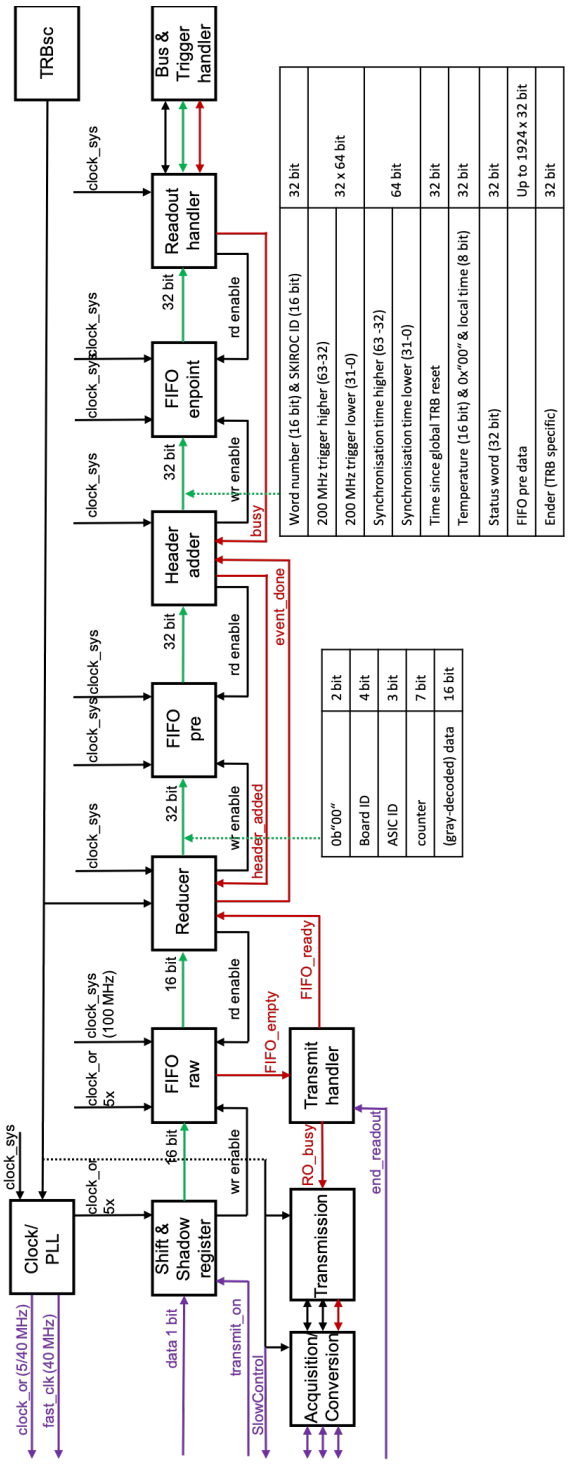

Figure IV.13: Basic firmware concept of the data handling. Lines connecting to the ASICs are shown in blue. Green connections indicate the data, whereas red signals guarantee sequential data processing as they perform some kind of hand-shaking. The data structure as it is modified by the various modules is shown in the two tables. Note the oversampling of the data-line from the ASIC to guarantee via edge-detection clock-synchronous further processing. The modules TRBsc and Bus&Trigger handler are TRB-specific [89] and adapted from the DIRICH-FW core [63] to our needs. The state machines controlling the different ASIC modes are only indicated schematically.

of status communication and the LEDs equipped on the PCB. Hand-shaking has been implemented to guarantee no event-mixing in the FPGA. The system clock provided to most of the entities is 100 MHz. The FW has been designed to be as modular as the GEAR board itself as all the implemented entities can be scaled quite straightforwardly to a higher number of ASIC branches controlled by one FPGA.

Details on the specific state-machines of each module also for the specific ASIC-control will not be given here, instead attention is given to some special modes of operation, uniquely developed. First of all, the SKIROC2-ASICs require two different clocks at 5 MHz and 40 MHz, which internally generate the required timing for the different ASIC stages. Whereas the analog stages require to have the above mentioned values and the ratio of 8 between the fast and the slow clock, there is no special need for the digitised values to be read from the RAM and transmitted at clock speeds of the slow clock frequency of 5 MHz for the SKIROC2A, which is the nominal value, as long as the fast clock speed is not exceeded and the drivers for the open-collector data line still deliver reasonable - and for the FPGA detectable - signal shapes. Various clock speeds have been tested and the signal shape of the transmitted data has been analysed, which is still good-enough for a slow clock speed of 40 MHz during transmission. Thus a mode of operation has been implemented, which switches between the 5 MHz and the 40 MHz clock speed, when a SKIROC2A ASIC has stored an event in its RAM and requests a readout. It can be decided via SlowControl whether the nominal readout at constantly 5 MHz, or this special mode is operational. As for the SKIROC2-CMS, the data-lines have been designed as LVDS signals at 40 MHz, there is no need to increase its readout speed.

Further special mode of operating the ASICs is due to the design of the 'rolling' SCAs in the SKIROC2-CMS as explained in the paragraph IV.2.1.2. The two basic modes of operation - the nominal 'trace'-mode and the special 'singles'-mode - can be selected via SlowControl. Furthermore it can be decided if the CMS-chip is triggered externally by e.g. the SKIROC2As, or is free running and triggers internally. The trigger handling schematic can be seen in figure IV.14. An adjustable trigger delay with variable width is implemented, which can be set via SlowControl. In principle, one could implement a kind-of lookup-table, which links the delay needed to the peaking-time of the shaped signal depending on the expected energies and thus ensures best resolution. For HI-TREX however, the resolution of the SKIROC2-CMS is not really crucial, as the energy measurement is done via the SKIROC2As, which nonetheless do have a slightly better ENC.

Another feature, which was implemented as a redundancy was the timestamping of the triggers, which arrive at the GEAR board. The sampling frequency was chosen with 200 MHz to be much faster than the BCIDs, which are done in the SKIROC2As with only 200 ns clock period. The delays introduced by the FPGA-logic (see picture IV.14) is constant and thus of no importance.

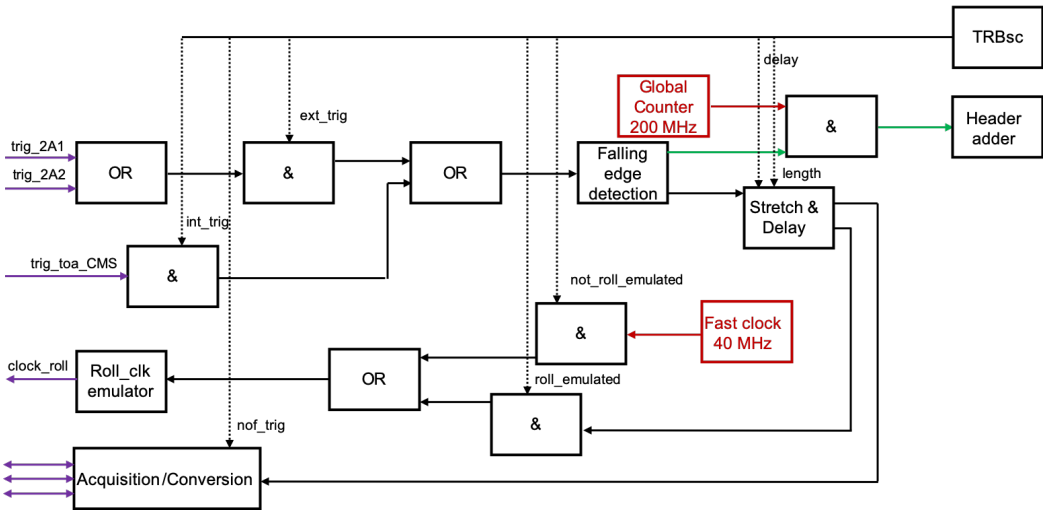

Figure IV.14: Trigger handling schematic for the SKIROC2-CMS. Blue signals depict again connections to and from the ASICs. Red labeled parts are clocks and the green arrows indicate the branch used for timestamping. Note that this timestamp is not delayed, or stretched as is the trigger for emulating the 'rolling' clock. Various SlowControl commands are available to properly configure the desired mode of operation.

IV.2.3 Back-End electronics: TRB3

The TRB3 system is a multi-FPGA versatile platform for TDC measurements and digital readout [49]. It was originally developed for the HADES experiment at GSI. It consists of FPGA-FW, DAQ and calibration software implemented in the corresponding hardware. Four peripheral FPGAs can be configured to various needs and one central FPGA acts as central trigger system (CTS) and manages the whole data-taking process. It hosts a gigabit ethernet (GbE) controller, supporting DHCP and thus allows for easy integration of the whole system into any GbE network, provided that 48 V power are available. A UDP protocol takes care of the whole communication (data and SlowControl) of the DAQ-PC with the TRB3 platform and enables the user to communicate directly via GbE. Internally, the uniquely developed TRBnet [64] protocol provides a powerful, standardised way for trigger distribution, data transport, SlowControl handling and error propagation and implements so-called endpoints, which provide a well-defined interface for any subsystem such as the SKIROC2 ASICs. Various SFP-connectors enable a high bandwidth for data transport and allow to flash-program even the GEAR endpoint FW easily without any further equipment. Eventbuilding software for large systems is included as well

as an analysis software, even with online-display. Multiple SlowControl settings and the readout control is nicely available in a web-GUI.

The way the TRB3 is used as a back-end for HI-TREX is mainly as data-aggregator and networking platform providing synchronous communication to an arbitrary number of GEAR boards. Once, data is presented to the media-interface of the endpoint, it will be sent to the central TRB3 platform, packaged and transmitted to the DAQ-PC via GbE. In an easy to configure DABC software [3] the data are collected, and stored to disk.

IV.2.4 Peripheral electronic components

Following the topic of data processing, the next subsection briefly introduces the further software developed for data analysis. First, the TRB3-data need to be unpacked. As variable event sizes can be sent via UDP (events from no, up to three ASICs can be sent in one package) and furthermore these sub-packages do not need to be ordered in time (three independent endpoints), the ROOT-tree [19] being produced simply sorts header-data from ASIC-raw-data. Afterwards, the sub-packages of ASIC-raw-data are separated into physical events and are stored into their own ROOT-tree. In a next step, these individual physical events are sorted in time and the three ROOT-trees are merged again according to the respective timestamp. Hence, a correlated ROOT-tree with individual physical events is generated for further analysis. As for the calibration procedure, an automated fitting-routine was written for 3α-spectra producing a text-based calibration file. Due to the nature of analog storage in the SKIROC2-ASICs, not only each channel needs to be calibrated individually, but also each SCA of each channel in both shaping branches. Hence sufficient statistics is required to guarantee proper fit-results. Also, as the preamplifier of the SKIROC2A is designed to be non-linear at high input signals, this non-linearity also needs to be calibrated for each channel. This non-linearity is stored as a ROOT-spline for each channel in both shaping branches and can be referenced easily for further analysis.

Further software developed takes care of proper register loading during the start-up procedure of the TRB3 system. Furthermore, the SlowControl values required by the ASICs can be configured in text-based scripts and loaded via the TRBsc, as explained already earlier. An implementation in the web-GUI is straightforward and reasonable in terms of usability, as well as is a basic online display plotting the most important ASIC-data.

The required hardware-components to set-up a complete data-taking system require additionally a 48 V power-supply (for the TRB3-system), a GbE switch (best with glass-fibre connection) and a DAQ-PC (with two independent network cards), as well as a low-voltage distribution system (regulating the required power from the central 48 V to the required voltages for the GEAR boards). As auxiliary boards for the TRB3, a SFP add-on (for glass-fibre connection) and a Distribution board v3

(for trigger and clock distribution) are required for the HI-TREX setup. In case a synchronisation of the TRB3 is needed with any external system, the GPin add-on is helpful.

The only missing components for the HI-TREX implementation is the connection from the Hybrid-PCB hosting the ASICs to the GEAR board. Due to the space-constraints in the vacuum chamber, high-density connections are required. Rigid-flex PCBs have been designed to connect the ASICs to some feedthrough PCB. The feedthrough PCB simply connects two Hybrid-PCB modules to the outside of the vacuum. Here, either the same rigid-flex PCBs can be used to interface a 10-layer PCB serving as a backplane for two GEAR boards, or the backplane can be mounted directly on the feedthroughs.

IV.3 Integrated Setup: Conceptional developments

A monolithic detector stack design was developed to guarantee an easy handling for the user, which uses the available space most efficaciously and provides maximum protection for the embedded fragile DSSSD.

IV.3.1 Mechanical integration

Given by geometrical constraints (chamber) and reusing the existing target ladder of the MINIBALL setup, geometrical boundaries are defined. The choice for a trapezoidal arrangement of detectors was done according to III.4.3. The available technological limit for wafer production goes hand-in-hand with the required PCB-space for the readout electronics. This defines the maximum granularity which can be read out, being 192 per Hybrid-PCB. The mechanical mounting of the detector-stacks must be vacuum-tight, stable and additionally must use as few material as possible due to absorption of γ-rays for MINIBALL.

A 3D-printed holding structure was developed and prototypically tested (see picture IV.15a. First efforts involved epoxy-based resin material, which are cured by a laser-beam in inverted stereolithography (SLA). The principle accuracy of the method of 50 µm is sufficient, however either the resin's tensile strength is too low and the elongation too high to guarantee a stable and precise mounting structure for the HI-TREX boards, or the resin further cures under the influence of UV-light, or any other high-energetic radiation and then is too brittle to be used. As a consequence a different method of additive manufacturing to manufacture the mounting structure was exploited: Selective laser melting of metals or alloys. A prototype of aluminum was printed and investigated. As the mechanical characteristics correspond to those of the traditional machining technologies, sufficient stability was proven. However, the accuracy in the production of fine structures cannot be reproduced as well as in the SLA process. The idea hence is to use a basic aluminum-structure, onto which

fine structures made of resin can be glued. This guarantees both, mechanical stability and flexibility in mounting the Hybrid-PCBs. Further developments foresee the mounting of a conical structure hosting protection foils, or apertures.

The PCBs are mounted in a similar way as an extendable drawer, using a type of dovetail groove CNC-milled into the Hybrid-PCB (see IV.15b). Due to this mounting procedure, the necessity having the bondpads sunken into the PCB as illustrated in IV.17 and IV.19 is obvious. An extremely compact and dense design of the HI-TREX setup is the result.

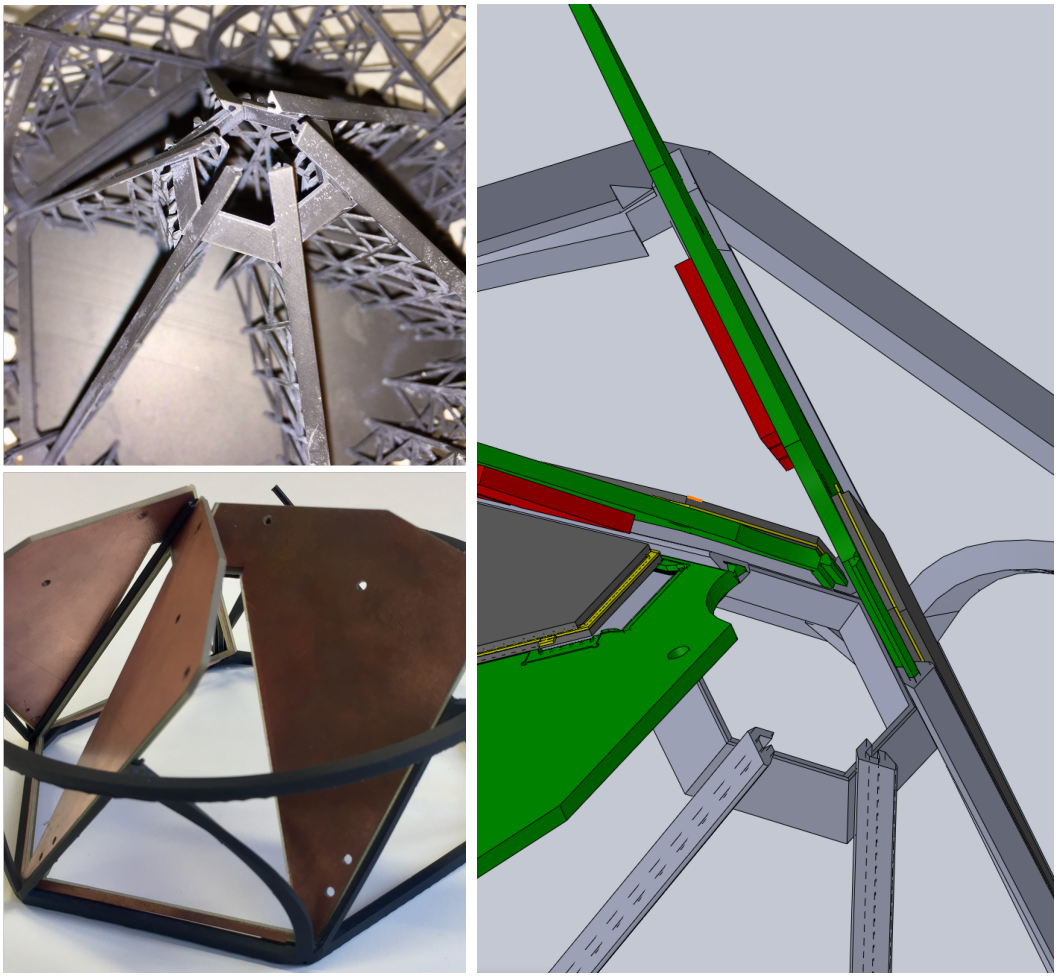

(a) SLA printed holding structure.

(b) Drawer like mounting.

Figure IV.15: Conceptional developments for the HI-TREX structure.

IV.3.2 Detector telescope: ΔE-E_{Rest}-E_{Rest}

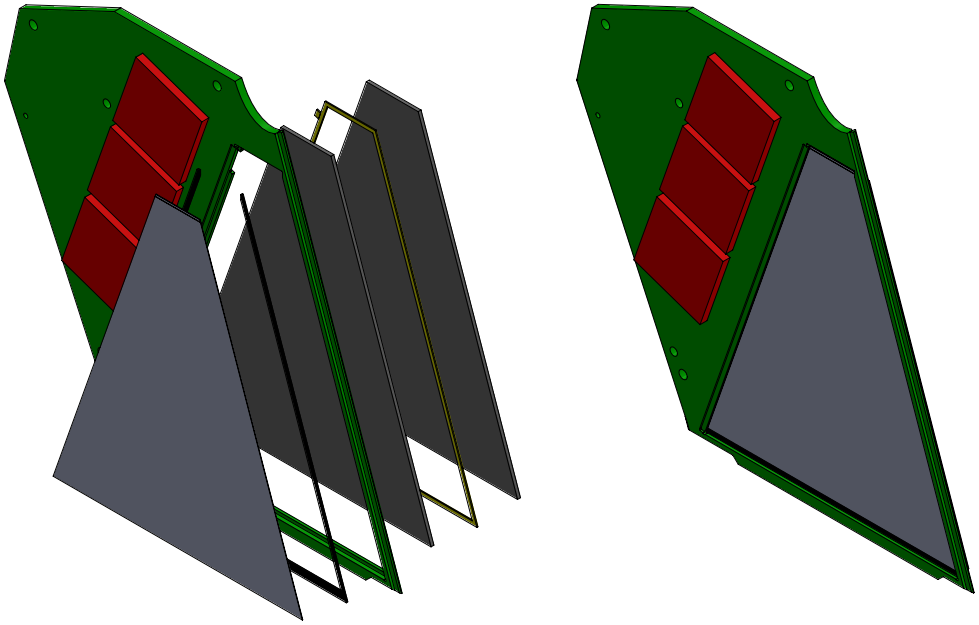

(a) Exploded view of the detector assembly.

(b) Actual, collapsed view. Note, that the DSSSD is completely sunken into the PCB.

Figure IV.16: Assembly of one detector-stack mounted on a common PCB. The red parts indicate the size of the SKIROC-ASICs, mounted in a BGA400-housing.

In figure IV.16a an exploded view of one detector-stack, mounted on a highly complex printed circuit board (PCB) can be seen. The collapsed view can be seen in IV.16b. The individual parts as seen from left to right in IV.16a are: DSSSD (light grey), Aluminum-Nitride (respectively silicon) frame (black) for matching of the thermal expansion coefficients of the PCB and the (brittle) DSSSD , PCB (green), E^1_{Rest} (dark grey), Gold frame (yellow) for contacting the ground potential and the second E^2_{Rest} (dark grey). The mounting and bonding procedure is quite complex due to the fragility of the DSSSD and the compact setup with one common PCB: Firstly, having the PCB produced, equipped with the necessary electronics components, contour-milled and electronically tested, the detectors can be mounted. The mounting of the DSSSD needs to be done first, as this is the most challenging part. Mounting and

bonding go hand-in-hand during this process, which is schematically proposed in the appendix B. Especially due to the fragility of the sensor, the idea of generating a second row of bondpads on the *n*-side evolved. This enables the required support during the ultrasonic wire-bonding, as otherwise vibrations would not be damped by this support structure and no sufficient force would be applied by the bond-wedge to guarantee a proper contact. In the appendix in figure A.2a this second row of bond-pads can be seen. Further details on the location of bondpads and milling contours of the detector-PCB can be found in figure IV.17. In the upper pictures, the top-view of the detector stack is shown. The parallel hatched area represents the location of the bondpads for connecting the *p*-side strips to the readout ASICs. This area is milled into the PCB, being on the same level as the DSSSD surface and thus guaranteeing an efficacious protection for the detector and as well for the bond-wires. The DSSSD thus is completely sunken into the PCB, which is required due to the mounting of the detector-stacks in a holding frame, as further detailed in section IV.3.1. The lower pictures show the bottom-view of the detector stack. Again, the parallel hatched area represents the location of the bondpads for connecting the *n*-side strips to the readout ASICs, whereas the criss-crossed hatched area shows an additional milling contour on the PCB, which is needed to contact the junction-side of the first E^1_{Rest} detector to bondpads located on an additional, small, rectangular PCB, which will be glued to the side of E^1_{Rest} at a position indicated by the milled contour which is not hatched in figure IV.17. It is also this PCB, which provides the ground connection to the Gold frame, glued in-between the backsides of the E_{Rest} detectors, and a bondpad for contacting the junction-side of the second E^2_{Rest} detector. From this small PCB wire-bonds are contacting the appropriate bond-pads on the common Hybrid-PCB. The E_{Rest} detectors can be mounted slightly shifted towards the major side of the trapezoid, to optimise the solid-angle coverage for the events with most interesting physics and to ensure access to the backsides of the membranes at any time.

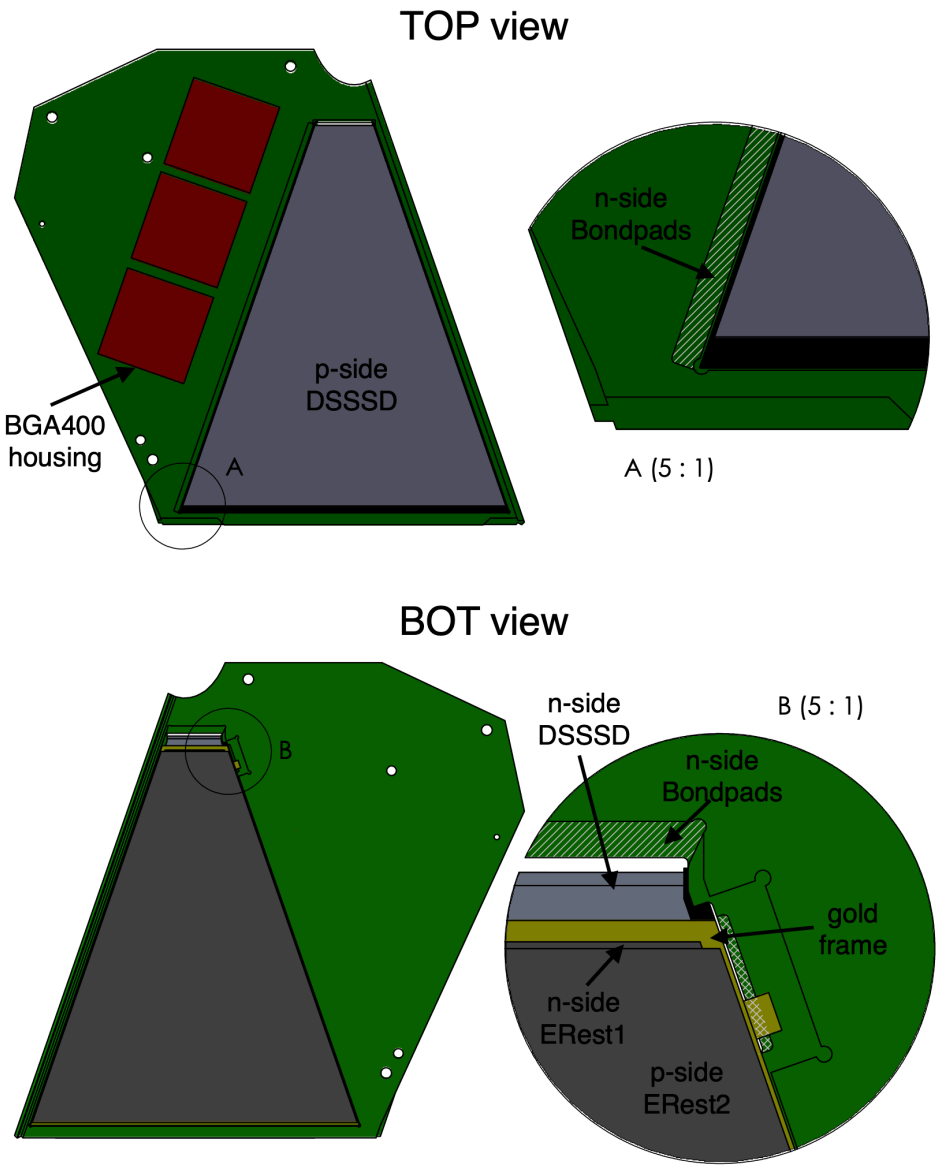

Figure IV.17: Details on the location of bondpads and milling contours on the detector-PCB. Please refer to the text and IV.3.3 for further details.

IV.3.3 ASIC integration and details on the Hybrid-PCB

The implementation of the silicon detector setup ΔE-E-E as well as the readout ASICs is done on one common printed circuit board (PCB) located inside the compact MINBALL target chamber and thus is in vacuum during measurements. The geometrical constraints defining the maximum detector area and the available PCB-space have already been discussed. A Hybrid-PCB has been designed and built to host the detector-stack, as well as two SKIROC2A and one SKIROC2-CMS ASIC. A fairly complex layer-stackup has been evaluated with the PCB-manufacturer IV-Schaltungen due to the need of being able to sink the DSSSD into the PCB for protection and mounting issues. The exact, well-balanced stackup can be seen in the appendix E. The decision to build a Hybrid-PCB was guided by the fact, that the combination of standard FR4 TG170 and Rogers RO4003 guarantees the best planarity of the final PCB and reduces warping effects during soldering at most. Special attention therefore has also been paid to the copper-filling of individual layers, which should be as symmetrical as possible also because of the warping.

Complex z-axis milling contours (see IV.19) are required for the embedment of the detectors: From the top-layer there are two different contours milled to $-0.9 \pm 0.05\,\mathrm{mm}$ and $-0.4 \pm 0.05\,\mathrm{mm}$ depth. The deeper one is required to glue the Aluminum-Nitride/silicon frame (see IV.3.2) hosting the DSSSD to the PCB. The shallower one hosts bondpads from an inner layer of the PCB to readout the *p*-side of the Silicon detector. Please refer to IV.19a for a CAD-view of the milled contours. On the backside of the PCB, three different depths have to be milled into the glass-fibre board: One passive layer ($-0.1 \pm 0.05\,\mathrm{mm}$) for glueing and fixing the $\mathrm{E_{Rest}}$ detectors and the aforementioned smalll 'bonding'-PCB, a second passive layer ($-0.4 \pm 0.05\,\mathrm{mm}$), whose needs were already detailed in IV.17 and one 'active' contour ($-0.4 \pm 0.05\,\mathrm{mm}$), hosting bondpads for the *n*-side readout. The milled contours which are 'active' are produced in a rigid-flex technology using no-flow prepregs to guarantee the bondpads being clean of any glue.

General features of the board are 6 layers, vias with 200 µm diameter, which are all filled-and-capped, as well as blind vias from the outermost layers, line-widths and clearances of 100 µm and chemical gold finish (ENIG). There are four holes for mounting located on the board as well as two fitting holes, which will be reamed into the PCB later for positioning and mounting during the 5-axis milling process, which is required to produce the white contours tentatively shown in figure IV.18.

Despite the connectors and the ASICs, there are a lot of passive components (mainly decoupling capacitors), with which the board will be equipped. The only further active IC-like components are the I^2C temperature sensors located directly underneath each ASICs footprint on the bottom side and one high-speed, single-supply operational amplifier with rail-to-rail output[6], which was designed as a

[6]The MAX4012 would have been used if the external triggering of the SKIROC2-CMS would not

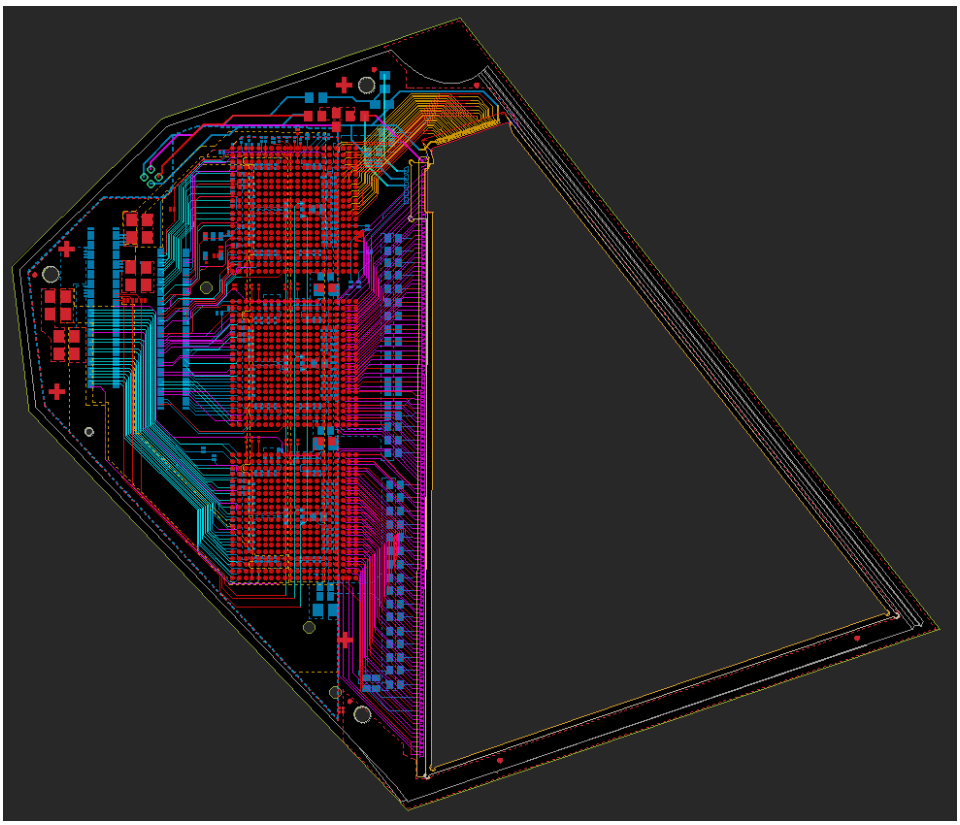

Figure IV.18: Hybrid-PCB's layout illustrating the high density and space-efficient use of the available PCB-space. The dimensions of the PCB are depicted in greenish colours. The milling contours for the detectors, being sunken into the PCB can be seen, as well as the various connections and pads in the different layers shown in different colours. The location of the bondpads for the SKIROC-ASICs packed in a BGA400 housing can be seen in the top layer (red). On the bottom side (blue) the high-dense, micro-pitch connectors with only 400 µm pitch (indicated in the top-left corner) provide the connection from the board to the front-end electronics GEAR.

have been able to be done via the output-trigger of the SKIROC2As due to timing constraints. See the firmware section of the GEAR-section for more details. In this case, there is a very special mode of operation of the SKIROC2-CMS in which only the hit-information of all 64 channels and no additional energy or timing information can be read. To speed-up the readout, the ASIC can be overclocked, however the output buffers of the appropriate pin are too slow and hence this rail-to-rail amplifier was successfully tested in a laboratory setup with the SKIROC2-CMS up to 200 MHz clock-speed, resulting in a dead-time of only $\approx 0.4\,\mu s$ between two hits in the Silicon detector.

backup during the layout-process of the PCB, in the case that the SKIROC2-CMS needs to be read-out in a very special 'probe' mode.

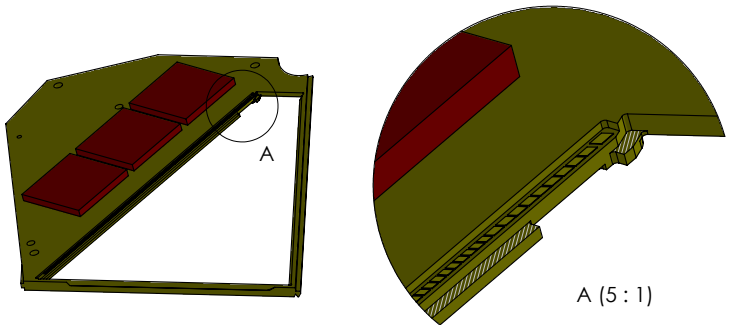

(a) Top view on the milled contours of the Hybrid PCB.

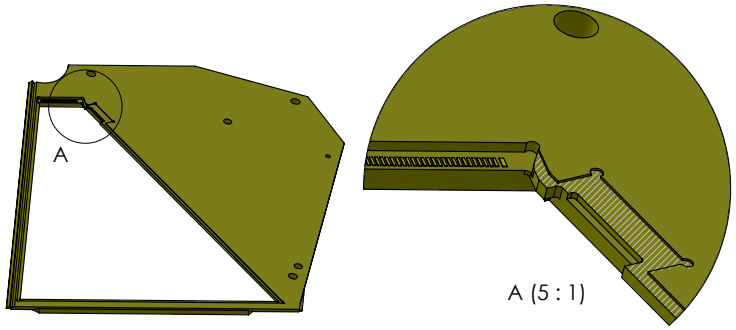

(b) Bottom view on the milled contours of the Hybrid PCB.

Figure IV.19: Details on the milled contours of the Hybrid PCB. The hatched areas represent the inactive layer for glueing and mounting. The other contours show the location of the bond-pads (yellowish), located on inner layers of the PCB.

There are three bias-lines and one bias-ground located on the PCB. The bias-lines are located on the outermost layers and are well separated from other signals wherever it was possible, to avoid creeping currents. The readout of the two E_{Rest} detectors can be done in three different ways, all foreseeably already prepared in the layout of the board: Either they can be read out via the biasing lines, the SKIROC2-CMS, or the SKIROC2A positioned in the middle of the board if two of the *p*-side channels located closest to the minor of the trapezoid are omitted (or regrouped with two other readout channels of the SKIROC2A ASIC). Anyhow, multiple *p*-side strips of the DSSSD need to be bonded together as the strip-number of 266 is not matching the number of readout-channels of 128. The reasons for choosing 266 strips on the *p*-side is discussed in section IV.1. Each two adjacent *p*-side strips are meant to be bonded together for 119 readout-channel, whereas for the 9 readout-channels

located closest to the minor side of the trapezoid the *p*-side strips are grouped in amounts of 3 (and 4 for the last one respectively). Hence the bondpads, at this side are slightly larger than the rest of the pads sunken into the PCB, as can be seen in the detailed view of figure IV.19a (the last pad is reserved for biasing the *p*-side).

A photograph of a mechanical dummy DSSSD fitted into the milled contour of the Hybrid-PCB can be seen in E.3.

A step-by-step description for the proposed production of the monolithic detector stack is detailed as follows:

- Production of Hybrid-PCB
- Surface mounting of ASICs and necessary parts
- Testing of equipped Hybrid-PCB with pulser
- CNC milling of outer contours for drawer-like mounting
- Testing of equipped Hybrid-PCB with pulser
- DSSSD mounting and bonding
  - Adhesive bonding of thermal foil for *p*-side protection
  - Wire bonding of secondary bonds at ohmic side of DSSSD
  - Glueing of ceramic or silicon frame on *n*-side
  - Removal of thermal foil
  - *n*-side placement on vacuum chuck
  - Placement inside the PCB millings
  - Wire bonding of *p*-side
  - Glueing of the edges of the support frame with elastic glue
  - Adhesive bonding of second ceramic or silicon support frame to the *p*-side outside the active detector area
  - Mounting of *n*-side bond carrier via Bluetape
  - Wire bonding of primary bonds at ohmic side
- Testing of equipped Hybrid-PCB with pulser and detector
- Glueing of secondary PCB to first E_{Rest} detector
- E_{Rest} mounting and bonding
  - Wire bonding of *p*-side to secondary PCB
  - Glueing of *p*-side to milled contour on Hybrid-PCB

  - Adhesive bonding of gold frame to *n*-side of first E_{Rest} and to secondary PCB
  - Glueing of *n*-side of second E_{Rest} to gold frame
  - Wire bonding of *p*-side of second E_{Rest} to secondary PCB
- Secondary wire bonds from secondary PCB to Hybrid-PCB
- Final testing of equipped PCB

Detailed, high-level technological developments, which are currently at the edge of possibility account for every requirement which were previously specified. Universality is a key feature and guarantees an adoption of the developed sensors and electronics to many nuclear physics experiments.

CHAPTER V

Experimental studies

Throughout the development of HI-TREX, experiments at three facilities have contributed important experiences and results to the success of this development. Experiments at the Munich tandem facility MLL made important contribution to the understanding of the ASIC, as well as the data-processing electronics. The non-linearity regime of the preamplifiers and the required peripheral components guaranteeing a stably working input-stage of the ASICs were investigated and understood. In an experiment at the Munich neutron source FRMII, the implantation profile of pin-diodes was examined and compared to SIMS-measurements, pathing the way to the shallow, ultra-thin and homogenous entrance-window of the DSSSD development. Finally, the basic requirements for radioactive beam experiments at CERN have been studied in an experimental campaign still with the 'old' TREX setup, but with the full upgrade of HIE-ISOLDE. The whole development was accompanied by a large series of measurements done in the laboratory with radioactive sources.

V.1 CERN: First transfer experiment with full HIE-ISOLDE setup

A study of yet experimentally unknown, excited states in the isotope ^{135}Sn was proposed [51] and accepted by the ISOLDE and Neutron Time-of-Flight Committee. The availability of all four cryomodules being installed at HIE-ISOLDE enabled energies of the ^{134}Sn-beam of 7.3 MeV/u. Thus, the one-neutron transfer experiment d(^{134}Sn, p)^{135}Sn in inverse kinematics was the first transfer experiment with such heavy, neutron-rich beams and the fully installed HIE-ISOLDE Linac. Besides from

the physics motivation, loads of experience could be gathered for the new HI-TREX setup.

Detailed GEANT4 simulations and Fresco calculations were performed in advance to the experiment conducted in autumn 2018. It was the first time, that TREX in its complete configuration was set-up.

V.1.1 Motivation

On the neutron-rich side of the nuclear chart, the region around ^{132}Sn is the focus of many efforts in both experimental and theoretical nuclear physics. As the *r*-process approaches ^{132}Sn from the neutron-rich $N = 82$ waiting point nuclei, and then proceeds along the $Z = 50$ isotopic chain towards more neutron-rich nuclei, the knowledge on the nuclear structure (masses m, neutron capture rates σ_n, β-decay half-lives $\tau_{1/2}$, fission barriers S_B, ...) is crucial input to the exact path of the r-process and the resulting elemental abundance distribution. The influence of the neutron capture rates on the distribution of the $A = 130$ peak (second peak in figure I.2) can be seen in figure V.1.

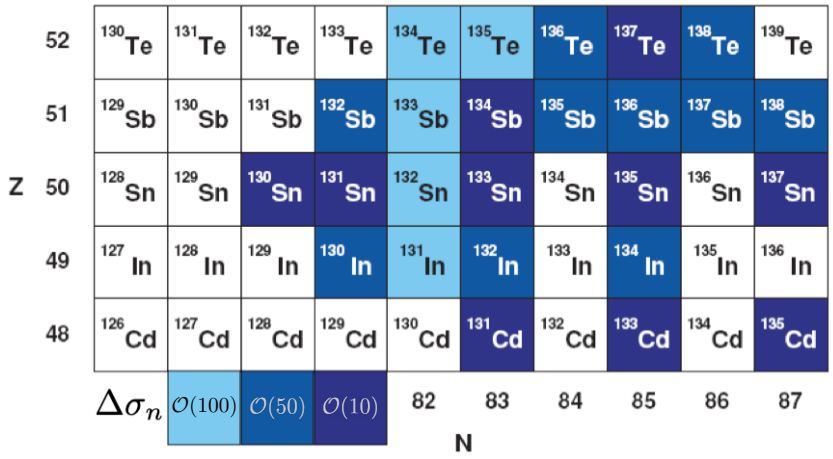

Figure V.1: Influence when varying the neutron capture rates of the shown isotopes by scaling factors denoted in the figure on the final abundance distribution of the $A = 130$ peak of more than 5% . Figure adapted from [84].

As the one-neutron transfer reactions (d,p) are as surrogate reactions for the neutron-capture process (n,γ) very useful tools for investigating astrophysical relevant nuclear reactions (see II.1), the first spectroscopy of ^{135}Sn will serve as a benchmark for nuclear theory. The main observables are the cross sections as well as the energies and the angular distributions of the outgoing protons which allow

for the determination of excitation energies, transferred angular momenta and spectroscopic factors. Shell model calculations need, apart from a set of interaction matrix elements, also spectroscopic information from the nuclei neighbouring the doubly-magic cores. E.g. the region north-east of ^{132}Sn requires the single-particle energies of states in ^{133}Sn and ^{133}Sb as input. The validity of the calculations can be tested only with nuclei further away from the core and therefore, keeping the magic closure at $Z = 50$, the spectroscopy of ^{135}Sn is the straightforward challenge for the predictive power towards neutron-rich isotopes [51].

V.1.2 Setup

MINIBALL consists of 24 High Purity Germanium (HPGe) crystals which are grouped in eight triple clusters with a common cryostat each [94]. Each crystal is a tapered, coaxial detector guaranteeing good angular coverage. The crystals are six-fold segmented, enabling a precise determination of the γ-ray interaction point for Doppler correction. XIA DGF-4C modules deliver energy and time information for each of the 168 signals [56]. At HIE-ISOLDE, all MINIBALL clusters are mounted on a flexible frame, allowing the optimisation of their positions for each experiment individually.

TREX is a versatile Silicon array consisting of 16 position sensitive ΔE-E telescopes providing energy measurement and particle identification. There are two types of telescopes: The so-called barrel detectors, quadratic resistive strip detectors, located box-shaped around the target and circular CD detectors of DSSSD type, covering the very forward and backward angles. Thus in the complete configuration, 66% of the solid angle are covered [14]. For a schematic view of the TREX components, please refer to the details in figure III.8a. The pitch of the position-sensitive barrel detectors is 3.125 mm, their thickness is 140 µm and the active area covers 50 mm × 50 mm. Mounted in close succession with same solid angle coverage are the unsegmented E_{Rest} detectors with thicknesses of 1000 µm and no segmentation. Like the barrel detectors, the annular CD detectors consist of four quadrants, but with different segmentation: there are 16 rings (pitch of 2 mm at the front-side of the DSSSDs and 24 radial segments (opening angle of 3.4°) at the back-side. Their thickness is 500 µm and the corresponding E_{Rest} thickness was chosen to be 500 µm in backward direction and 1500 µm in forward direction. A flexible foil system was installed at the forward barrel region, shielding the detectors from elastically scattered heavy ions. The Mylar foil had a thickness of $\approx$ 12 µm. The targets which were used were deuterated polyethylene CD_2 foils. For the Sn runs a thickness of 120 µg/cm^2, respectively 1.1 mg/cm^2 was used, the Xe runs used 1.3 mg/cm^2 whereas for the stable beam calibration with ^{22}Ne a thickness of 1.2 mg/cm^2 was mounted on the target ladder. The electronics used to read-out the TREX setup was based on standard Mesytec modules [37]. A detailed description of a very similar setup can be

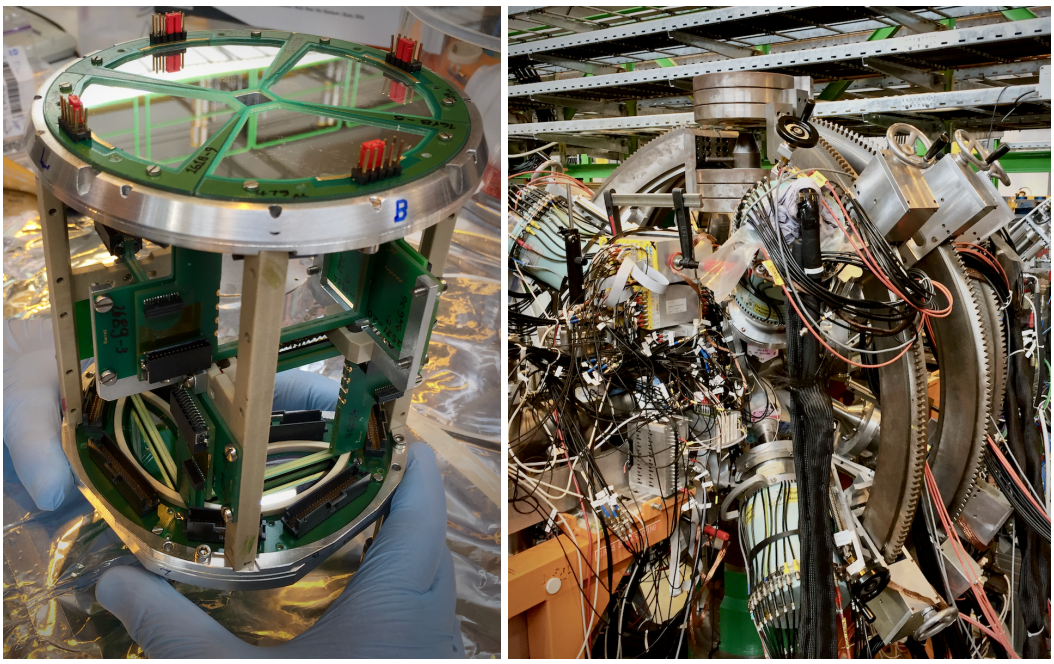

(a) TREX in its full configuration mounted on its holding structure.

(b) MINIBALL closed around the target chamber hosting the TREX array.

Figure V.2: Experimental setup used at CERN.

found in the appendix of [44]. The only difference to the aforementioned transfer setup was the use of four instead of two trigger groups: Each quadrant Top, Left, Bottom, Right generates its individual trigger and readout request. The calibration procedure was guided by [42].

The setup of the experiment as proposed in [51] consisted of MINIBALL and the completely configured TREX array. Furthermore an ionisation chamber consisting of a Silicon detector and a gas-detector was mounted downstream of the MINIBALL setup for beam diagnostics [93]. The beam generation for the ^{135}Sn experiment uses a isotopically enriched, molecular ^{134}Sn^{34}S^{+} beam ($A = 168$) to eliminate Cs contamination. The molecules will be cracked in the REXEBIS. No RILIS is used. For the ^{133}Sn experiment, the same mass markers are used, whereas in the stable-beam experiment the ^{132}Xe was simply introduced in gaseous form into the beam-line without using the primary target.

At the beginning of the experiments, the reaction ^{22}Ne(d,p)^{23}Ne was used to determine the angles of each individual MINIBALL detector, which is required for a proper Doppler-correction. Furthermore, the transfer reactions enables a cross-check of all gain and threshold settings of the setup.

V.1.3 Beam conditions for the radioactive beams ^{134}Sn and ^{132}Sn

In both experiments, the required beam intensities were not reached. The maximum intensity for ^{134}Sn was $2.8 \cdot 10^3$/s and for ^{132}Sn $2.1 \cdot 10^4$/s respectively. The required value in beam-intensity for guaranteeing a statistical error per bin in the backward barrel of TREX, measuring the transfer reaction to ^{135}Sn being 2% or better, needs to be at least 10^4/s [51]. Compared to the $\approx 3.0 \cdot 10^5$/s obtained in a previous experiment [77], the beam intensity for ^{132}Sn was roughly one order of magnitude too low. The numbers for the beam-intensities have been deduced from γ-lines following the β-decays of the beam nuclei, being stopped at the target position inside MINIBALL: The 872 keV transition in ^{134}Sb and the subsequent decays to ^{134}Te, to ^{134}I until to the stable ^{134}Xe could be observed correspondingly. In the case of ^{132}Sn, the 993 keV γ-line in ^{132}Sb has been used. The error for the intensity of the ^{134}Sn beam needs to be considered to be larger than 50% as the branching ratios to excited states in ^{134}Sb and β-delayed neutron emission populating ^{133}Sb are only poorly known. For ^{132}Sn, the dominant error is the absolute efficiency of MINIBALL of $\approx$ 10%, yielding an intensity error of roughly 15%.

The beam composition at some points during the ^{135}Sn experiment can be seen in figure V.3. The spectra have been measured with the aforementioned ionisation chamber.

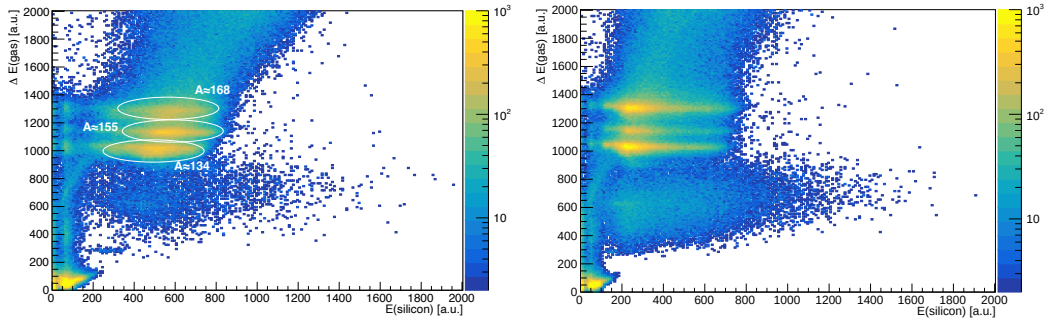

(a) Beam composition at the beginning of the experiment. The dominant contribution is in the $A \approx 155$ mass peak.

(b) Beam composition after changing the primary target and mass marker heating; shortly before the primary target broke down.

Figure V.3: Beam composition measured with the ionisation chamber, mounted downstream of MINIBALL. Note the decrease in energy measured by the Silicon detector due to radiation damage and the much stronger $A \approx 168$ peak with respect to the $A \approx 155$ peak in figure V.3b compared to V.3a.

As shown in the ionisation chamber plots, there is more than only a single mass

present in the beam composition. Comparing SRIM-simulations [106] to the measured spectra concludes together with prompt γ-spectra measured having the beam stopped within MINIBALL and further time-of-flight measurements, the operators of the HIE-ISOLDE Linac had done, that the three main components are nuclei with mass $A = 134$ and the corresponding isobaric contaminations, an unidentified $A \approx 155$ contaminant and stable $^{168}Yb^{39+}$, due to the - within the resolution power of the mass separator attached to the REXEBIS - same A/q as $^{134}Sn^{31+}$. Many efforts have been done during the beam-time to improve on the beam quality (like heating the mass markers and the primary target, or changing the settings of the trap, refocussing and even re-phasing the whole accelerating structures); but none of them succeeded. The only notable difference was a shift in the ratios of the mass $A \approx 168$ and $A \approx 155$ to the mass peak $A \approx 134$ (figure V.3).

As the beam-composition did not improve significantly for ^{134}Sn, a re-measurement of the experiment originally conducted by [46] was agreed on. However, the situation for the ^{132}Sn beam was very similar in terms of beam contamination, but the prompt, Doppler-corrected spectra (please refer to the appendix F for more details) identified unambigously ^{166}Yb as the overwhelming component via the observed transitions $6^+ \rightarrow 4^+ \rightarrow 2^+ \rightarrow 0^+$.

V.1.4 Stable beam experiment d(^{132}Xe, p)^{133}Xe

To show the general feasibility of transfer reactions with MINIBALL and the TREX setup with heavy, high energy beams at HIE-ISOLDE energies, a stable ^{132}Xe beam was produced with 7.2 MeV/u beam energy. Contrarily to the previous experiments, no overwhelming beam contaminants seemed to be present. The prompt γ-ray spectrum of the reaction d(^{132}Xe, p)^{133}Xe is shown in figure V.4a.

The strong 463.7 ± 0.2 keV line ($\sigma = 4.2 \pm 0.2$ keV) could be assigned to the decay of the 1071 keV-$7/2^+$-state to the 607.9 keV-$5/2^+$-state. However, this assignment needs to be treated with caution, as explained below. Next to this strong transition, there are three more peaks visible at 563.7 ± 0.7 keV and 661.8 ± 0.7 keV, as well as at 124.5 ± 0.9 keV, but which are not of any known transition in ^{133}Xe.

Coupled-channels DWBA calculations have been done with Fresco [86] for the population of various states in ^{133}Xe. The dominant differential cross-sections in the laboratory frame are the transfer cross section to the $3p3/2$ shell at an excitation energy of 3.2 MeV ($\Delta L = 1$) and the transfer to the $2f5/2$ shell at the same excitation energy. Furthermore, almost equal contributions come from the $2f7/2$ orbital at two slightly different excitations ($\Delta L = 3$). With a Q-value of the reaction of 4.099 MeV, the preferred population of energetically highly excited states can be well understood.

Measured transfer cross-sections as shown in [50] at a beam-energy of 5.8 MeV/u populated predominantly the 0.0 MeV-$3/2^+$-state ($\Delta L = 2$) and an excited 1.59 MeV-

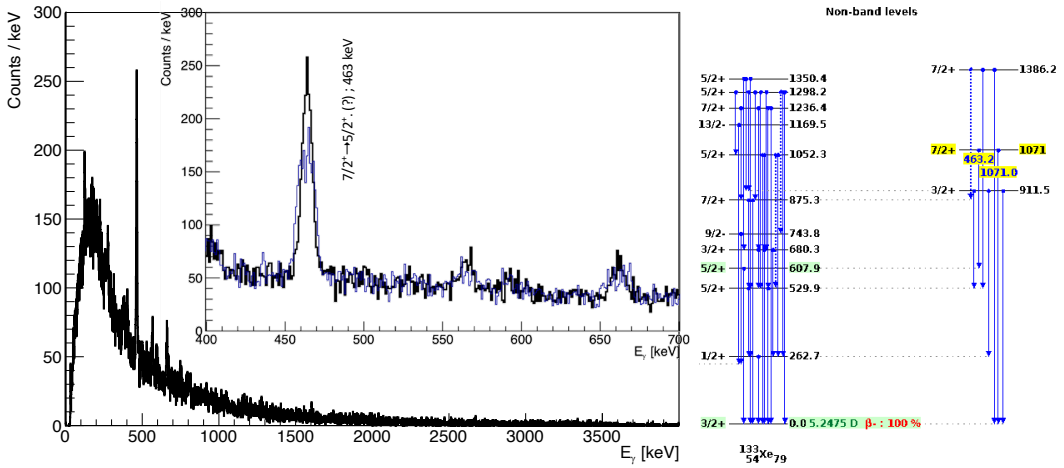

(a) Doppler-corrected γ-ray spectrum gated on prompt particle-γ coincidences (within 100 ns time difference).

(b) Level scheme of ^{133}Xe taken from [29]. Highlighted is the decay of the populated $7/2^+$-state.

Figure V.4: Prompt γ-ray spectrum of the ^{133}Xe experiment together with part of its known level-scheme. The black histogram in the inlet of V.4a represents the Dopper-corrected spectrum for the transfer reaction, whereas the blue one shows the Doppler-correction for the beam kinematics only.

$5/2^+$-state ($\Delta L = 2$). A tentative assignment of a (not yet confirmed) 3.0 MeV-$(7/2^+)$-state ($\Delta L = 4$) was made in this measurement.

Assuming a population of the 1071 keV-$7/2^+$-state in the transfer reaction, a significant amount of the transfer cross section would be detectable in the backward barrel according to the Fresco calculation shown in V.5. A cut on the prompt 463 keV γ-ray deexciting the $7/2^+$-state and a cut on the prompt 662 keV γ-ray produces the particle distributions shown in V.6. The corresponding spectra for cuts on the two remaining γ-peaks can be found in the appendix in F.7 and F.8.

The distribution of particles in coincidence with both γ-rays does however not fulfil the expectations according to the DWBA-calculations: Almost no statistics is present in the backward region of the barrel detectors. Most statistics is located in the forward barrel region and furthermore lies within the $E - \theta$-splines of elastically scattered deuterons and protons. An analysis of the specific energy loss of these particles identified them unambiguously as protons. Due to the overlapping splines of punch-through protons and elastically scattered ones, further kinematical cuts on the particles are hard to motivate.

The missing transfer protons in the backward barrel region are one complication

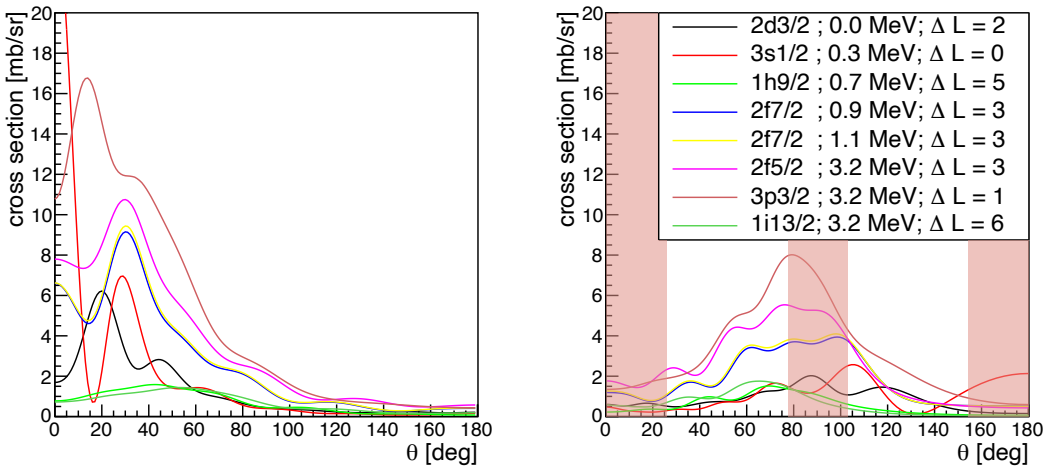

Figure V.5: Fresco calculation for the reaction d(^{132}Xe, p)^{133}Xe at 7.2 MeV/u beam energy. The differential cross-section is shown for the transfer to various states - some of them are hypothetical - as indicated in the legend in the right plot. The left distribution is for the centre-of-mass system and the right for the laboratory-system correspondingly. The reddish parts show the solid angle not covered by the TREX-barrel detectors.

in assigning the 463 keV γ-ray to a direct population of the 1071 keV-$7/2^+$ level. Second, the lack of the direct deexcitation of this state to the ground-state, as well as the subsequent decay of the 607.9 keV-$5/2^+$-state, which is missing as well indicates either a wrong level scheme in [29], or a wrong assignment of the observed transition to the 1071 keV-$7/2^+$-state.

Concerning the first case, the original data on the 1071 keV-$7/2^+$-state in ^{133}Xe are published in [57]. The spectrum, which is in coincidence with the 608 keV γ-ray deexciting the $5/2^+$ state to the ground level only shows the 463 keV and a 1093 keV ($(7/2) \rightarrow 5/2^+$) line. No direct ground-state transition is present. However, the 608 keV γ-ray should be visible in a prompt $\gamma\gamma$-coincidence. The corresponding, doppler-corrected two-dimensional spectrum can be seen in the appendix in figure F.11. A gate on the 463 keV γ-ray reveals the spectrum shown in figure V.7. Compared to coincident background spectra, a statistical enhancement of about $^2/_3$ is observed, however no statistically significant peak is visible. The structure at 660.7 ± 1.3 keV might form some peak, as well as the there might be a coincidence around 2100 keV or even around 3300 keV, however no conclusive statements can be made as a result. Especially the absence of any other line in the clinically pure gamma spectrum does not help in consolidating the assumption of the production of ^{133}Xe.

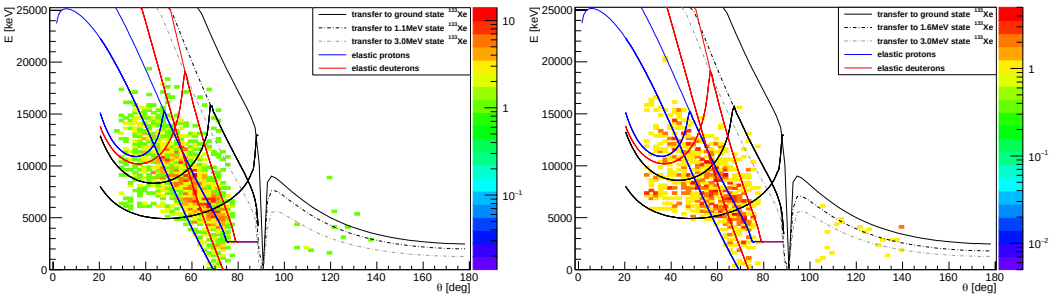

(a) $E - \theta$ distribution of particles in coincidence with the 463.2 keV γ-ray. The transfer to the 1071 keV-$7/2^+$-state is shown together with the kinematics of the transfer to the ground state and a 3.0 MeV excited state.

(b) $E - \theta$ distribution of particles in coincidence with the 662 keV γ-ray. The transfer to a 1.6 MeV state is shown together with the kinematics of the transfer to the ground state and a 3.0 MeV excited state.

Figure V.6: Prompt particle distribution in the laboratory system with overlaying kinematical splines from elastic scattering and transfer reactions. In forward direction, the punchthrough-splines are shown additionally. Again, the energy resolution was modelled and the influence of the protection foils was taken into account. The splines for the excited states were included to guide the eye.

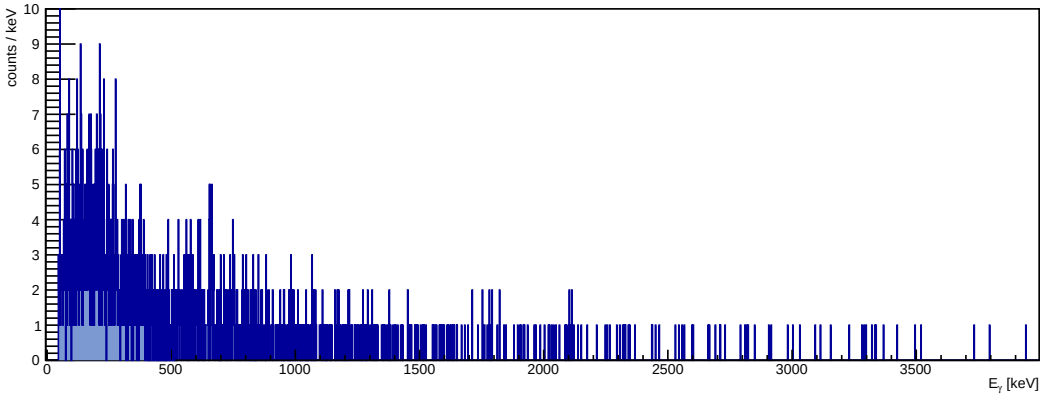

Figure V.7: Prompt γ-coincidence spectrum of MINIBALL with 1σ-gate on the 463 keV transition.

As the ionisation chamber was not in use during this stable beam run and no other system monitoring the beam-composition was present, the only thing to conclude on the beam composition is to compare the off-beam γ-ray spectra of the previous radioactive run to the current stable-beam run. Off-beam spectra means an acquisition of data during two EBIS pulses. This enables monitoring of the

background behaviour and β-decays of possibly implanted radioactive ions. The spectrum shown in V.8 is representing the difference of the γ-ray spectra obtained in the off-beam window of the experiment with the strong ^{166}Yb contamination and little of the radioactive ^{132}Sb (see the previous subsection) and the spectra obtained in the subsequent ^{132}Xe run. The spectra are not normalised in time to each other. Most of the dominant transitions were identified as results of the β-decay of ^{132}Sb. Nicely, the influence of the half-lives of the ground-states of the corresponding β-unstable isotopes can be seen, as e.g. the ^{132}Xe transitions are consistently more dominant in the spectrum taken at later times but therefore lacking of the ^{132}Te transitions.

The important information is, that no peaks are observed which are solely present in the ^{132}Xe-beam run. This allows at least the conclusion on the beam being made of stable isotopes.

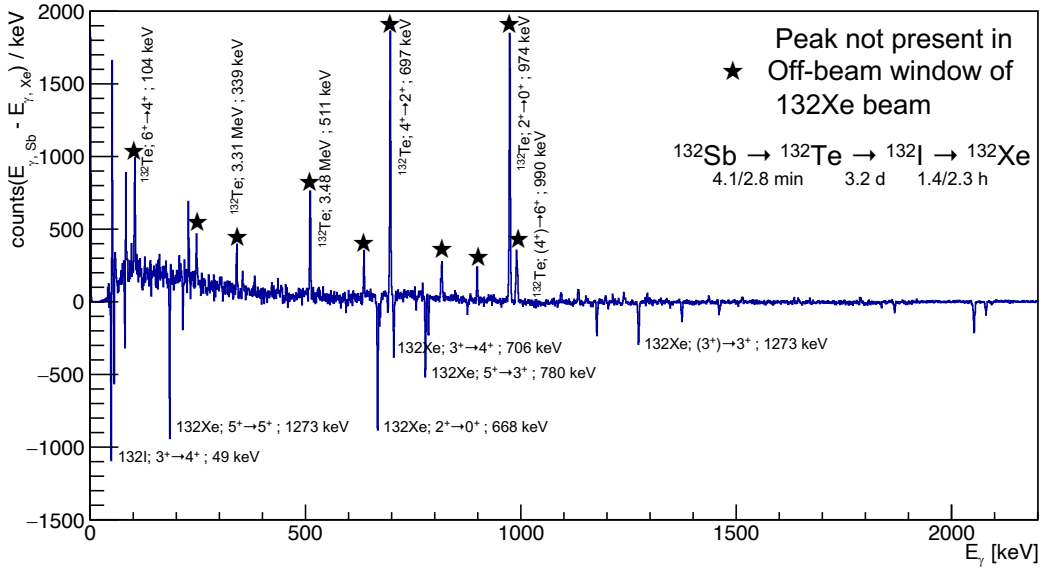

Figure V.8: Difference of the off-beam spectra acquired in the ^{132}Sb run and in the ^{132}Xe run. The peaks marked with an asterisk denote peaks which are not present in the Xe-run. Both runtimes have not been normalised to each other. The most dominant transitions have been identified.

PACE4 [35] calculations have been performed to evaluate the contributions in the cross-section from fusion-evaporation reactions. Dominant channels in the fusion with deuterium, carbon, nitrogen and aluminum were found to be ^{132}Cs, ^{138,139}Nd, ^{140}Pm, and ^{147}Tb and ^{150}Dy, respectively. However, the observed proton distribution does not reproduce the estimates from the PACE4-calculations. Furthermore,

again the clinically pure spectrum with the single, dominant 463 keV transition - suggesting a very unique decay branch - does even seem to be more unlikely with regard to the statistical population of many states in a fusion-evaporation reaction compared to the usually much more selective transfer reactions. In addition, the Doppler correction on the transfer reaction kinematics would then not result in any sharp peak.

Investigations of the prompt timing peaks (see appendix F.10a, F.10b and F.10c) and their variation in shape, when e.g. looking at the prompt particle timing when gating on the 463 keV transition, did not show any hint.

For completeness, another scenario can be constructed, when ignoring the exact energy calibration of the germanium detectors. Ignoring means in this case, that only for this data-set, the energy calibration can be assumed to be slightly off, whereas in the preceding and succeeding experiments, the measurements with the calibration sources yield exact energy values. Assuming such a slight miscalibration, the 463.7 keV transition can be interpreted as a 464.5 keV originating from the deexcitation of the first $2+$ level in ^{132}Ba. A contamination of barium is not likely to stem from the EBIS source itself. However, there is the possibility, that the barium was implanted during the previous Sn runs as a molecule into the EBIS in large quantities [97].

To summarise, the following partially contradictory conclusions can be drawn: The analysis of only the particle distributions, is severely limited by the missing particle identification capability of TREX in the forward barrel region due to the overlapping splines from elastically scattered protons, deuterons and punchthrough events and a missing resolution power like in the Zn-experiment in III.3. By consulting the information gained by MINIBALL, a prompt particle-γ correlation results in a clinically pure γ-spectrum, which is dominated by the 463 keV transition. This suggests a very specific population of a single-particle state in a transfer reaction. The principally suitable 1071 keV state would have to coincide with the following 608 keV transition, which is not observed. Additionally, the associated kinematical distribution of the corresponding protons is strongly peaked at forward laboratory angles, which is unusual and can not be properly explained by DWBA-calculations. Inelastic excitations of ^{132}Ba are possible but unlikely in terms of a otherwise properly working γ-array calibration and fusion-evaporation processes can be nearly excluded by the lack of appropriate (known) transitions and as the Doppler correction procedure only yields minimum peak-widths when using the transfer reaction kinematics.

Still there is the possibility, that an isomeric state at high excitation energy has been produced in a transfer reaction. A recent multi-nucleon transfer measurement [48] of a millisecond $23/2^+$ isomer in ^{133}Xe has shown this state at 2107 keV being fed by a 465 keV and 468 keV deexcitation. Linking the possibly coincident observation of the 2.1 MeV γ-ray from figure V.7 to a similar - maybe not isomeric, but highly

excited in energy and spin - state is nothing but speculation in view of a moderate differential cross-section in a (d,p) transfer reaction.

On the positive side, the experiment demonstrates the absolute necessity of upgrading the silicon detector array. The principle feasibility of transfer experiments with MINIBALL in conjunction of a silicon detector array has been demonstrated. Much experience was gained in understanding the electron problematics. It was shown, that the use of highly segmented DSSSDs solves this issue. The importance of a proper particle identification in the forward laboratory angles was emphasised as well as the need to have a low-noise electronics readout with good resolution, especially in the backward barrel region, in order to account for the kinematical compression of the transfer states. In detail, the backward trigger threshold is limiting the possibility to measure any possibly highly excited state.

V.2 FRMII: Implantation testing

This section deals with the experiments carried out at the Munich neutron source FRMII. Nuclear reactions were used to investigate the dead-layer of various Silicon PIN-diodes which have been produced with different implantation profile parameters. The goal of this experiment hence is to provide feedback for the sensor supplier and prove the reliability of some new implantation and annealing methods as already touched in section IV.1.

V.2.1 Motivation

There are various parameters, which can be tuned in order to obtain a certain depth distribution of the p^+ implant: As illustrated in the measurement V.9a, adjusting the peak-temperature and the time of the rapid thermal annealing process of the sample, results in differently diffused acceptors in the silicon bulk. The original distribution, shown in green, is the result from the implantation process. The method used 2 kV of accelerating potential to implant a dose of $1E16\,\mathrm{atoms/cm^2}$ through 20 nm of SiO_2 thickness.

The SIMS measurements in V.9b show the influence of the implantation process parameters like the implantation oxide thickness and different accelerating potentials. The implanted dose was again $1E16\,\mathrm{atoms/cm^2}$. Very differently to V.9a, the depth profile is not as shallow and decreases as steeply, but much broader and also shows some maximum concentration at around 10 nm depth. This is due to the higher accelerating potentials and the thicker oxides, which introduce a much higher energy straggling as in V.9a. Furthermore the overall concentration is lower as more boron remains in the absorbing SiO_2 layer during the thermal diffusion and annealing.

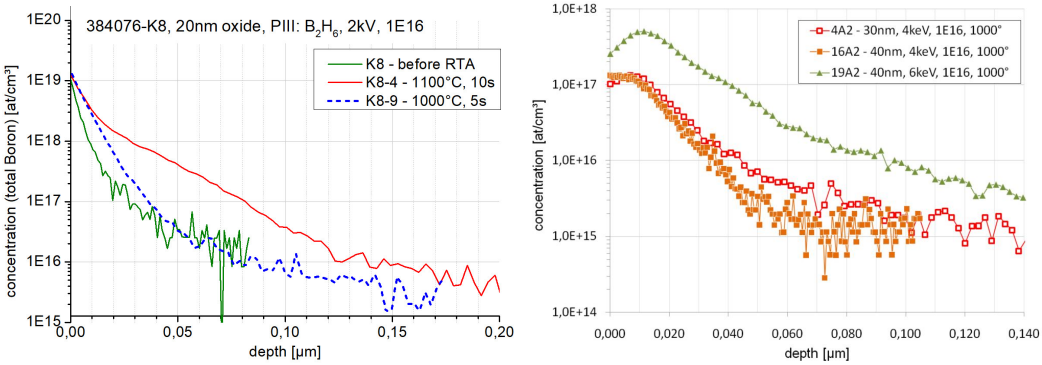

(a) Influence of the rapid thermal annealing parameters on the acceptor depth-distribution.

(b) Effect of the implantation process parameters: oxide thickness and accelerating potential.

Figure V.9: Various SIMS (secondary ion mass spectrometry) measurements of differently processed wafers. The measurements were kindly provided by [102].

Confiming the SIMS measurements and proving a working *p*-*n*-junction with as little as possible boron concentrations in a working detector under realistic conditions is the goal of the experiments done at the FRMII.

V.2.2 Setup

The experiment makes use of two different neutron-capture reactions: ^{6}Li(n, α)^{3}H and ^{10}B(n, α)^{7}Li. As the energy of the neutrons is as cold as $\approx 1.83\,\mathrm{meV}$, the thermal neutron-capture cross section for the Lithium reaction scales from $\sigma^{n}_{therm} = 940\,\mathrm{b}$ [68] according to the optical theorem [12] to approximately $\sigma^{n}_{cold} = 3.5\,\mathrm{kb}$. The value for the cold neutron capture for ^{10}B is even higher ($\sigma^{n}_{therm} = 3.8\,\mathrm{kb}$ [68]). The reaction products have a very specific energy and are basically emitted at rest due to the small kinetic energy of the neutrons: The alpha and tritium products from the ^{6}Li-reaction have an energy of $E_{\alpha} = 2.05\,\mathrm{MeV}$ and $E_{t} = 2.73\,\mathrm{MeV}$, whereas in the ^{10}B-reaction, two dominant disintegrating channels are present. The Lithium can be emitted at $E_{Li} = 1.02\,\mathrm{MeV}$ or $E_{Li} = 0.84\,\mathrm{MeV}$, whereas the alpha particle's kinetic energy is $E_{\alpha} = 1.78\,\mathrm{MeV}$ and $E_{\alpha} = 1.47\,\mathrm{MeV}$ accordingly.

Having a properly calibrated readout electronics and having the distribution of the target nuclei only on the surface with a very well defined thickness[1], it is possible to use the energy loss of the aforementioned products in the inactive volume of

[1] In case of the boron target, a B_4C layer with a thickness of only 10 nm on a silicon wafer was used. For the lithium experiment, a Mylar-foil with 2 µm of LiF was mounted at the target position.

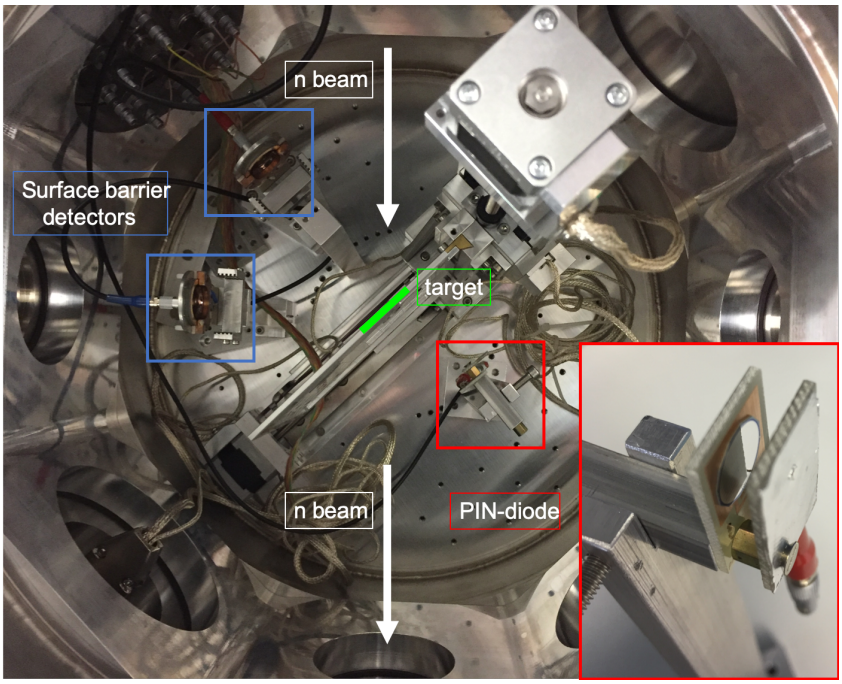

Figure V.10: Photograph of the experimental setup at the FRMII. The neutron beam enters the vacuum chamber from the top. The detectors are highlighted by coloured boxes.

the entrance window to calculate the effective dead-layer thickness of some Silicon sensor.

The setup of the experiment can be seen in figure V.10. The target was mounted on a movable target stage and two surface barrier detectors were used to calibrate the electronics and provide comparative measurements. Various circular-shaped Silicon PIN-diodes have been produced by CiS, each having different dead-layers according to the varying implantation and annealing processes. Apertures were mounted in front of the detectors to constrain the active detector area as some non-uniform metallisation was processed at the edge of the diodes for wire-bonding purposes. For better means of comparability, the energies of the nuclear reaction products were measured with the surface barrier detectors[2], having a well-defined inactive entrance window thickness of 70 nm and the PIN-diodes with the same readout channel.

[2]Partially depleted silicon surface barrier detector from ORTEC; model AD-025-150-100 [70].

V.2.3 Results

The energy spectrum shown in figure V.11a is an overlay of the spectra measured with one specific PIN-diode (No. 8) with both the Lithium (red) and the Boron targets (blue). The origin of the peaks is labeled.

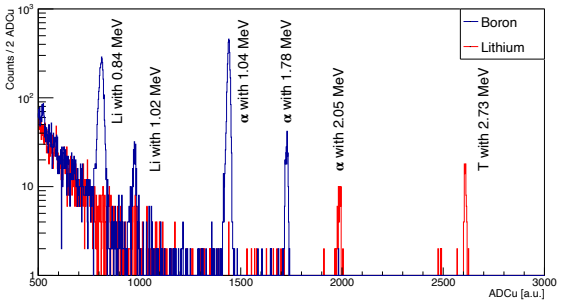

(a) Overlay of spectra acquired with both targets and the PIN diode No. 8. The Boron and the Lithium target have been used in different measurement times.

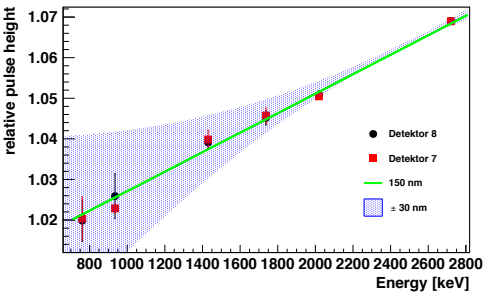

(b) Calibrated spectrum as in V.11a plotted against the relative pulse heights of two detectors with a linear fit representing a dead-layer of 150 nm with an 'error'-interval of ± 30 nm [98].

Figure V.11: Results from the measurement at the FRMII.

In figure V.11b, the dead-layer thickness of detector No. 7 & 8 was extracted by a fit to be 150 nm by comparing the mean value of the peaks measured with the surface barrier detectors to the mean values measured with the Silicon PIN-diodes and comparing these data to energy-loss calculations done with GEANT4, SRIM or ATTIMA. Comparing this entrance window thickness to the according SIMS-measurements results in the in IV.1 aforementioned concentration value of $\gtrapprox 1E16\,\mathrm{atoms/cm^3}$ for which the acceptors effectively contribute to the dead-layer. The production parameters for the detector No. 7 & 8 had been a oxide thickness of 40 nm, an accelerating potential of 10 keV, implant doses and annealing temperatures of $5E15\,\mathrm{atoms/cm^2}$ with 1000 °C and $1E16\,\mathrm{atoms/cm^2}$ with 900 °C respectively.The depth-distribution of the boron was of a similar shape as shown in the measurement labeled with '19-A2' in V.9a, however with approximately one order of magnitude higher Boron concentration. The peak concentration of around $1E19\,\mathrm{atoms/cm^3}$ has proven to result in a reliably working *p*-*n*-junction.

The measurements at the FRMII have led to an iteration of the implantation and annealing parameters, which resulted in the acceptor distributions as shown in the beginning of this section. With an effective dead-layer thickness of only 90 nm or even less, very promising implantation profiles have been produced recently, whose

capability of providing a p-n-junction for the DSSSDs developed for HI-TREX still needs to be shown.

V.3 MLL: Performance of new electronics

V.3.1 Motivation

This experiment was dedicatedly proposed to test the newly developed ASIC-based HI-TREX readout electronics under realistic conditions with heavy ions up to 110 MeV. In the laboratory tests, α-sources with energies up to 5.8 MeV can be used to test the low-energy branch of the dual-range preamplifiers in the SKIROC2-ASICs. However, testing of the high energy branch is not possible without using accelerated ions. The Munich tandem accelerator Maier-Leibnitz-Laboratorium hosts a 14 MVTandem-van-de-Graaff accelerator[65] and is able to deliver various stable ion species.

It was chosen to measure the elastic scattering of ^{58}Ni ions with an energy of 110 MeV as this ion beam can be easily produced with high intensity of up to 7pnA. The target was chosen to be 12 µg/cm^2 of ^{58}Ni deposited on a thin Carbon backing due to the large kinematic walk with the θ-angle. Hence, elastic bands from Ni and C should be visible, when measuring at certain angles in forward direction.

V.3.2 Setup

The setup of the experiment can be seen in figure V.12. The targets were mounted on a movable target stage, inserted through the lid of the vacuum chamber.

The detector used was a DSSSD[3] with 16 strips on each side with a pitch of 3.1 mm and a thickness of 100 µm. The 3α-spectrum shown in IV.6b was measured with this setup. This detector was mounted on a movable arm allowing to cover an angular range from 0° to 85° (centroid of the active detector area). As the distance of the detector to the target was $\approx$ 15 cm the solid angle of the detector itself is approximately 0.11 sr.

The detector strips were decoupled by a PCB hosting 10 nF capacitors. Although the blue PCB shown in V.12 embeds 2 SKIROC2A ASICs, only one is needed to readout the frontside of the DSSSD. The backside is read out by a SKIROC2-CMS in the externally triggered, special 'singles' mode (custom roll-clock; see IV.2.2.3 and IV.14). Flexible flat cables connect to the GEAR board outside the vacuum., which interconnects via glass fibres to the TRB3 platform. Hence, the complete electronics setup as illustrated in IV.8 is used with the only difference in the layout of the ASIC-board and the flex-PCB.

[3] W1(DS)-100, Type 9G/2M Silicon detector from Micron Semiconductor with a dead-layer (implant thickness) on the junction side of only 0.1 µm.

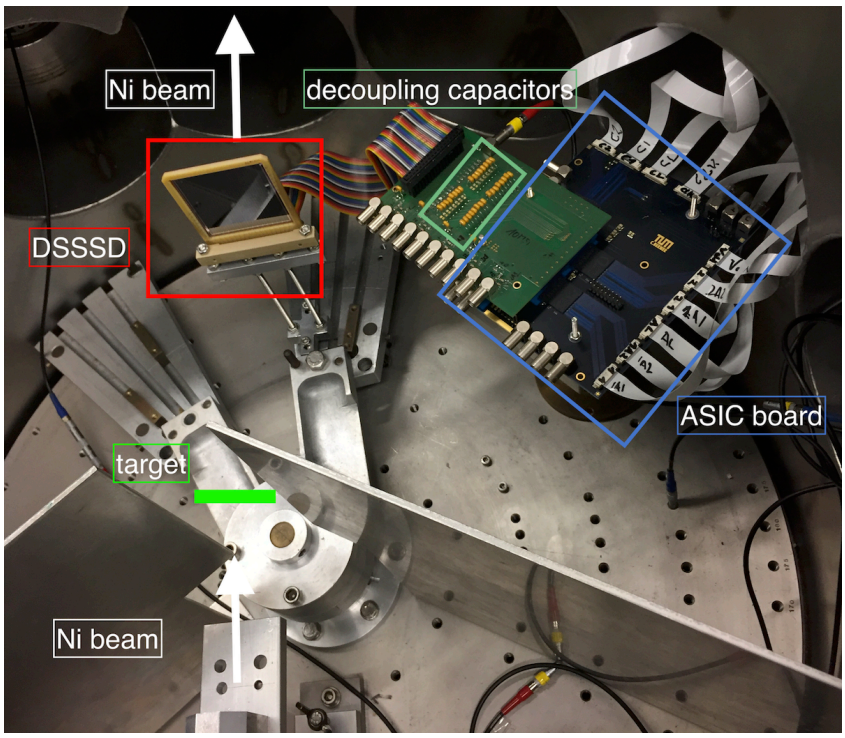

Figure V.12: Photograph of the experimental setup at the MLL. The ^{56}Ni beam enters the vacuum chamber from the bottom. The detector, mounted on a movable arm is highlighted by the red box. A PCB hosting decoupling capacitors (greenish box) is mounted on the blue ASIC-PCB. Flexible flat cables interconnect via some feedthrough to a backplane onto which the GEAR board is mounted.

V.3.3 Results

The elastic bands can be seen in the spectra shown in V.13. The feedback capacitance of the SKIROC2A was in this case set to 2.6 pF, allowing to measure energy depositions in the low-gain energy branch up to $\approx$ 80 MeV. Various settings have been tested. In this setting however, the whole low-gain range was used and simultaneously in the high-gain energy branch, the effect of the punch-through protons was observed with best resolution.

Three important results were observed. First, at high injected charge values a non-linearity of the ASIC preamps was observed. This can be seen best in the spectrum shown in V.13b: The energy deposition of the elastically scattered Carbon ions in the highest θ-bin still nicely coincides with the predicted value by calculation. However, at lower θ-values a deviation of the linearly calibrated energy deposition from the theoretical value can be observed. This behaviour is expected, as the preamplifiers

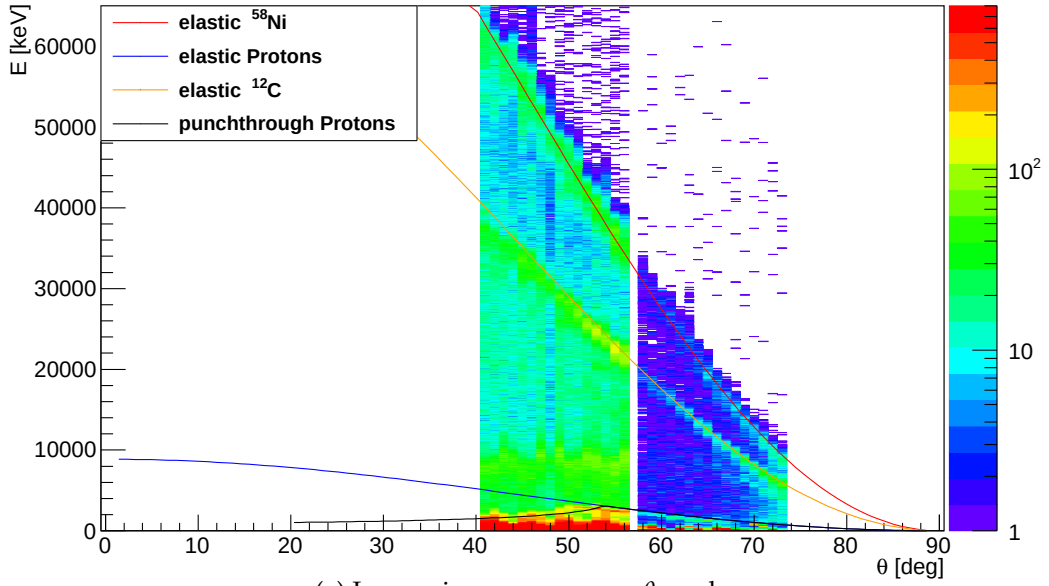

(a) Low-gain energy versus θ-angle.

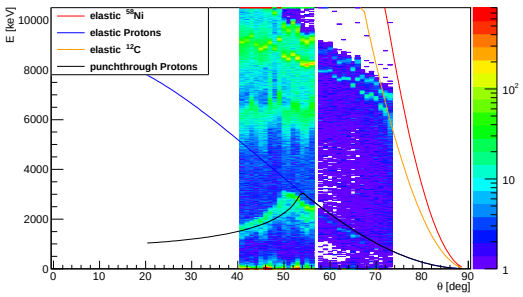

(b) High-gain energy versus θ-angle.

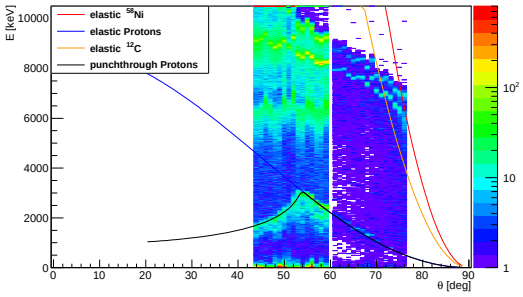

(c) High-gain energy versus the θ-angle shifted by 3°.

Figure V.13: Results from the measurement at the MLL. Calculated elastic splines are shown with punch-through splines for elastically scattered protons.

of the SKIROC2A were dedicatedly designed not to simply saturate at a maximum charge deposition, but to exhibit some non-linear behaviour, to guarantee a largest possible input-range coverage. In V.4, it is shown, that this non-linearity can be reliably calibrated with almost no draw-back in energy-resolution.

Second, protons have been observed punching through the 100 µm thick Silicon detector. However, from the comparison of V.13b and V.13c and the curvature of the calculated punch-through splines, the target as the origin of these events can be excluded. Shifting the measured high-gain energy by about 3° to higher θ-values nicely fits the theoretical energy distribution. As a possible origin a defocussed

beam, scattered at e.g. the second target made of polyethylene which was mounted in the vacuum chamber as well would explain this observation. A calibration issue can be excluded according to IV.6b.

Third, the behaviour of the ASIC was investigated when introducing very high charges or high rate at the inputs of the preamplifiers. Bringing the DSSSD to the very forward region and thus increasing the particle rate, or shooting the 110 MeV Ni-beam directly into the detector, without having any target mounted, both resulted in the same behaviour. It was observed, that at a certain beam intensity, or at high enough charge introduction, individual channels stop to measuring and stop to trigger. The reason for this behaviour was determined in missing leakage current at the preamplifier inputs, which is dedicatedly required to reach the quiescent bias level of the input transistors and guarantee a consecutive measurement.

It is noteworthy to mention the extraordinary low trigger threshold, which was able to be set as low as 20 keV without any special measure. The system performance was very stable and all components worked smoothly as expected. Especially grounding was not an issue.

V.4 Lab: Resolution, linearity, capability and scalability

The general understanding of the ASICs performance has been tested in the laboratory with various methods. A full setup consisting of various front-end boards as shown in V.12 with multiple GEAR boards and a central TRB3-system was successfully tested. All tests with a pulser make use of the internal calibration capacitance of 3 pF implemented in each channel of both SKIROC2A and SKIROC2-CMS ASIC. The pulser frequency - when stated - is constant in time.

As already mentioned in section IV.2.2.3, two basic readout speeds are implemented for the SKIROC2A: The standard 5 MHz readout speed and an accelerated 40 MHz mode. The 50% trigger efficiencies for a full chip were measured to be 1.5 kHz and 3.8 kHz respectively at an ADC resolution of 12 bit. Decreasing the conversion time by choosing only 10 bit ADC resolution, yields roughly 10 kHz for the 40 MHz transmission mode. Note that the instantaneous 50% efficient trigger rate can be as high as 28 MHz due to the SCAs.

Plot V.14a shows the pedestal variation of the SKIROC2A with temperature measured directly underneath the ASIC. The ENC increases non-linearly from $\sigma^{ENC}_{20.7^\circ\mathrm{C}} = 1.390 \pm 0.007 ADCu$ to $\sigma^{ENC}_{63.3^\circ\mathrm{C}} = 2.466 \pm 0.121 ADCu$. The increase in gain is linear with increasing temperature according to V.14b. Nonetheless, cooling in vacuum can be omitted in the case of HI-TREX, as the resolution-dependency on the temperature is on the one hand negligible small compared to the increase of the ENC due to the capacity of the detector and the cabling, and on the other hand the gain-shift can be removed by calibration, as the temperature values are

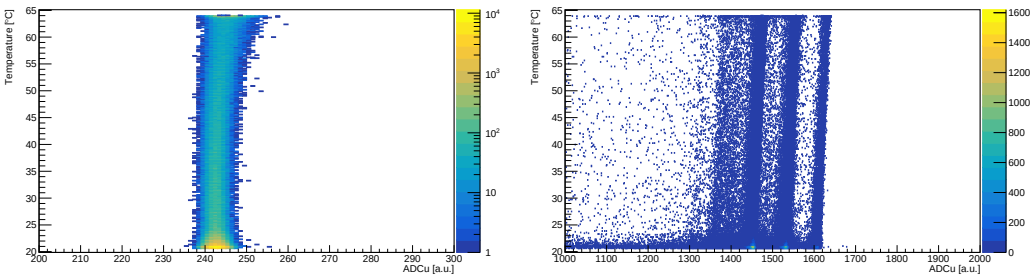

(a) SKIROC2A's pedestal of channel 46 and SCA *No*.8 plotted versus the temperature measured directly underneath the ASIC.

(b) High-gain response of channel 52 and SCA *No*.8 versus the temperature. Measured with a 3α-source without an aperture in front of the detector.

Figure V.14: Influence of the temperature on the ENC and the gain of the SKIROC2A.

constantly monitored and written into the data stream. The mean distribution of the pedestals is only varying within 8 ADC units throughout both ASICs and the width is constant as well, hence suggesting an adequate dimensioning of the power supply throughout the whole chip and PCB. If preferred, the (marginal) influence of the pedestal spread on the trigger threshold can be compensated by using the individual 4 bit DACs per channel.

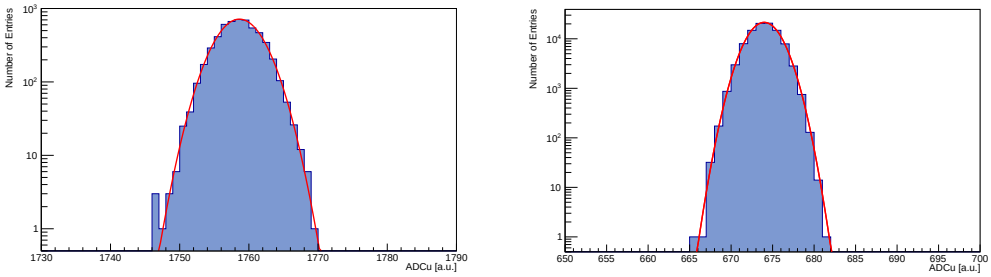

(a) SKIROC2A response at channel *No*. 1 and SCA *No*. 0 measured.

(b) SKIROC2-CMS response at channel *No*. 48 and SCA *No*.11.

Figure V.15: Pulser measurement determining the ENC of both SKIROC2A and SKIROC2-CMS. The pulser amplitude has been set to positive 70 meV for the SKIROC2A and negative 70 meV for the SKIROC2-CMS. A gaussian fit has been used to determine the resolution.

The electronics resolution was determined to be $\sigma_{2A}^{ENC} = 7.9 \pm 0.08\,\text{keV}$ and $\sigma_{CMS}^{ENC} = 12.0 \pm 0.03\,\text{keV}$. These values were measured at normal operating temperat-

ures without any additional cooling. Typical temperatures are around 50 °C for the SKIROC2-CMS and 43 °C for the SKIROC2A. These values are strongly influenced by the layout of the multi-layer PCB. The values for the resolution are close to the manufacturer's specifications (see table IV.1).

Further important investigations have been made addressing the behaviour of the SKIROC2A-ASIC at high input values, as mentioned in V.3. As by construction of the preamplification stage a non-linear behaviour was dedicatedly implemented to guarantee charge measurement up to 10 pC, this feature must be addressed in the ASICs calibration. The deviation from a linear behaviour in the low-gain energy branch can be seen in the non-calibrated plot shown in V.16a: The blue line corresponds to a spline fitted to the data, whereas the red line simply is a linear fit up to ADC channel 1000. The plot V.16b shows the situation after calibration and V.16c represents the remaining percentage-based deviation from a linear dependency. Dependent on the feedback capacitance setting of the preamplifier, this deviation always is better as 0.4%. The mean values as plotted have been fitted with an automated routine for all the 15 SCAs of a certain channel. For a full characterisation of the ASIC, each channel and each channel's SCAs need to be fitted for all possible preamp settings at both low- and high-gain branches. An automated routine is highly recommended as well as the use of the high-precision DACs of the on-board microcontroller on the GEAR platform.

Finally, the response of the SKIROC2A ASIC having a silicon detector connected to its inputs was measured in the laboratory (see figure V.17). The SKIROC2A-spectrum was measured with a PIN-diode manufactured by CiS embedding a shallow p^+-implant. The detector capacitance amounts roughly to 30 pF. An unprecedented energy resolution of only $FWHM = 26.9 \pm 0.3$ keV was measured in the bonded channel for the SKIROC2A. The ASIC's temperature was 18.3 °C. The feedback capacitance was set to 2.8 pF. The spread of the energy resolution among different SCAs was observed to be negligible.

For completeness, the spectrum of the SKIROC2-CMS was taken with the DSSSD detector which was used in the MLL experiment. The resolution for the SKIROC2-CMS was determined to $FWHM = 62.4 \pm 2.6$ keV, which - by the way - is better than any resolution yet measured with TREX. The dominating contribution to this resolution of the SKIROC2-CMS is the lack of any aperture in front of the DSSSD and the fact, that the setting of the feedback capacitances of the preamplifiers and the timing of the 'Singles'-mode have been optimised for the measurement of the elastic scattering in the MLL experiment. This value surely can be improved. Anyhow the energy information of the SKIROC2-CMS is a redundant information as the actual energy measurement will be done with the SKIROC2A ASICs in the HI-TREX setup.

The HIE-ISOLDE experiment showed nicely the urge for the upgrade of the TREX-setup: The electron-problematic, a missing physical segmentation and an insufficient energy resolution, limited the usability of TREX in conjunction with heavy, neutron-rich beams. In

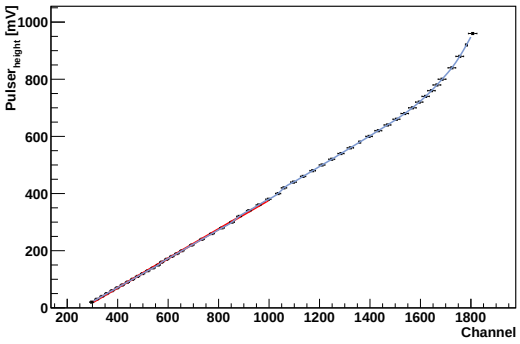

(a) Uncorrected spectrum showing the non-linearity.

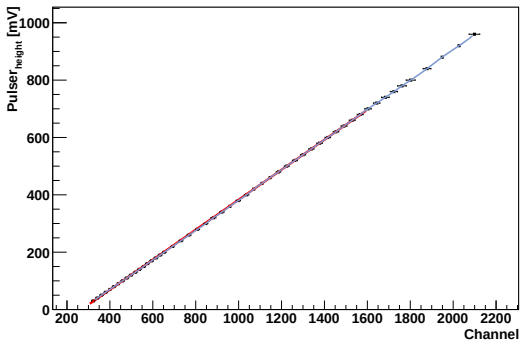

(b) Pulser signal corrected for the non-linearity.

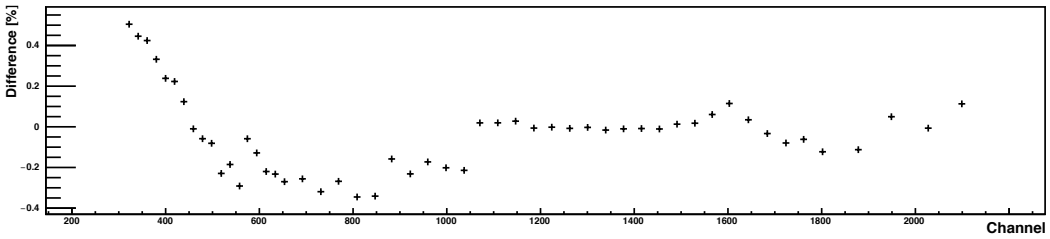

(c) Percentage-based deviation of the blue spline from the linear fit, shown in red in figure V.16b.

Figure V.16: Influence of the input voltage on the measured ADC channel in the SKIROC2A of the SCA *No*. 4 in the low-gain energy branch. The x-errors as shown in the upper two plots are multiplied by a factor of 10 for better visibility. The feedback capacitance was set to 2.6 pF.

the MLL experiment a few minor problems with the front-end PCB design were observed, which are addressed and understood. Otherwise a nicely working setup was tested and evaluated and the stability and application of the developed electronics in experiments with heavy-ion beams was proven. Finally, by exploiting PIN-diodes with shallow implantation in an experiment at the FRMII, valuable input to the manufacturer was given and the way towards the trapezoidal DSSSDs for the HI-TREX setup was laid out. It has to be mentioned, that the characterisation of the electronics developments in the laboratory revealed unprecedented values in terms of rate-capability, time- and energy-resolution.

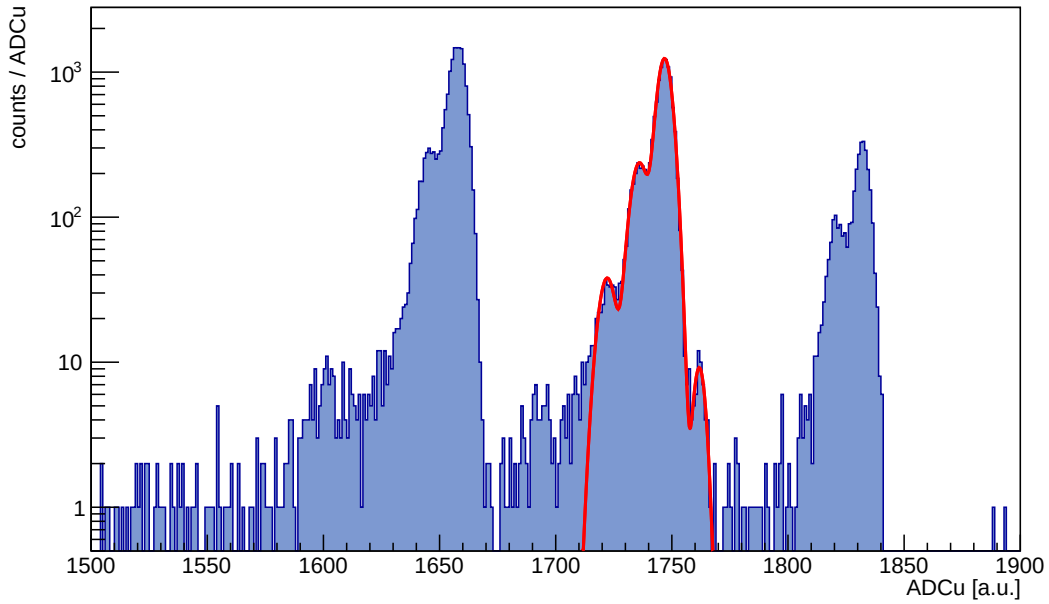

Figure V.17: SKIROC2A response at channel 58 and SCA *No*. 7 measured with a silicon PIN-diode. A fit to the four α-peaks from the ^{241}Am-decay is shown superimposed in red.

CHAPTER VI

Conclusion and further developments

VI.1 Summary and status

Experimental focus of this work was the execution and analysis of experiments with the silicon detector array TREX at the next-generation facility HIE-ISOLDE. A study of yet experimentally unknown, excited states in the isotope ^{135}Sn was proposed and accepted. The fully installed HIE-ISOLDE linac enabled energies of the ^{134}Sn-beam of 7.3 MeV/u. Thus, the one-neutron transfer experiment d(^{134}Sn, p)^{135}Sn in inverse kinematics was the first transfer experiment with such heavy, neutron-rich beams at CERN. Besides the lack of appropriate instrumentation to monitor the beam-composition at the accelerator side and the dysfunction of the primary target already after a short period of beam-time, important experience could be gathered for the technological development of the new HI-TREX setup. The switch to an alternate reaction with a stable ^{132}Xe beam revealed a unusually dominant transition in the prompt, doppler-corrected γ-ray spectrum, whose origin from the d(^{132}Xe, p)^{133}Xe reaction remains unclear. Further analysis, especially theoretical calculation are envisaged. Anyhow, the general feasibility of transfer reactions at HIE-ISOLDE with MINIBALL in conjunction with a segmented silicon array has been shown.

Further experimental investigations were closely related to the comprehensive technological developments, which were made for the new HI-TREX setup. HI-TREX is a highly integrated setup for transfer experiments at REX-HIE-ISOLDE and the upgraded successor of TREX. The main upgraded components feature two basic developments: The silicon detector upgrade and the accompanying custom made electronics. 70 µm thin, AC-coupled DSSSDs are a technological novelty and special effort has been put in the development of the ultra-thin, shallow p^+-implant layer, reducing energy straggling and enabling measurements of heavy ions even

at very low energies. Experiments at the FRMII helped to provide feedback for the sensor suppliers on the implantation parameters and proved the reliability of certain annealing methods. Finally, the complete readout-chain of the newly developed ASIC-based electronics has been successfully tested with a DSSSD in an elastic scattering experiment at the MLL with a high-intensity, heavy ion beam of ^{58}Ni at 110 MeV. The SKIROC2 ASICs showed a superior energy resolution of 26.9 keV FWHM and worked well in the vacuum under realistic conditions. The FPGA-based readout platform GEAR could also be tested for the first time in conjunction with the backend system TRB3 and proved excellent stability and capability.

Detailed, realistic GEANT4 simulations on the basis of the experiences gathered with TREX have been used to evaluate and specify the requirements for the new setup.

From the technological point of view, the enormous developments for HI-TREX enable the experimental tools to keep abreast with developing infrastructure and to push nuclear-(astro-)physics further to the limits. The developments are at the present technological limit in many aspects: Designing a highly segmented silicon array on basis of a vacuum-compatible, integrated, high-resolution electronics by means of ASIC-implementation is state-of-the-art in experimental nuclear and particle physics, as well as industrial applications. The generic ASIC readout platform GEAR is making use of the newest FPGAs available, embedding a high functional logic density while having a reduced power consumption and offering full flexibility for various types of experiments. The use of a high-density Hybrid-PCB with highly complex contours embeds bond-pads in inner layers of the PCB and enables the newly developed, thin DSSSD to be completely sunken into the PCB and be thus efficaciously protected. By mounting two unsegmented silicon detectors on the same PCB, a hitherto unparalleled compactness is guaranteed for the complete HI-TREX setup. Further pending developments, like the 3D-printed holding-structure and the testing of the rigid-flex PCB connections are detailed in the next section. The developments done for HI-TREX are generic developments for any experiments using silicon detectors to detect charged particles and thus guarantee a setup which will be compatible for long time in various future experiments.

A possible application of the setup would be feasible in the proposed operation of the TSR storage ring with reaccelerated ISOL beams at ISOLDE [38]. Despite the opportunities for nuclear astrophysics having cooled, stored radioactive ion beams, technological limitations like target-thickness effects and secondary electron contaminations can be addressed in a very elegant way. The developed DSSSDs are predestined by their thin entrance window for the application in storage rings and they can even be used as active vacuum barrier. Furthermore, the ASIC-based electronics is optimised such that an application in ultra-high vacuum without additional, external cooling is possible.

VI.2 Pending completion of kicked-off developments

The application of all the basic electronics developments for the HI-TREX setup has successfully been demonstrated in the heavy-ion experiment at the MLL and the reliability of the innovative sensor manufacturing has been proven in the FRMII experiment. Nevertheless, a few finalisations and some minor adaptions to the developments still need to be accomplished; part of which already have started.

To cope with the required leakage-current the ASICs need as input reference to their preamplification stage, two solutions have been worked out: Placing SMD-resistors on the bottom side of the PCB in conjunction with a stacked PCB, also hosting resistors due to space constraints, would enable a well-specified current between the preamplifiers $3V3$-supply and each input to the ASIC. Laboratory test have shown that from 100 MΩ to 10 GΩ every resistance value would be suitable. However, guaranteeing proper functionality and short recovery times from high charge input, 1 GΩ resistors are recommended. This requires a minimum package size of the SMD components of 0402, which results in the design of a stacked PCB, as too few PCB-space is available, or otherwise severe constraints on the number of channels which could be used of the SKIROC2A ASICs would be imposed. The second solution exploits the idea, that as the input channels of the ASIC are directly accessible on the back-side of the PCB, thus a passive silicon component integrating poly-silicon resistors could be fabricated. Consultations with the sensor supplier have evaluated the minimum space required to have 1 GΩ resistors processed. Feasibility was agreed on and an offer has been made. The advantages would be effectiveness in size and reliability as the component would be glued directly onto the PCB.

The sensor development has evolved steadily throughout this thesis. The thinning of large m embranes down to 70 µm succeeded and various implantation parameter have been tested and the layout of all necessary masks has been fixed. Yet, the fabrication of the whole detector batch still is pending due to some minor modifications in the implantation process and some testings of the wafer-handling and post-treatment processes.

Due to the thinness of the silicon-membranes, special attention has to be drawn to the mounting and connection procedures of the detectors with the Hybrid-PCB. A detailed plan for handling and mounting has been discussed with the sensor supplier, whose experts agreed on providing the assembly. Some promising pre-tests with thinned wafers showed the general feasibility of the procedures, but again, finalisations especially on the glueing and bonding process of the sensors to the PCB are upcoming. Furthermore, the E_{Rest} detectors need to be processed, tested and mounted simultaneously.

ASIC-wise, still a few features have not yet been evaluated., which could be useful for different experiments than the intended use of HI-TREX. Concerning the

SKIROC2A, the internal TDC - enabling the simultaneous measurement of the time down to 100 ps accuracy by forgoing either the high-, or the low-gain energy branch - is deactivated by the SlowControl at the moment, like is the Time-over-Threshold (ToT) measurement of the SKIROC2-CMS at high input signals. Especially the over-range behaviour of the ADC implemented in the SKIROC2-CMS and the automated switch to the ToT measurement needs to be investigated in close detail.

Accordingly, minor adaptions in the FPGA-firmware would allow for multiple DAQ-modes to be set via SlowControl. As well as the final integration of the whole setup surely would require some hand-shaking in the FW to be implemented concerning the external trigger- and/or clock synchronisation with the MINIBALL DAQ. A GUI to improve the usability of the system and the refinement of the analysis software can be well imagined.

An important test with good chances of success is the characterisation of the final silicon sensors together with the Hybrid-PCBs and the final auxiliary PCB components.

As detailed in the section describing the conceptual developments, the idea of using two additive manufacturing methods to comply with the necessary accuracy of the drawer-like 3D-printed mounting structure, principally has been shown. However, the mounting of e.g. a conical structure hosting protection foils, or apertures still needs to be implemented. Finally, the whole mounting procedure of the full setup needs to be cross-checked with some CAD-program and minor adaptions, like the final feedthrough design or the final rigid-flex PCB mounting are to be fabricated.

Last but no least, the reallocation of the beam-time of the d(^{134}Sn, p)^{135}Sn experiment was approved and hopefully the new setup will then be ready for future exciting physics campaigns.

APPENDIX A

Further DSSSD considerations

In this part of the appendix, some more layout-details concerning the double-sided Silicon-strip detector are presented. The layout of the pads for wire-bonding can be seen for the p-side in figure A.1 and for the n-side in figure A.2. AC-pads for wire-bonding can be found on the p-side on the left and right side, as for the n-side on the minor and major side respectively. DC-pads can be found on the p-side only on the right side and on the n-side only on the major side. The size of the AC-pads has been made large enough to be able to attach at least two bond-wires with standard diameter. Thick metallisation needs to be used on the junction-side as otherwise the shallow metallisation would be destroyed by the force induced by the bond-wedge. Additional p^+-implant is deposited underneath the bond-pads and biasing resistors in a deeper profile than along the remaining strip, which helps in terms of full-depletion of the detectors. The strips on the p-side are numbered in increasing order from the longest one on the major side, to the smallest one on the minor side. The bias-ring can be contacted by wire-bonding everywhere, although no shortening to the guard-ring structure consisting of 14 rings with different widths must be made. On the n-side no guard-ring structure is needed, as ground is contacted on this side. However openings of the overall n-side passivation are required to contact the strips and bias-ring. A second row of bond-pads was designed outside the active detector area due to possible constraints in the mounting procedure. The 32 strips of the n-side are numbered increasingly from the side where no p-side DC-pads are located to the side where the poly-Silicon resistors of the p-side are attached to the bias-ring. Fiducials having the shape of multiple crosses are located all along the detector edge on both sides for positioning and navigation under some microscope.

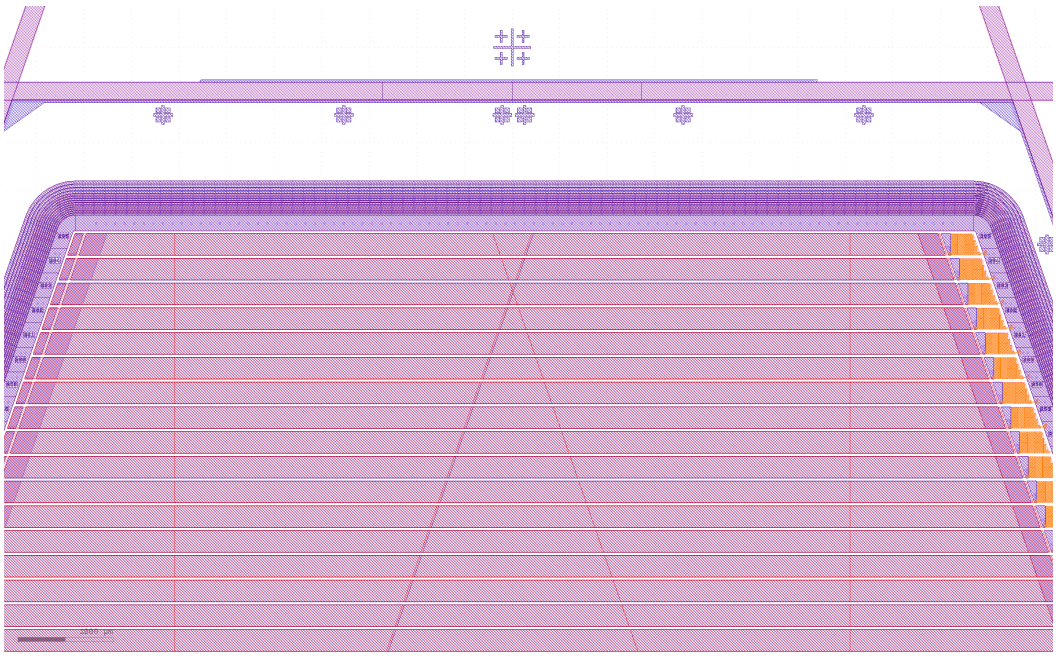

(a) Minor side of the trapezoid.

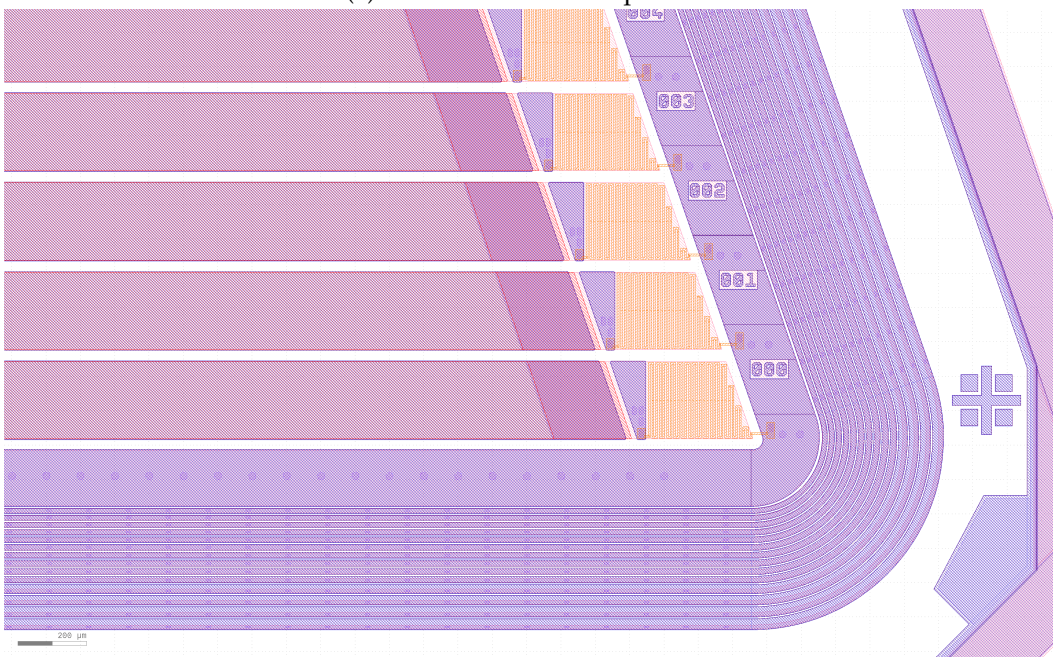

(b) Right corner of the major side of the trapezoid.

Figure A.1: Junction side of the DSSSD. Shown are the shallow p-implant strips (red), deep p-implants at the end of the strips (greyish), Poly-Silicon resistors (orange), metallisation thick (for bondpads, dark blue) and thin (for charge collection, light blue) and oxide openings (pink).

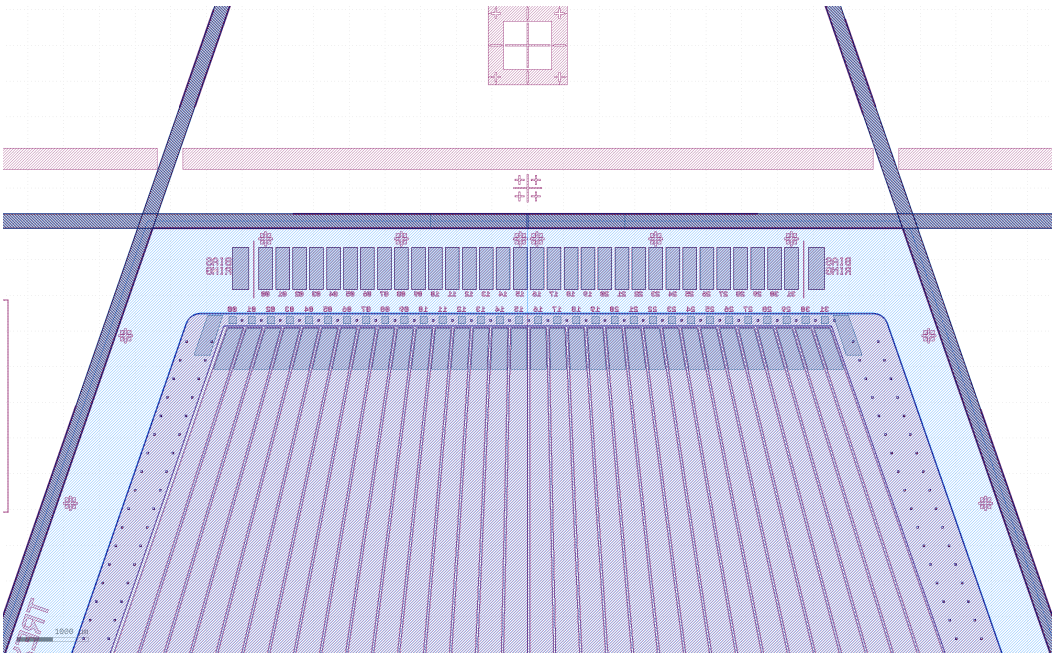

(a) Minor side of the trapezoid. Note the second row of bond-pads due to the mounting procedure.

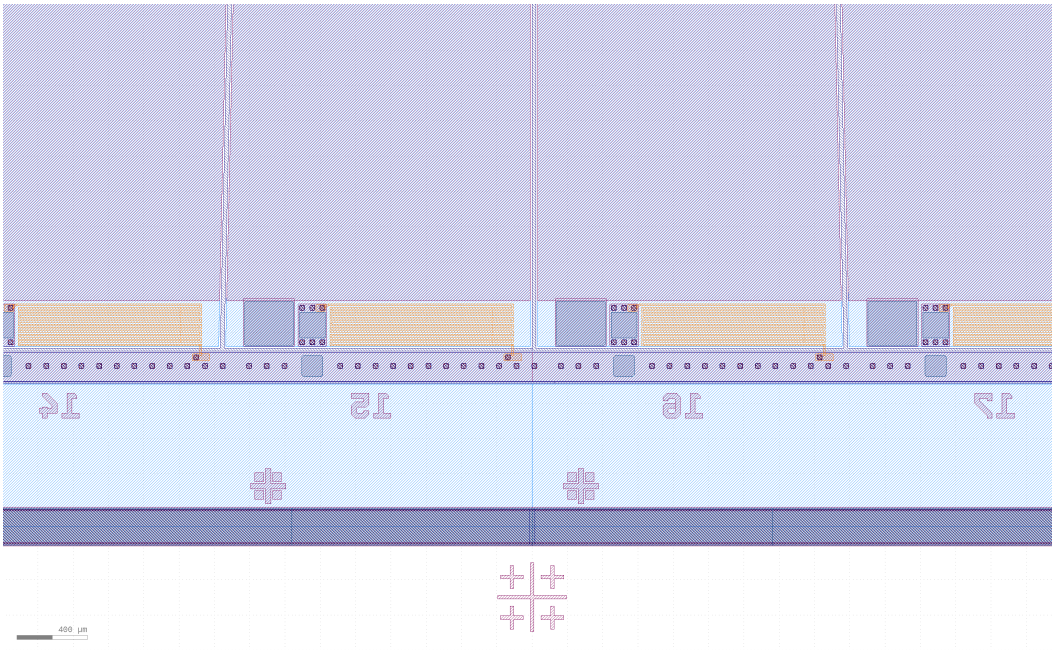

(b) Major side of the trapezoid. The biasing resistors are located here due to the larger pitch.

Figure A.2: Ohmic side of the DSSSD. Shown are the n^+-implant strips (ligth blue), Poly-Silicon resistors (orange), metallisation (purple), nitrid openings for moderated p-spray (dark blue) and passivation removal (violet).

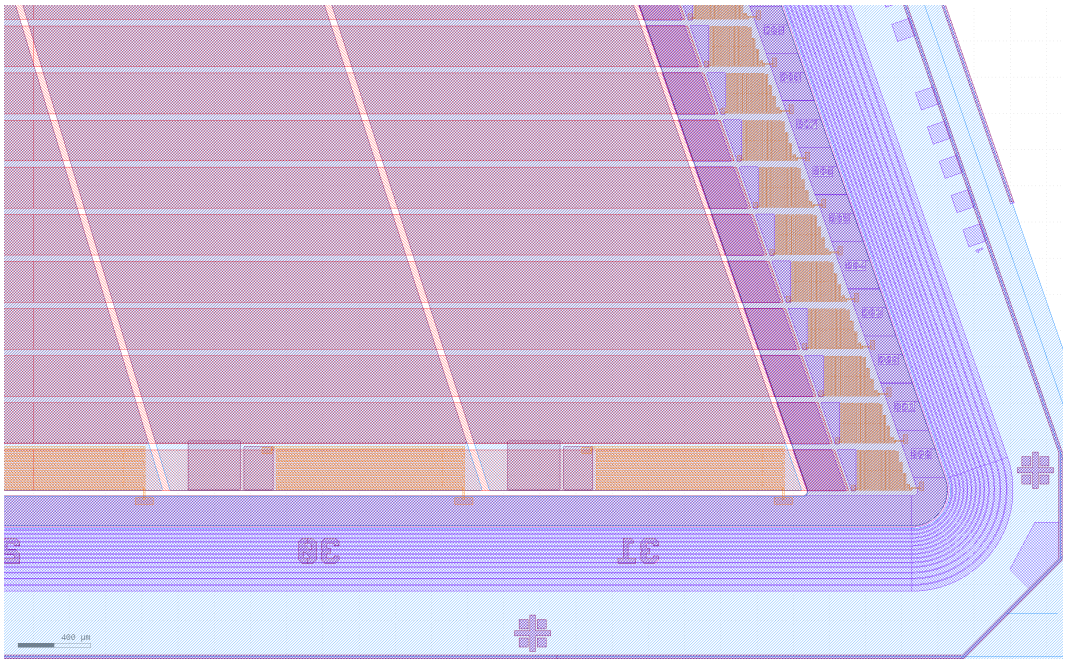

Figure A.3: Right corner on the major side of the trapezoid showing both, the n- and the p-side. Shown are the n^+-implants (light blue), n-side metallisation (purple), thick p-side metallisation (dark blue), shallow p-implant (red) and the biasing resistors on both sides (orange). Note the absence of n^+-implants underneath the p-side area without a well-defined shallow entrance window thickness. Fields for scratch marker can be seen on the right side of the detector.

APPENDIX B

Mounting and bonding procedure of the DSSSD: A proposal

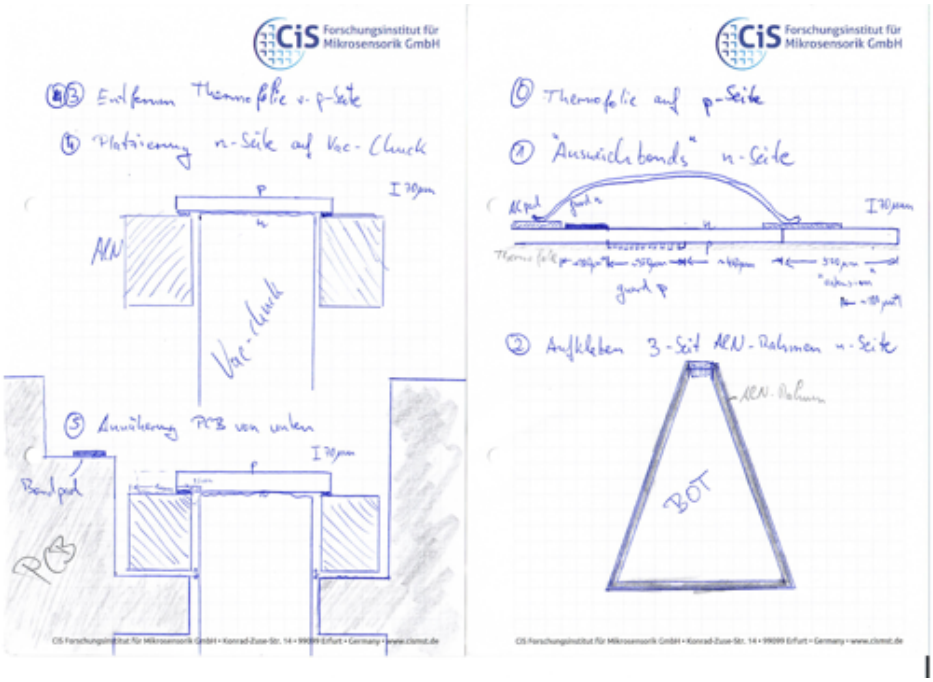

(a) Preparation of first n-side bonds, glueing of the detector to the mounting frame and placement inside the PCB millings.

Figure B.1: Proposed bonding and mounting procedure for the DSSSD. Approximate dimensions are given for each step described.

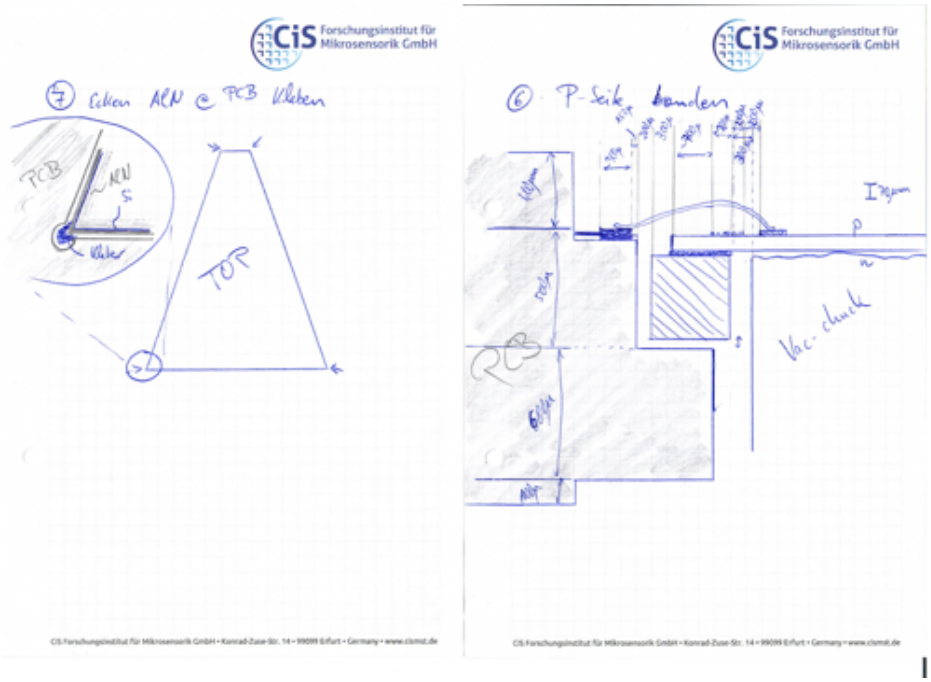

(b) Bonding of the p-side strips and glueing of the mounting frame elastically to the PCB to allow a certain range of motion in the event of thermal fluctuations.

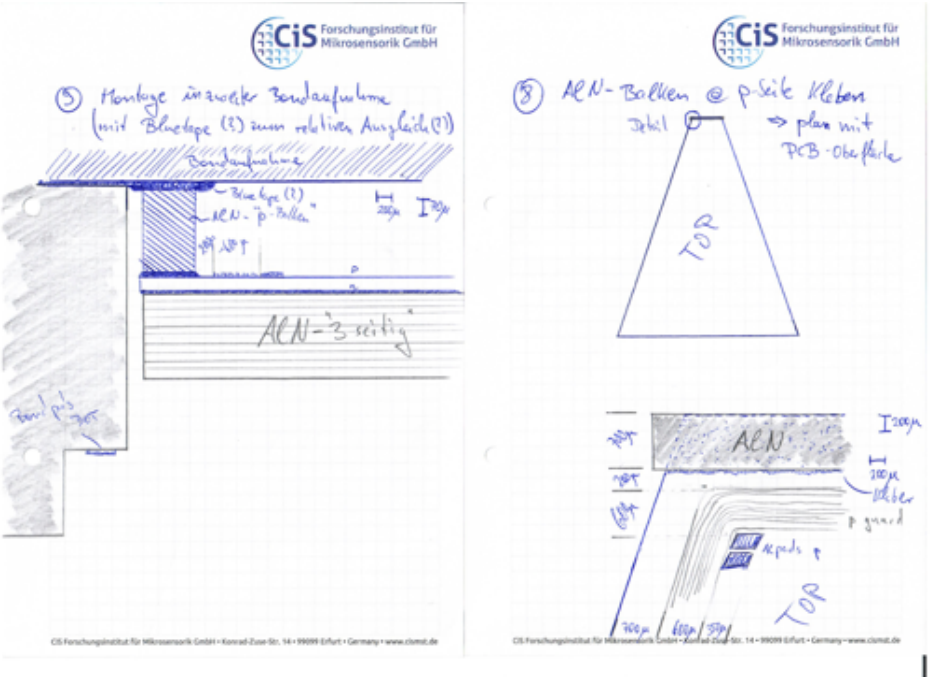

(c) Preparation of the support structure for the n-side bonding.

Figure B.1: Proposed bonding and mounting procedure for the DSSSD (cont.).

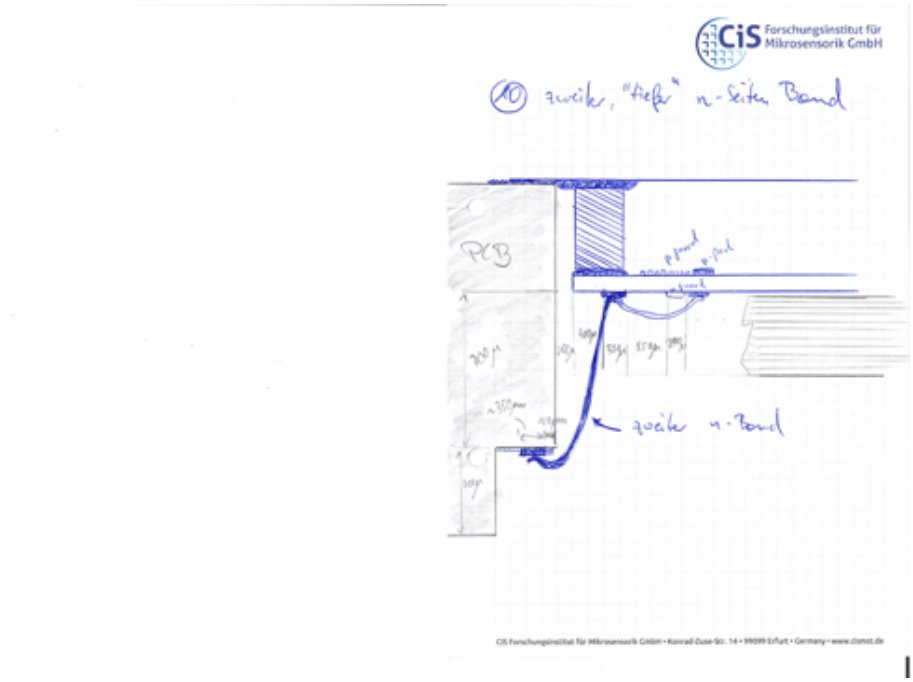

(d) n-side bonding to the milled bondpads in the inner-layer of the PCB.

Figure B.1: Proposed bonding and mounting procedure for the DSSSD (cont.).

APPENDIX C

Shortlisted ASICs

Please refer to the next page due to layout constraints.

Front-end-ASICs

Chip	IDE3465	IDE3466	VATA64HDR16	IDE1162	TA32CG3	IDE3160	VASCM3.2	VA32HDR14.2	VA32HDR14.3		MAROC3	SPIROC	SKIROC	MICROROC		APFEL1.4/1.5	AGET	ATHED	CASIS1.2A	HIDRA1	
Polarity	both (positive)	both (positive)	both	both	both ?	both (positive)	both	both (positive)	both(negative)		negative	positive (both ?)	both (from May on)	negative		both ?	both	both	both ?	similar to CASIS	
# of chn	_20	_36	_64	_32	_32	_32	_128	_32	_33		_64	_36	_64	_64		_2	_64	_16	_16	_27	
P/chn	?		<15 mW	?				3mW	3.4 mW			25µW (idle)	1.5 mW				<60 mW	<10 mW	30 mW	3 mW	
P total	<65 mW		<960 mW	55…66 mW	?	203 mW	?				220 mW		96 mW				< 120 mW	<640 mW	480 mW	48 mW ?	
analogue Buffer	no		no	no		no		no			no	yes, 16-depth	yes, 15 depth	no			no	yes (split analogue cell in 2)	no	no		
capacitive load	10pF - 30 pF		<300 pF	50 pF		220pF		20 pF				50 pF ??	50 pF	80 pF			300 pF				
Outputs	16 (HG) + 4 (LG) charge, 37 digital triggers		charge or time,trigger (OR)	32 CSA outs directly (-> TA32CG3), shaped amux	OR trigger and 32 in parrallel	multiplexed diff. current and common OR trig	serial multiplexer, integrated signals, correlated double sampling (CDS)	multiplexed and parallel output of each channel	same as 14.2		64 triggers, 1 AMUX 1 digital charge (12, 10 or 8 bit)	digital (12 bit Wilkinson), AMUX, trigger ?	digital (12 bit) and AMUX	digital, and 1 AMUX		shaped signal	multiplexed sampled analogue, trigger OR, designed for 12bit	multiplexer charge and time	correlated double sampling, amux out		
Output charge	multiplexed 20 pulse height samples serially		multiplexed 64 pulse height samples serially, voltage and diff. current		-						analogue or via 12 bit Wilkinson ADC	AMUX and digital (4 to 12 bit) + 2 gain = 14 bit energy				shaped signal	circular sampled buffer value, all chn or trig chn. or specific chn.,				
Output time	no		or multiplexed TAC	no	-	-		-			no	yes, 100 ps sigma (12bit TDC) and 12 bit BunchcrossingID	yes, 12 bit (200ns) gray counter from 64CR, and 12 bit TDC (100 ps)			no	no	yes			
Trigger-out	yes, OR, 37 digital, <100kcps/chn		yes, OR	no, but CSA-out	yes	yes, OR	?	--> TA32CG3! connection	same as 14.2		yes, 64 chn		yes, OR	?		no	hit channel register		?		
multiplexer speed	<50kcps/all channels readout (<--> 1 MHz ???)		<10 MHz	?	-	better < 500 kHz (noise)					5 MHz		5MHz??			-	25 MHz	2MHz	?		
Shaping-time	1µs & 250 ns parallel		50,100,150,300 ns	2 … 2.5 µs	..	1.8 … 2.3 µ s	?	2 µs	2 µs		50 … 150 ns	50 … 100 ns	300 ns			248 ns	50 ns … 1 µs (16 values)		1 µs		
multiple Range	yes, 2 (LG+HG(2))		yes, 2	no	-	no	yes, 1, 2.5, 6, 20 pC (+-)	no			yes, (preamp 8 bit (0 to 4))	yes, 2 gain (1&10) and preamp 8bit gain (0-5V) and 12 bit ADC	yes, dual (1 & 10) and 12bit ADC	LG, HG		dual (1 and 32)	yes 120 fC, 240 fC, 1 pC, 10 pC	yes , +- 10 MeV, +- 45 MeV, +- 225 MeV, +- 1GeV	yes		
Range 1	0.4 fC … 2.6 pC (+-)		-6,+7 pC	-1.5 pC … +1.5 pC	-	-5 pC … +13 pC		-2 … +13 pC	-20 pC … + 8 pC		0 … -3 pC up to 0 …-30 / -85 pC		2 fC … 8 pC	1 fC … 1 pC		1 fC … 6.3 pC	1 pC / ENC=0.5 fC/ 12 keV	20 keV	2.7 pC		
ENC 1	0.35fC / 9 keV		1 fC/ 22.5 keV	0.4 fC / 10 keV	-	0.7 fC/14 keV		0.5 fC / 11 keV	1 fC / 22 keV		> 2 fC / 50 keV		0.4fC / 10 keV	0.4 fC / 10 keV		0.7 fC / 15 keV	0.1 fC / 3 keV @ 120 fC range		0.4 fC / 10 keV		
Range 2	100fC … 26 pC (40pC) (+-)		-20,+55 pC	-	-				-								10 pC		52 pC		
ENC 2	4.2 fC / 94.5 keV		8fC / 180 keV	-	-				-							0.7 fC *32: ???	5 fC / 120 keV		?		
Threshold-DAC	8-bit		externally, global	-	3-bit							10 bit global	10 bit common			10 bit	8bit global	yes	?		
trim DAC/chn	different HG thresholds		4-bit	-								4bit fine	4 bit fine				4 bit fine		?		
min trig threshold	1.1/11 fC (HG), 150 fC(LG)		tbd	-		21 fC / 460 keV					5 fC / 100 keV	50 fC / 1 MeV	0.4 fC / 10 keV				> like noise (0.1 fC / 3 keV @ 120 fC range)	200/300 keV	?		
Trigger shaping	250 ns		50 ns	-	75 ns … 150 ns						20 … 25 ns	15 ns	30 … 120 ns				?		?		
readout	all chn ph/fixed chn waveform, triggers		all chn ph/fixed chn waveform	CSA (direct) or AMUX from shaper	-			AMUX & parallel	same as 14.2		all outs						peripherial boards (CoBo, MutantASAD,…)	multiplexed			
supply voltage	-2V, +1.5V, +3.3V and +400µA mbias		+2.5 V, -2.5 V	-2V, +1.5 V	?	-2.5 V, +2.5 V		?	?		+3.5 V, +2.5 V, ???, 0…3.5 V	5V, 3.5 V					count rate < 1kHz				
Config Register	356-bit		873-bit	?		186- bit		?	?		829 Slow Control	Slow Control (712) and Probe (912)					surely		3.3 V		
what	DAC, trig mask, shaping time, …		trig thr, input load, delay, …	-							different parameters						yes				
programming	serial Interface		serial interface, clock, bonding,	-							serially						SPI				
pitch size	?		140µm/200µm	-													0.6 mm				
size	7.14x6.045 mm^2		9.81x6.50 mm^2	?							4.0 x 3.9 mm^2	4.2 x 7.2 mm^2	7.1 x 8.5 mm^2			3.3 x 3.4 mm^2	8.7 x 7.7 mm^2		3.1 x3.1 mm^2		
operating temp	+25 °C		+20°C	?												-20°C		6°C			
availability	immediately		immediately								immediately?										
Price	?		730 €/ die								?										
Company	IDEAS, Norway	IDEAS, Norway	IDEAS, Norway	IDEAS, Norway	IDEAS, Norway	IDEAS, Norway	IDEAS, Norway	IDEAS, Norway	IDEAS, Norway		Omega MicroElectr	Omega MicroElectr	Omega MicroElectr	Omega MicroElectr		Panda	CEA Saclay	Musette	Space		
Specialities	radiation hardened, double dual range, SEL> 100 MeV/mg/cm2), gain decrease 0.2%/°C, saturation LG 40-50 pC!!!	SIMILAR TO 3465 but with gray-counter (counts coincidences in hits) and SPI	external bias,config register, test input	output of CSA directly to e.g triggering chip, external bias generation possible			CDS, two alternating S+H					IDLE-mode! , backup S&H, ADC converts 36 analogue values in 1 run (100 µs), max 32 runs if SCA is full, readout up to 256 ASICS in one chain	Labview TestBoard,	similar to SKIROC			350 kHz rate possible	PZC, split 512 cells to two buffers, sampling with 1 … 100 MHz (stopped externally), possbypass of CSA, !!! FIXED PatternNoise !!!, designed for 12bit external ADC, clock distributor, …	predecessor of AGET?	automatic gain selection		
Designed for	Silicon readout		SiPM, MPPCs (Multi Pixel Photon Counters)	Si-Wire readout		PMTs @ Scintillators	TFT, Silicon		MA-PMTs		Hamamatsu PMTs	SiPM Scintillating fibres	Silicon PIN Diodes			Si-readou	TPCs	Si-Strip readout	Space		
Experiment	Space (JUICE/ RADEM, EDRS-C)		???	MONICA (Space)	ISS-CREAM						ATLAS luminometer	HCAL CMS	ECAL ILC			Panda	CERN, Samurai, GANIL, NSCL	MUSETTE/VAMOS	PAMELA		
Pros	radiatio																				
Cons			in development/ improvement																		

APPENDIX D

Data structure of the ASICs

Please refer to the next page due to layout constraints.

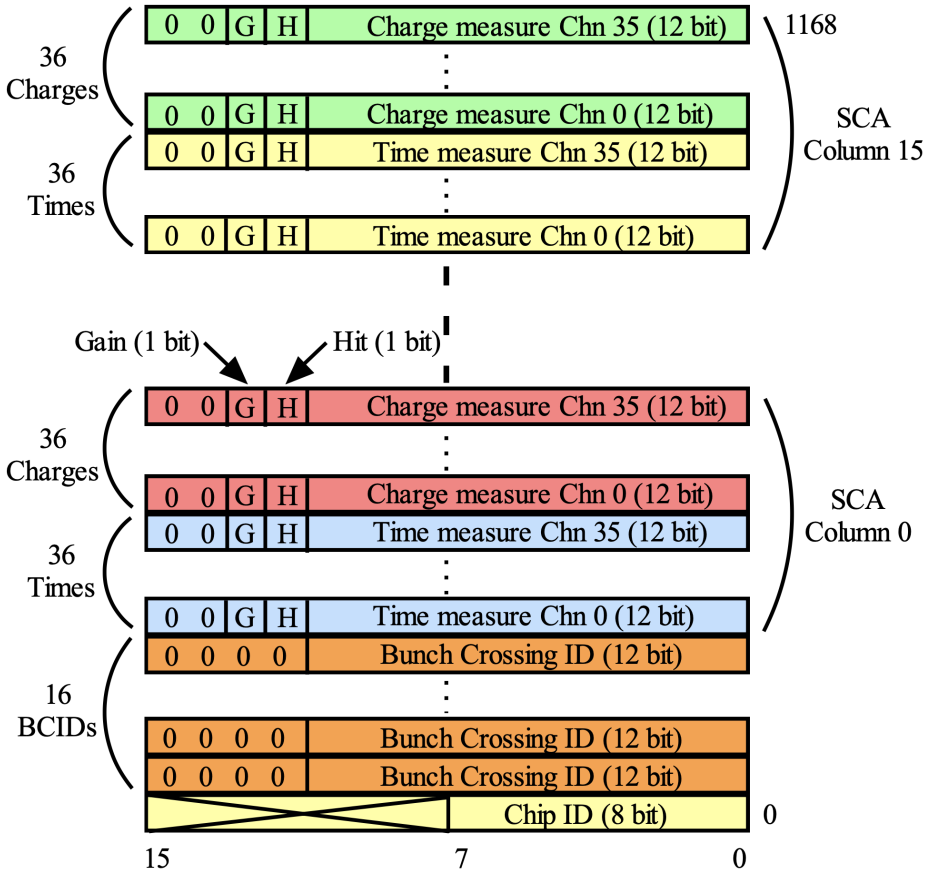

Figure D.1: Memory mapping of the SKIROC-2A. Readout is MSB first and high address first. BCID is gray-encoded. ADC data are 12 bits gray. It can be decided via SlowControl settings if the TDC-time or the second branch of the slow shaper (high gain, or respectively low gain; indicated by the gain bit) are converted and read-out [28].

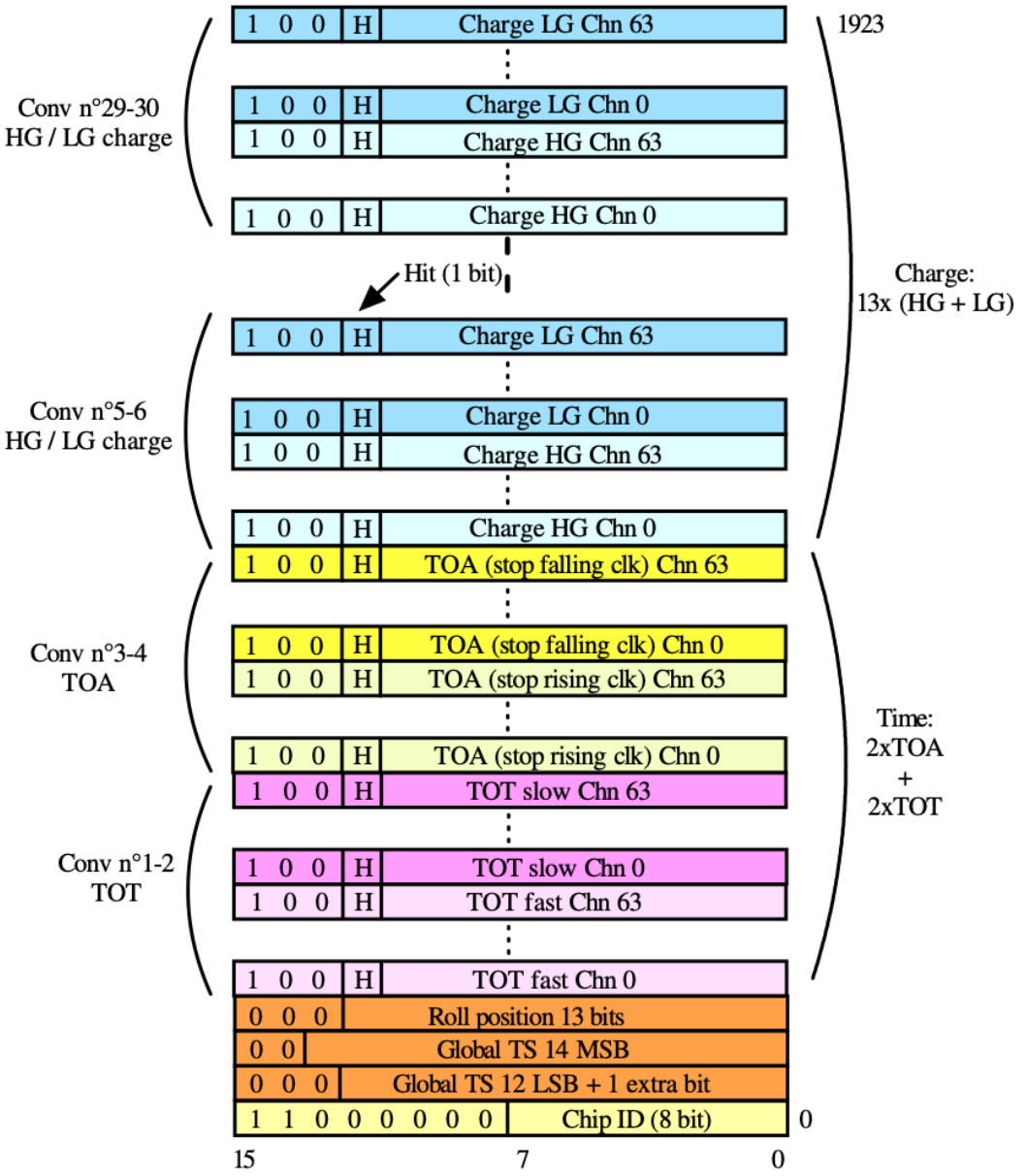

Figure D.2: Memory mapping of the SKIROC2-CMS. Readout is MSB first and high address first. Global time-stamp is gray-encoded. Extra bit is LSB counter on falling edge (binary decoded). ADC data are 12 bits gray. Conversion order is TOT/TOA/Q. First conversion is "TOT fast" with FlagTDC @ '1' [21].

APPENDIX E

Details on the Hybrid-PCB

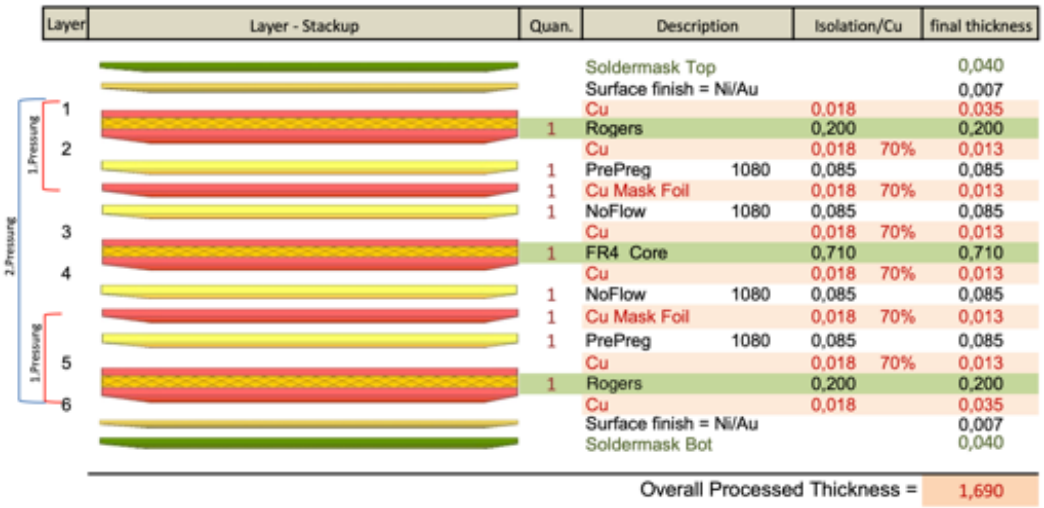

Figure E.1: Layer stackup of the Hybrid-PCB. This is a 6 layer PCB processed in a panel of 2 single PCBs. Materials are FR4 TG170 and Rogers RO4003. Copper thickness is 18 µm on inner and outer layers.

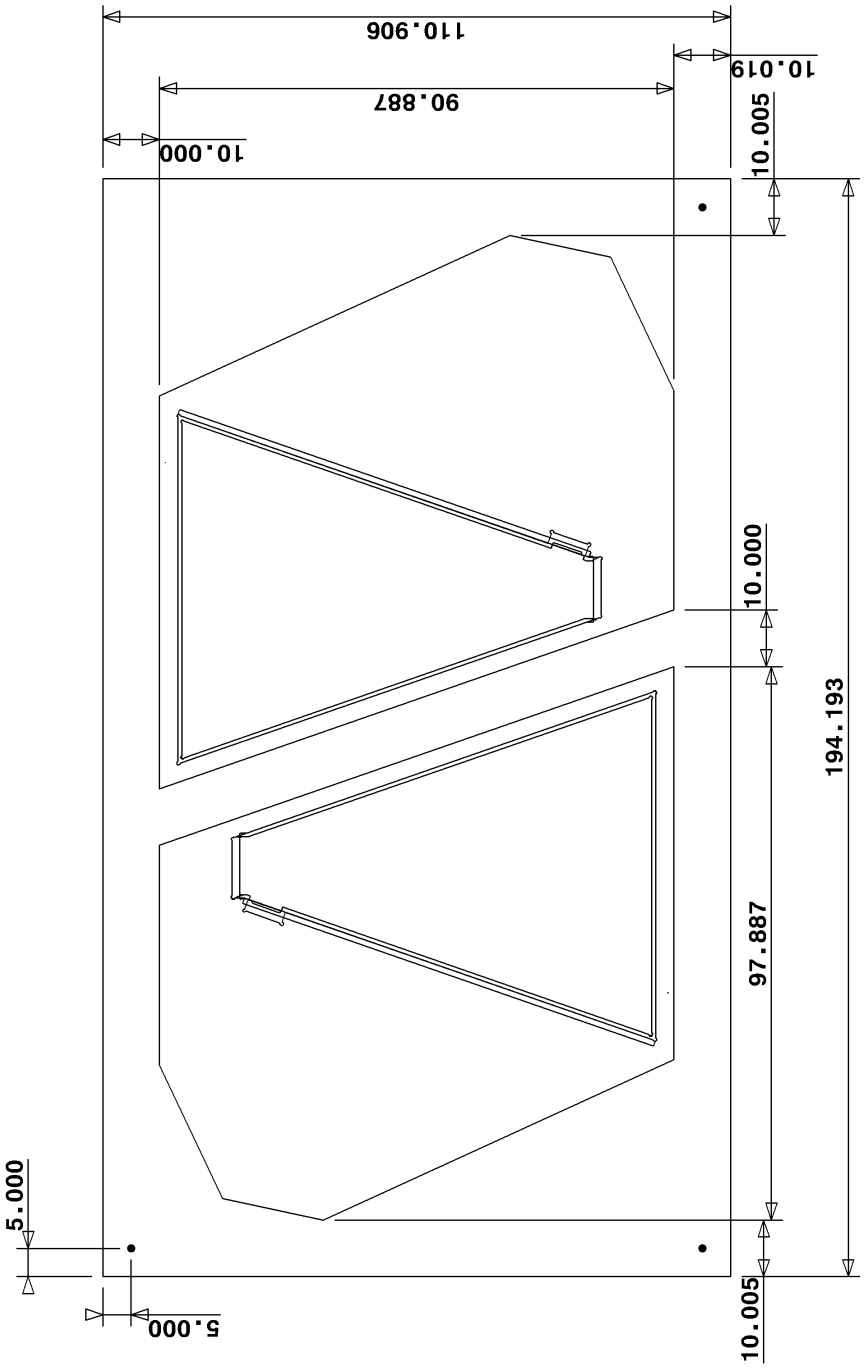

Figure E.2: Dimension and layout of the panel hosting two Hybrid PCBs. The reason to manufacture the PCB as a panel is due to the need during component assembly to have a rectangular outline for automated placement and soldering. All dimensions are given in mm.

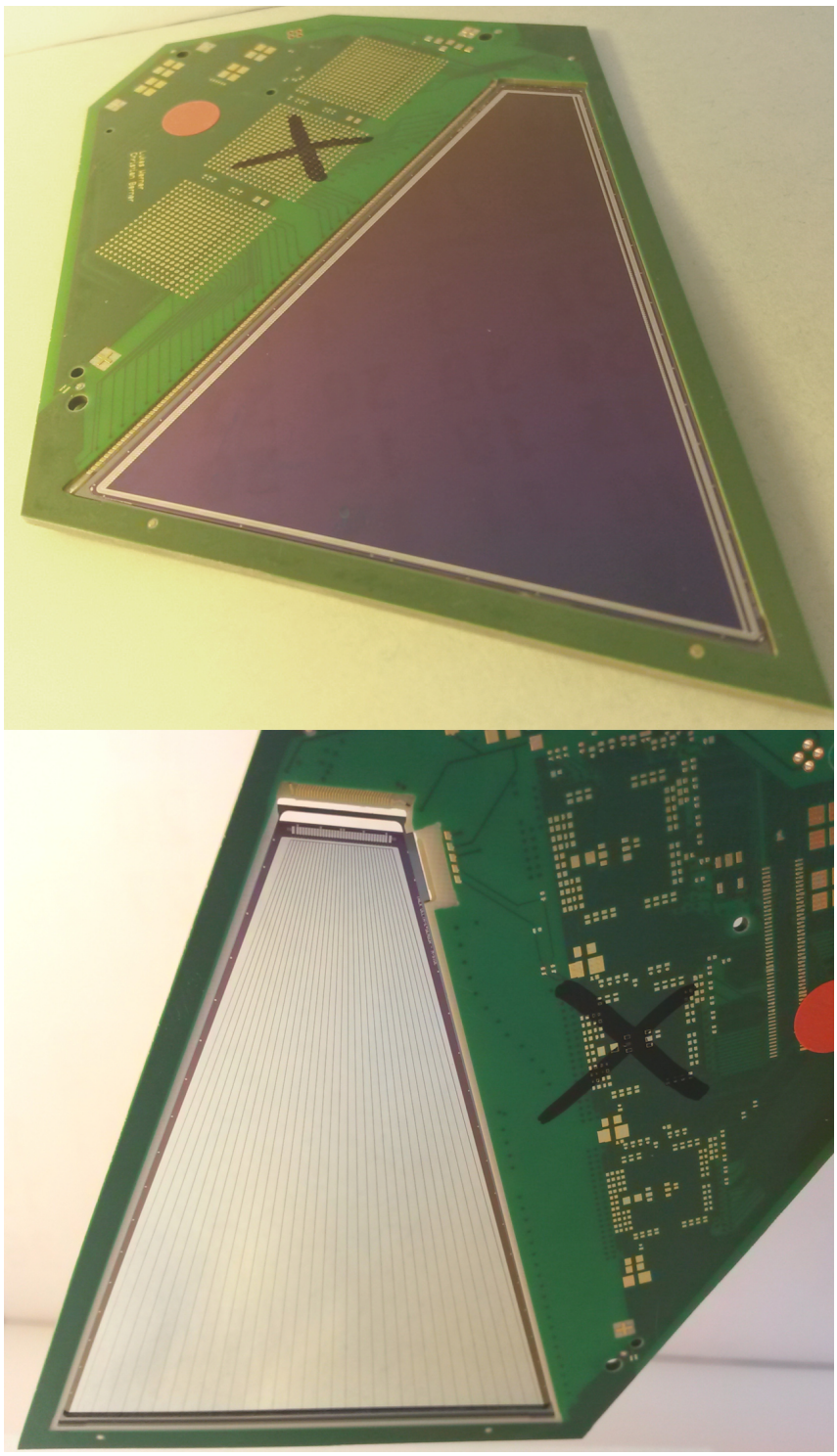

Figure E.3: Dummy DSSSD fitted into the Hybrid PCB.

APPENDIX F

Results CERN

F.1 d(^{134}Sn, p)^{135}Sn

Although the statistics is pretty low, a correlation in the time-distribution between the particles and the γ-rays can be seen in figure F.1a. The corresponding prompt, Doppler-corrected energy spectra of the γ-rays are displayed in F.1b.

It was concluded, that the peak of 197 keV is due to inelastic excitation of ^{155}Gd, as the Doppler-correction for this isotope resulted in the sharpest prompt peak with maximum statistics. The particle distribution gated on the prompt γ-peak can be seen in figure F.1c.

F.2 d(^{132}Sn, p)^{133}Sn

The prompt, Doppler-corrected spectra can be seen in the plot F.2. The dominant contributions originate from ^{166}Yb: The $6^+ \rightarrow 4^+ \rightarrow 2^+ \rightarrow 0^+$ transitions together with both prompt characteristic X-rays K_α and K_β can be nicely seen. A cut on these prompt γ-lines shows a distribution of particles located predominantly within the bands of elastically scattered target particles. The corresponding $E - \theta$ plots can be seen in the appendix in F. The $E - \theta$ plot shown in F.3 presents the whole statistics acquired during the d(^{132}Sn, p)^{133}Sn experiment. In the backward barrel only the left and bottom quadrant are shown as the other two barrel detectors suffer from a too bad resolution and pickup noise. In the forward region, the energy straggling in the target, as well as the Mylar foils covering the barrel detectors and the energy resolution of the detectors are taken into account when calculating the $E - \theta$ splines. The back-bending bands indicate the location of punch-through particles. In the backward barrel, only the influence of the target was taken into

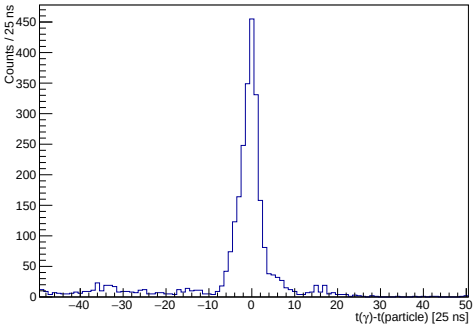

(a) Time difference between the particles, measured in TREX and the detected γ-rays in MINIBALL.

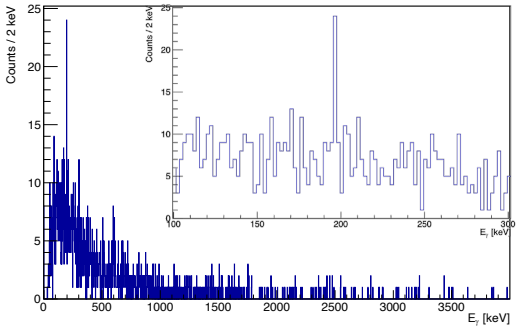

(b) Doppler-corrected γ-ray spectrum gated on prompt particle-γ coincidences (within 100 ns time difference).

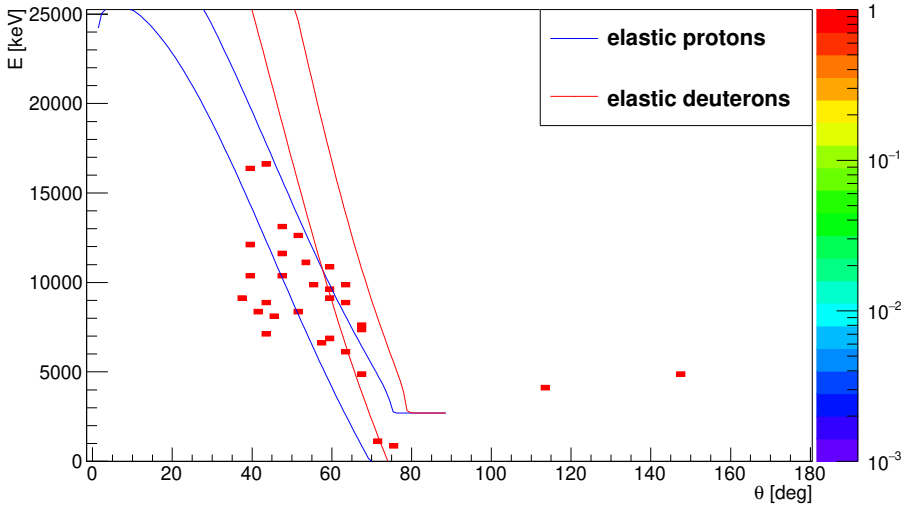

(c) Distribution of detected particles in coincidence with the prompt $E^{\gamma} = 197\,\text{keV}$ line. The lines indicate the location of elastically scattered protons and deuterons assuming a ^{155}Gd beam.

Figure F.1: ^{135}Sn experiment.

account. All reactions are assumed to happen in the middle of the target. The $E - \theta$ splines show the location of elastically scattered target particles, as well as the location of protons due to the transfer reactions to the ground state and a 3.0 MeV excited state in ^{133}Sb. Additionally the transfer to the ground state in ^{133}Sn is indicated, however due to the much smaller Q-value of this transfer reaction, the energies are somewhat smaller and possible contribution in the particle distribution from ^{133}Sn states lacks of sufficient statistics.

The particle discrimination between protons and deuterons followed a two-step

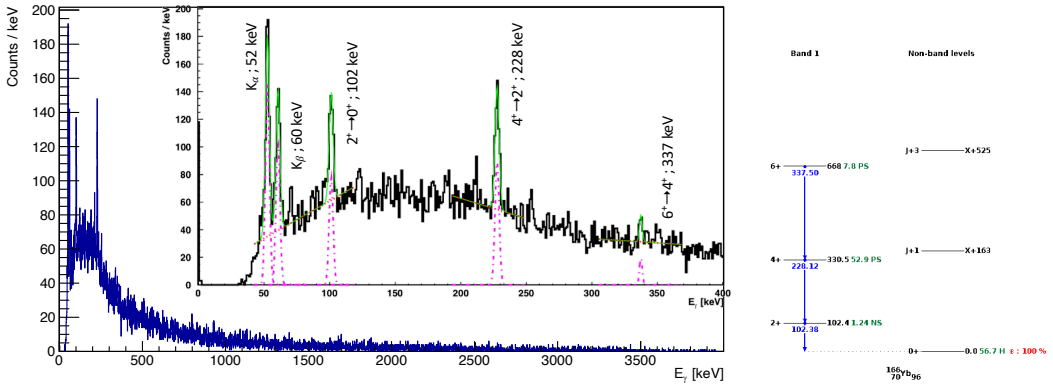

(a) Doppler-corrected γ-ray spectrum gated on prompt particle-γ coincidences (within 100 ns time difference).

(b) Level scheme of ^{166}Yb taken from [29].

Figure F.2: Prompt γ-ray spectrum of the ^{133}Sn experiment dominated by the beam contamination ^{166}Yb.

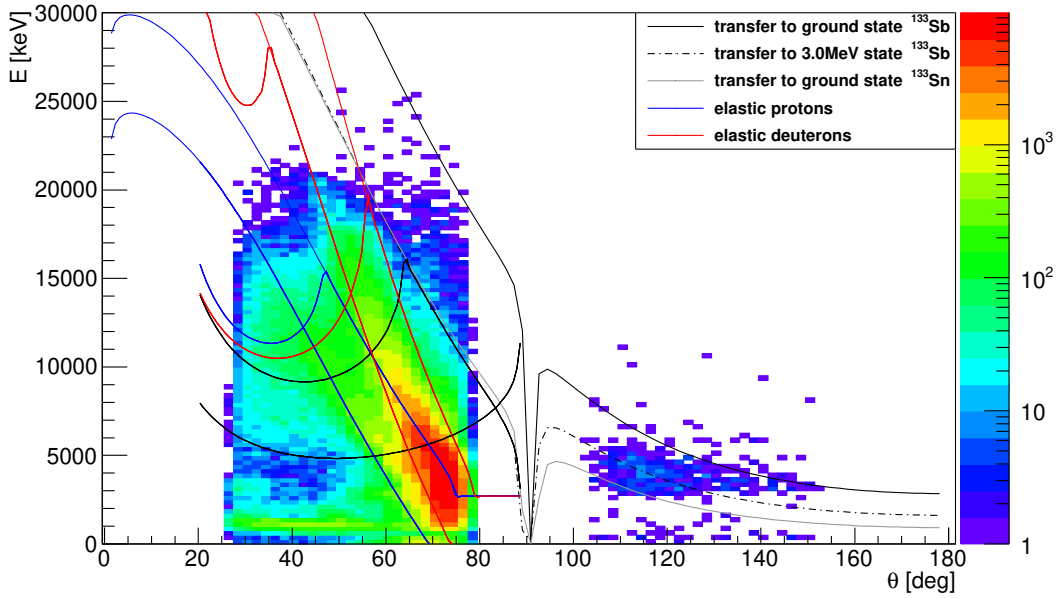

Figure F.3: Energy-vs-θ plot showing the energy and angular distribution of particles measured with the TREX barrel detectors.The lines indicate the location of elastically scattered target particles, as well as the location of protons from transfer reactions.

method: First, all particles are sorted by their characteristic energy loss in the ΔE-E detector setup. This is possible even in backward direction until $\theta_{lab} \approx 115°$. Second,

for unidentified particles punching through both detectors in the forward region, the $E - \theta$ splines are used for further discrimination. In backward direction, all particles stopped in the ΔE detector are considered as protons.

The identified protons are used to produce the spectra shown in figure F.4. The excitation spectrum of these protons can be seen in F.4c. It barely shows any pronounced structure due to the lack of energy resolution. The distribution is gaussian-like with a mean at 2267 ± 88 keV. For comparison, the mean of the excitation energy distribution of the elastically scattered deuterons as shown in F.4b is symmetrically centered around 43 keV. Hence, all the various assumptions for the energy reconstruction of the particles seem to be consistent. The γ-ray spectrum in coincidence with the protons is presented in F.4a.

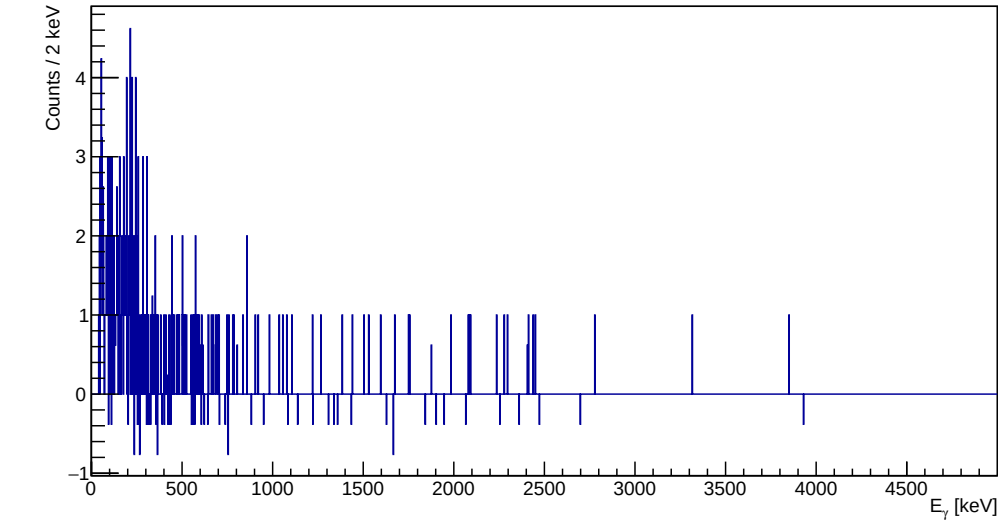

(a) Coincident γ-spectrum, gated on protons in the backward barrel.

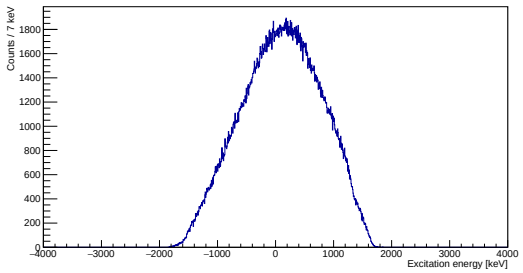

(b) Excitation energy of elastically scattered deuterons to cross-check the settings.

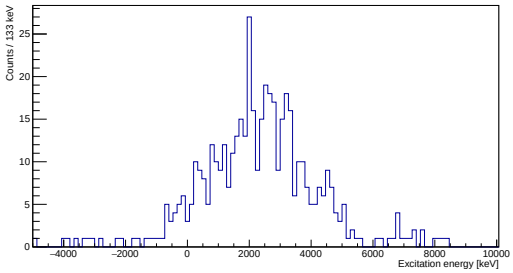

(c) Excitation energy of the protons identified in the backward barrel.

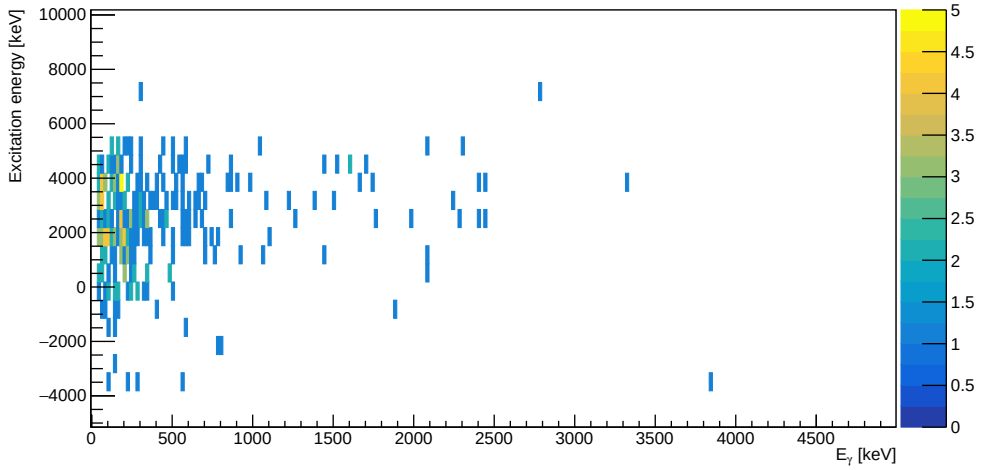

(d) Excitation energy versus Doppler-corrected γ-energy.

Figure F.4: Pattern of the transfer reaction d(^{132}Sb, p)^{133}Sb.

The spectrum is Doppler-corrected and background subtracted by taking random coincidences outside the prompt time-difference peak, normalising them to the coincidence interval and subtracting these events from the prompt spectrum, resulting in sometimes non-integer and even negative values. No real peak-like structure can be extracted because of missing statistics. Same situation applies for the correlation spectrum of the excitation energy dependent on the measured γ-ray energy.

Despite the beam contamination with ^{166}Yb and ^{132}Sb, transfer reactions to ^{133}Sb were identified in the backward barrel. It was the primary target, which broke after a very short time and prevented taking more statistics.

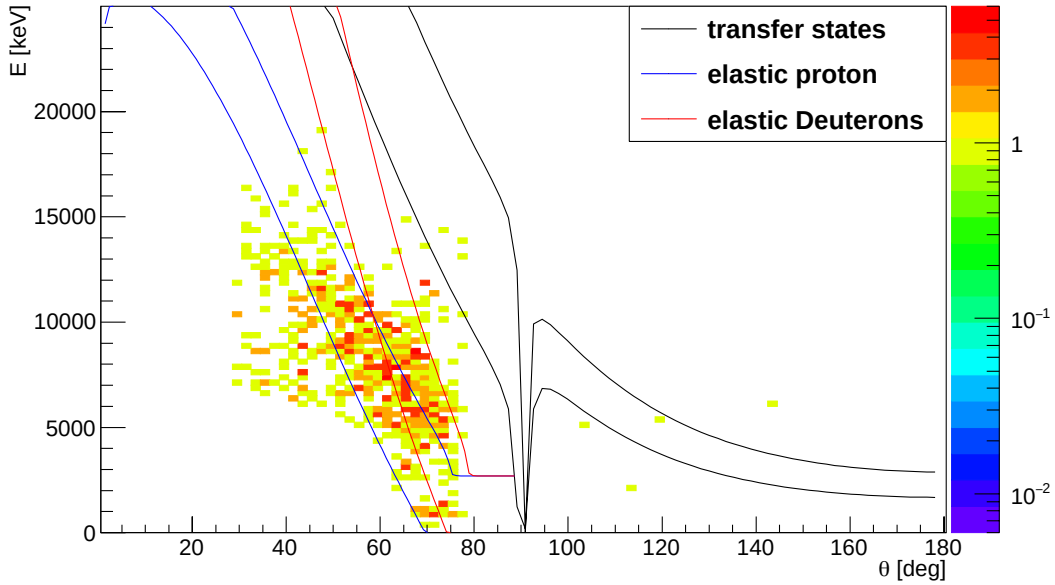

Figure F.5: Energy-vs-θ plot showing the energy and angular distribution of particles measured with the TREX barrel detectors when cutting on the prompt 228 keVγ-ray. The lines indicate the location of elastically scattered target particles, as well as the location of protons from transfer reactions to the ground state and a 3.0 MeV excited state in ^{133}Sb. In the forward direction, energy resolution is taken into account, as well as the Mylar-foil covering the forward barrel. In backward direction, only the energy loss in the target is taken into account. It was assumed that the reactions happen in the middle of the target.

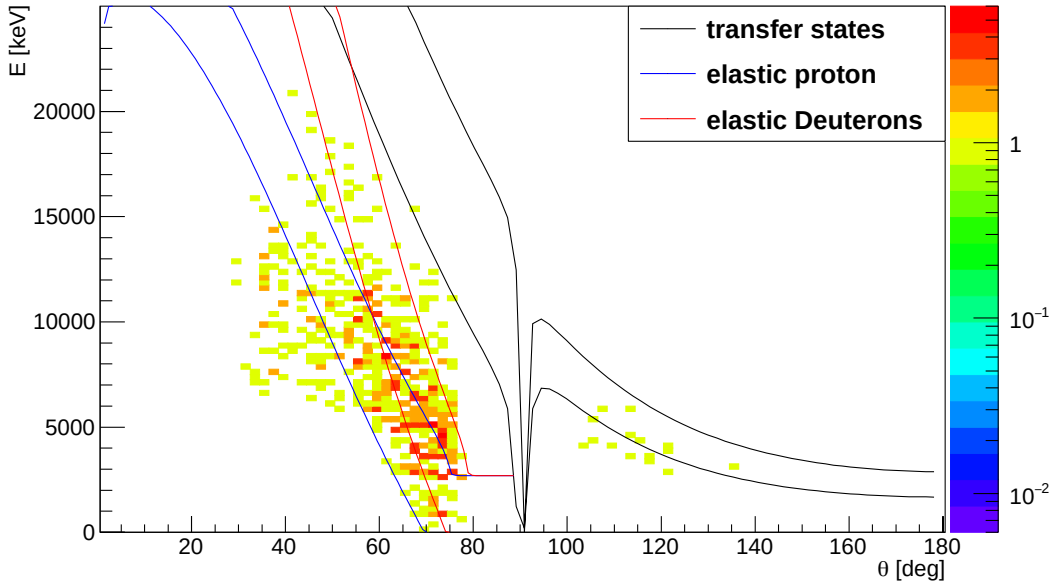

Figure F.6: Energy-vs-θ plot showing the energy and angular distribution of particles measured with the TREX barrel detectors when cutting on the prompt 102 keVγ-ray. The lines indicate the location of elastically scattered target particles, as well as the location of protons from transfer reactions to the ground state and a 3.0 MeV excited state in ^{133}Sb. In the forward direction, energy resolution is taken into account, as well as the Mylar-foil covering the forward barrel. In backward direction, only the energy loss in the target is taken into account. It was assumed that the reactions happen in the middle of the target.

F.3 d(^{132}Xe, p)^{133}Xe

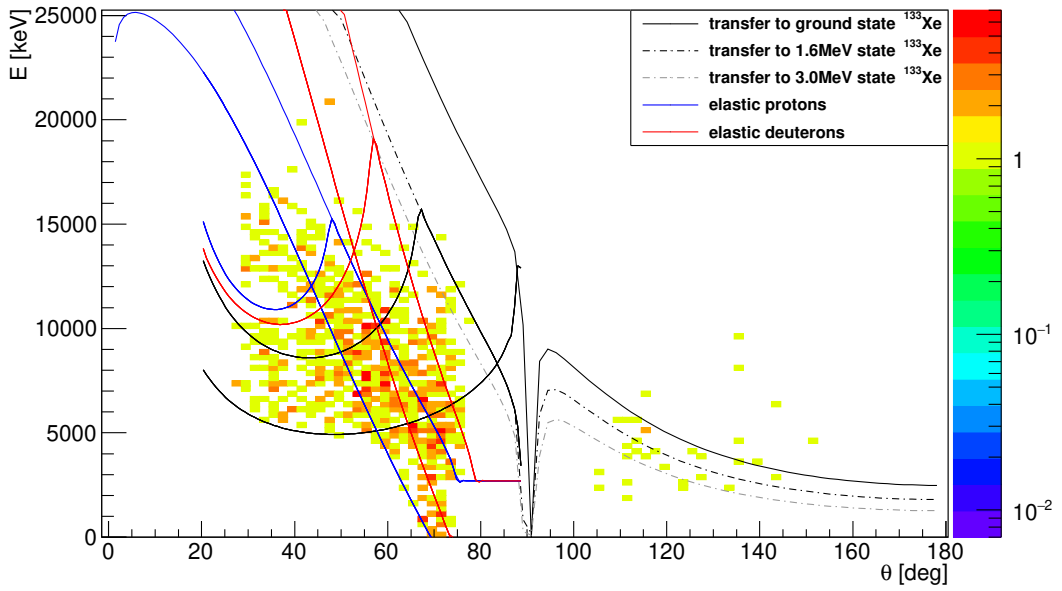

Figure F.7: Energy-vs-θ plot showing the energy and angular distribution of particles measured with the TREX barrel detectors when cutting on the prompt 125 keVγ-ray of the reaction d(^{132}Xe, p)^{133}Xe at 7.2 MeV/u beam energy. The lines indicate the location of elastically scattered target particles, as well as the location of protons from transfer reactions to the ground state, a 1.6 MeV state and a 3.0 MeV excited state in ^{133}Xe. In the forward direction, energy resolution is taken into account, as well as the Mylar-foil covering the forward barrel. In backward direction, only the energy loss in the target is taken into account. It was assumed that the reactions happen in the middle of the target.

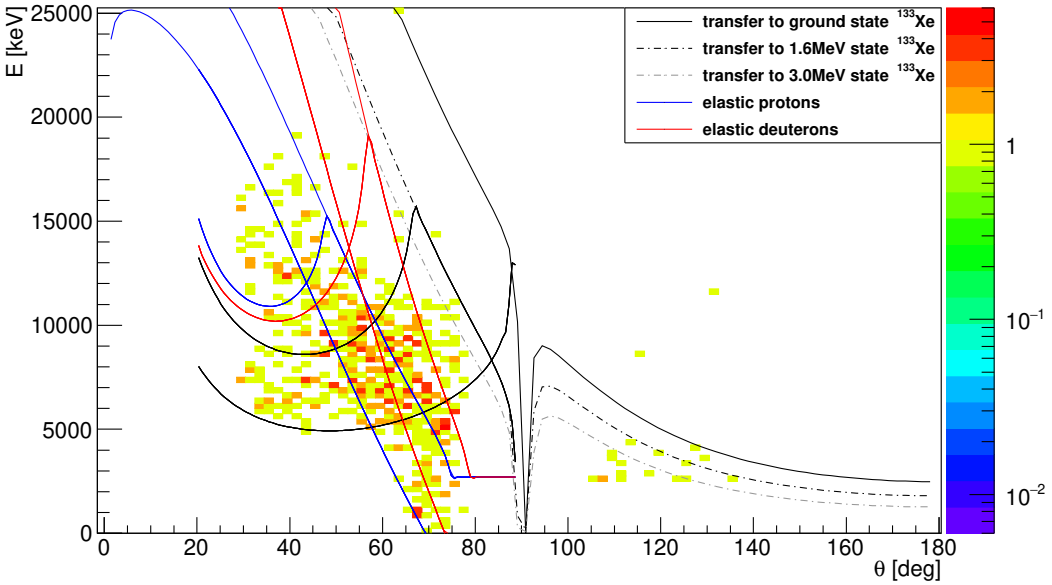

Figure F.8: Energy-vs-θ plot showing the energy and angular distribution of particles measured with the TREX barrel detectors when cutting on the prompt 564 keVγ-ray of the reaction d(^{132}Xe, p)^{133}Xe at 7.2 MeV/u beam energy. The lines indicate the location of elastically scattered target particles, as well as the location of protons from transfer reactions to the ground state, a 1.6 MeV state and a 3.0 MeV excited state in ^{133}Xe. In the forward direction, energy resolution is taken into account, as well as the Mylar-foil covering the forward barrel. In backward direction, only the energy loss in the target is taken into account. It was assumed that the reactions happen in the middle of the target.

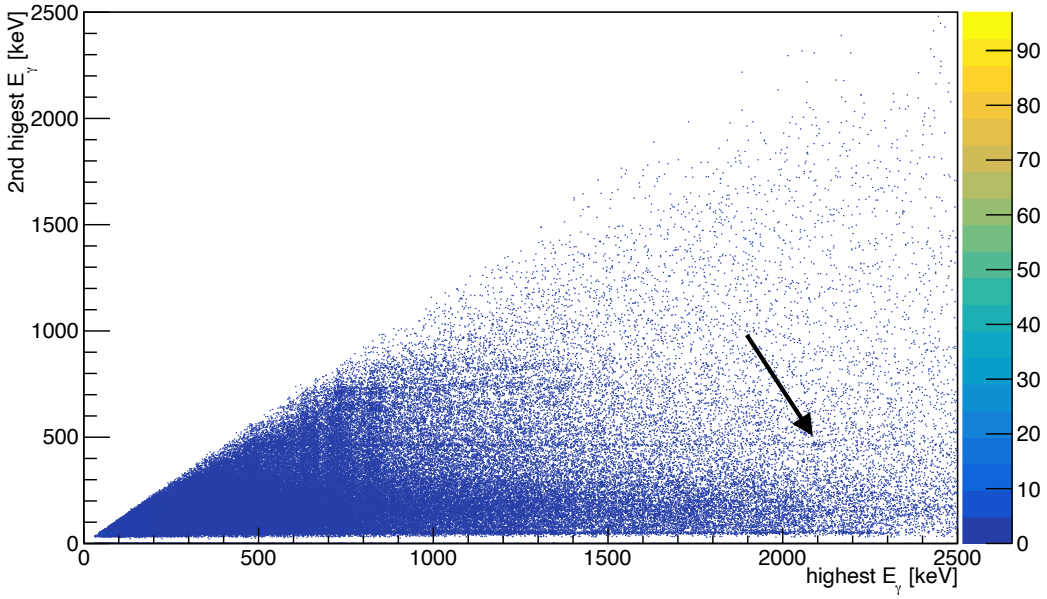

Figure F.9: $\gamma\gamma$-coincidence spectrum of MINIBALL. The most energetic γ-ray and the second highest one were selected. Events with higher multiplicity are discarded. The arrow is marking a possible coincidence of the 463.2 keV γ-ray.

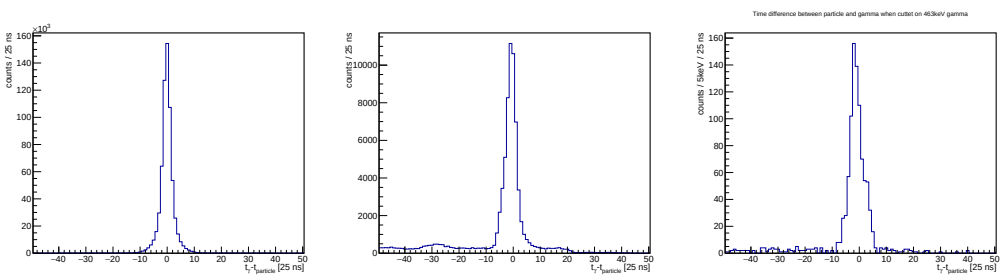

(a) Time difference between two γ-rays within one EBIS-gate.

(b) Prompt time difference spectrum between a γ-ray and a particle.

(c) Prompt time difference spectrum between a γ-ray and a particle, when cutted on the 463 keV transition.

Figure F.10: Various time difference spectra between particles and γ-rays.

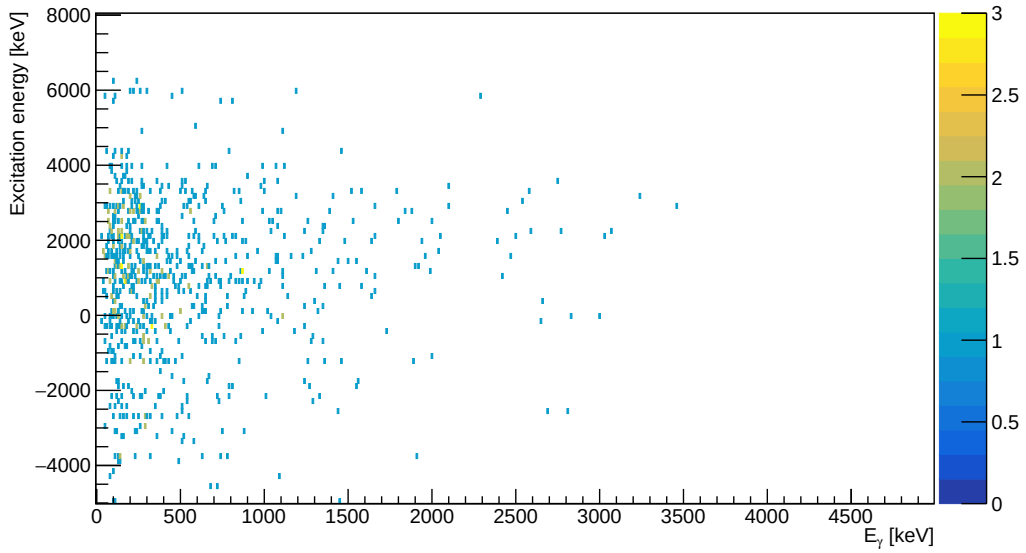

Figure F.11: Excitation energy versus γ-energy spectrum, when naively assigning all particles in the backward barrel detectors to be transfer protons from the ^{133}Xe reaction. Not the absence of the 463.2 keV γ-ray.

Bibliography

[1] B. P. Abbott et al. Gw170817: Observation of gravitational waves from a binary neutron star inspiral. *Phys. Rev. Lett.*, 119:161101, Oct 2017.

[2] W. Adam et al. P-type silicon strip sensors for the new CMS tracker at HL-LHC. *Journal of Instrumentation*, 12(06):P06018–P06018, jun 2017.

[3] J. Adamczewski-Musch et al. Data acquisition backbone core, user manual, programmer manual. Technical report, 2009. available via: https://web-docs.gsi.de/ dabc/doc/manuals/dabc_v1.0.01.pdf.

[4] S. Agostinelli et al. Geant4—a simulation toolkit. *Nuclear Instruments and Methods in Physics Research Section A: Accelerators, Spectrometers, Detectors and Associated Equipment*, 506(3):250 – 303, 2003.

[5] A. N. Andreyev et al. Nuclear fission: a review of experimental advances and phenomenology. *Reports on Progress in Physics*, 81(1):016301, nov 2017.

[6] ANL. Atlas 2018 strategic plan. `https://www.anl.gov/atlas/reference/atlas-2018-strategic-plan`, 2018. [Online; accessed 07-January-2020].

[7] S. Anvar et al. Aget, the get front-end asic, for the readout of the time projection chambers used in nuclear physic experiments. In *2011 IEEE Nuclear Science Symposium Conference Record*, pages 745–749, Oct 2011.

[8] C. Arlandini et al. Neutron capture in low-mass asymptotic giant branch stars: Cross sections and abundance signatures. *The Astrophysical Journal*, 525(2):886–900, nov 1999.

[9] M. Arnould et al. The r-process of stellar nucleosynthesis: Astrophysics and nuclear physics achievements and mysteries. *Physics Reports*, 450(4):97 – 213, 2007.

[10] N. Austern et al. Continuum-discretized coupled-channels calculations for three-body models of deuteron-nucleus reactions. *Physics Reports*, 154(3):125 – 204, 1987.

[11] D. W. Bardayan. Transfer reactions in nuclear astrophysics. *Journal of Physics G: Nuclear and Particle Physics*, 43(4):043001, feb 2016.

[12] M.L. Bellac et al. *Quantum Physics*. Cambridge University Press, 2011.

[13] L. Bianchi et al. Speg: An energy loss spectrometer for ganil. *Nuclear Instruments and Methods in Physics Research Section A: Accelerators, Spectrometers, Detectors and Associated Equipment*, 276(3):509 – 520, 1989.

[14] V. Bildstein et al. T-rex. *The European Physical Journal A*, 48(6):85, Jun 2012.

[15] Y. Blumenfeld et al. Facilities and methods for radioactive ion beam production. *Physica Scripta*, T152:014023, jan 2013.

[16] J. Borg et al. SKIROC2_CMS an ASIC for testing CMS HGCAL. *Journal of Instrumentation*, 12(02):C02019–C02019, feb 2017.

[17] M. J. G. Borge et al. ISOLDE past, present and future. *Journal of Physics G: Nuclear and Particle Physics*, 44(4):044011, mar 2017.

[18] M. J. G. Borge and others. Hie-isolde, the project and the physics opportunities. *The European Physical Journal A*, 52(11):334, Nov 2016.

[19] R. Brun et al. Root - an object oriented data analysis framework. *Nuclear Instruments and Methods in Physics Research Section A: Accelerators, Spectrometers, Detectors and Associated Equipment*, 389(1):81 – 86, 1997. New Computing Techniques in Physics Research V.

[20] S. Callier. Skiroc2 an integrated readout chip for a high granularity electromagnetic calorimeter. Technical report, OMEGA microelectronics group, LLR, Palaiseau, 2015. available via: https://indico.in2p3.fr/event/11997/attachments/6162/7648/SC_Skiroc2_seminaire_LLR_20150928.pdf.

[21] S. Callier. Technical documents. personal communication, 2016.

[22] S. Callier et al. SKIROC2, front end chip designed to readout the electromagnetic CALorimeter at the ILC. *Journal of Instrumentation*, 6(12):C12040–C12040, dec 2011.

[23] W. N. Catford. *The Euroschool on Exotic Beams*, volume 4. Springer, Berlin, Heidelberg, 1 edition, 2014.

[24] Wilton N. Catford. *What Can We Learn from Transfer, and How Is Best to Do It?*, pages 67–122. Springer Berlin Heidelberg, Berlin, Heidelberg, 2014.

[25] R. Catherall et al. An overview of the hie-isolde design study. *Nuclear Instruments and Methods in Physics Research Section B: Beam Interactions with Materials and Atoms*, 317:204 – 207, 2013. XVIth International Conference on Electro-Magnetic Isotope Separators and Techniques Related to their Applications, December 2–7, 2012 at Matsue, Japan.

[26] CERN. Hie-isolde high intensity and energy upgrade. `https://hie-isolde-project.web.cern.ch`, 2020. [Online; accessed 07-January-2020].

[27] J. Diriken et al. Experimental study of the ^{66}Ni$(d,\ p)^{67}$Ni one-neutron transfer reaction. *Phys. Rev. C*, 91:054321, May 2015.

[28] F. Dulucq. Presentation of the front-end "roc" chips readout for ecal and hcal ilc calorimeters. Technical report, LAL, IN2P3-CNRS, Orsay, France, 2010. available via: https://www.eudet.org/e26/e28/index_eng.html.

[29] C. L. Dunford. Plots produced using the online service retrieval code package, 2019. available via https://www.nndc.bnl.gov/nudat2/replotband.jsp.

[30] C. L. Dunford. Data retrieved from, 2020. available via https://www.nndc.bnl.gov/.

[31] J. E. Escher et al. Cross sections for neutron capture from surrogate measurements: An examination of weisskopf-ewing and ratio approximations. *Phys. Rev. C*, 81:024612, Feb 2010.

[32] L. D. Faddeev. Scattering theory for a three particle system. *Sov. Phys. JETP*, 12:1014–1019, 1961. [Zh. Eksp. Teor. Fiz.39,1459(1960)].

[33] FAIR. Fair - the new large scale accelerator facility in europe. `https://fair-center.eu/index.php?id=1`, 2020. [Online; accessed 07-January-2020].

[34] H. Feshbach. *Theoretical Nuclear Physics: Nuclear Reactions*. Number Bd. 2 in Wiley classics library. John Wiley & Sons, Incorporated, 1992.

[35] A. Gavron. Statistical model calculations in heavy ion reactions. *Phys. Rev. C*, 21:230–236, Jan 1980.

[36] G. Giacomini. *Noise Characterization of Silicon Strip Detectors, Comparison of Sensors with and without Integrated JFET Source-Follower*. PhD thesis, Università degli studi di Trieste DEGLI STUDI DI TRIESTE, Fisica Nucleare e Subnucleare, 2007.

[37] Mesytec Gmbh. Readout electronics for nuclear physics experiments. Technical report. available via: https://www.mesytec.com/products/nuclear-physics.html.

[38] M. Grieser et al. Storage ring at hie-isolde. *The European Physical Journal Special Topics*, 207(1):1–117, May 2012.

[39] J. Gómez Camacho et al. A pedestrian approach to the theory of transfer reactions: Application to weakly-bound and unbound exotic nuclei. *Lecture Notes in Physics*, 879, 11 2013.

[40] G. Hagen et al. Structure of ^{78}Ni from first-principles computations. *Phys. Rev. Lett.*, 117:172501, Oct 2016.

[41] F.G. Hartjes. Moisture sensitivity of ac-coupled silicon strip sensors. *Nuclear Instruments and Methods in Physics Research Section A: Accelerators, Spectrometers, Detectors and Associated Equipment*, 552(1):168 – 175, 2005. Proceedings of the 5th International Conference on Radiation Effects on Semiconductor Materials, Detectors and Devices.

[42] S. Hellgartner. Documentation of the calibration of the t-rex detectors and of miniball. Technical report, 2012. contact: stefanie.hellgartnertum.de.

[43] S. Hellgartner. Details on the ^{74}zn experiment. private communiation, 11 2014.

[44] S. Hellgartner. *Probing Nuclear Shell Structure beyond the $N = 40$ Subshell using Multiple Coulomb Excitation and Transfer Experiments*. PhD thesis, Technische Universität München, Physik-Department, Lehrstuhl E12 für Experimentalphysik, Physik der Hadronen und Kerne, 11 2015. available at: http://mediatum.ub.tum.de?id=1277804.

[45] C. J. Horowitz et al. r-process nucleosynthesis: connecting rare-isotope beam facilities with the cosmos. *Journal of Physics G: Nuclear and Particle Physics*, 46(8):083001, jul 2019.

[46] K. L. Jones et al. The magic nature of 132sn explored through the single-particle states of 133sn. *Nature*, 465(7297):454–457, 2010.

[47] Y. Kadi et al. Hie-isolde: Technical design report for the energy upgrade. Technical Report 1, CERN, Geneva, 2018. available via: https//doi.org/10.23731/CYRM-2018-001.

[48] L. Kaya et al. Millisecond $23/2^+$ isomers in the $n = 79$ isotones ^{133}Xe and ^{135}Ba. *Phys. Rev. C*, 98:054312, Nov 2018.

[49] G. Korcyl et al. A users guide to the trb3 and fpga-tdc based platforms. Technical report, 2019. available via: http://jspc29.x-matter.uni-frankfurt.de/docu/trb3docu.pdf.

[50] G. Kraus et al. Investigation of the (d, p)-reaction on136, 132xe in inverse kinematics. *Zeitschrift für Physik A Hadrons and Nuclei*, 340(3):339–340, Sep 1991.

[51] T. Kröll et al. Proposal to the isolde and neutron time-of-flight committee - first spectroscopy of the r-process nucleus ^{135}sn. Technical report, 2018. available via: https://cds.cern.ch/record/2299693/files/INTC-P-539.pdf.

[52] J. Lawrence. Apv25-s1 user guideversion 2.2, 2001. available via https://cds.cern.ch/record/1069892/files/cer-002725643.pdf.

[53] C. Li et al. Measurement of the ^{2}H$(d, p)^3$H reaction at astrophysical energies via the trojan-horse method. *Phys. Rev. C*, 92:025805, Aug 2015.

[54] C. Li et al. Measurement of the ^{2}H$(d, p)^3$H reaction at astrophysical energies via the trojan-horse method. *Phys. Rev. C*, 92:025805, Aug 2015.

[55] M. Lindroos et al. Hie-isolde: the technical options. Technical Report 1, CERN, Geneva, 2006. available via: https://cds.cern.ch/record/1001782/files/CERN-2006-013.pdf.

[56] XIA LLC. User's manual - digital gamma finder (dgf) dgf-4c revision f. Technical report, 2009. available via: https://www.xia.com/Manuals/DGF_UserManual.pdf.

[57] T. Lönnroth et al. One- and three-quasiparticle states in127,129,131,133xe and their coexistence with band structures. *Physica Scripta*, 27(4):228–240, apr 1983.

[58] G. Lutz. *Semiconductor Radiation Detectors*. Springer, Berlin, Heidelberg, 2 edition, 2007.

[59] G. J. Mathews et al. Introduction to big bang nucleosynthesis and modern cosmology. *International Journal of Modern Physics E*, 26(08):1741001, Aug 2017.

[60] T. Mayer-Kuckuk. *Kernphysik: Eine Einführung*. Teubner-Studienbücher : Physik. Vieweg+Teubner Verlag, 2002.

[61] P. W. Merrill. Spectroscopic observations of stars of class s. *Astrophysical Journal*, 116:21 – 26, July 1952.

[62] M. Cheikh Mhamed. Report on r&d on radioactive plasma ion sources. Technical Report D14.2, ENSAR2, Project Ref. No. 654002, 2 2019. available at: http://www.ensarfp7.eu/.

[63] J. Michel et al. Electronics for the RICH detectors of the HADES and CBM experiments. *Journal of Instrumentation*, 12(01):C01072–C01072, jan 2017.

[64] J. Michel et al. A users guide to the hades daq system. Technical report, 2019. available via: http://jspc29.x-matter.uni-frankfurt.de/docu/trbnetdocu.pdf.

[65] MLL. Meier-leibnitz-laboratorium für kern-, teilchen-, und beschleunigerphysik, 2019. available via https://www.mll-muenchen.de/ueber_uns/index.html.

[66] David J. Morrissey and Brad M. Sherrill. *In-Flight Separation of Projectile Fragments*, pages 113–135. Springer Berlin Heidelberg, Berlin, Heidelberg, 2004.

[67] MSU. Facility for rare isotope beams. `https://frib.msu.edu`, 2020. [Online; accessed 07-January-2020].

[68] S.F. MUGHABGHAB et al. I - thermal cross sections. In S.F. MUGHABGHAB et al., editors, *Neutron Resonance Parameters and Thermal Cross Sections*, pages 1 – 18. Academic Press, 1981.

[69] M. R. Mumpower et al. The impact of individual nuclear properties on *r*-process nucleosynthesis. *Prog. Part. Nucl. Phys.*, 86:86–126, 2016. [Erratum: Prog. Part. Nucl. Phys.87,116(2016)].

[70] Ortec. Partially depleted silicon surface barrier detector, 2019. available via https://www.ortec-online.com/-/media/ametekortec/brochures/a-series.pdf.

[71] R. B. Owen et al. One and two dimensional position sensing semiconductor detectors. *IEEE Transactions on Nuclear Science*, 15(3):290–303, June 1968.

[72] A. Prochazka et al. Online energy loss and slowing down calculator, interface to catima library, 2019. available via https://www.isotopea.com/webatima/ or via https://web-docs.gsi.de/ weick/atima/.

[73] V. Radeka. Low-noise techniques in detectors. *Annual Review of Nuclear and Particle Science*, 38(1):217–277, 1988.

[74] A. Ratkiewicz et al. Towards neutron capture on exotic nuclei: Demonstrating $(d, p\gamma)$ as a surrogate reaction for (n, γ). *Phys. Rev. Lett.*, 122:052502, Feb 2019.

[75] T. Rauscher et al. Constraining the astrophysical origin of the p-nuclei through nuclear physics and meteoritic data. *Reports on Progress in Physics*, 76(6):066201, may 2013.

[76] K. Riisager et al. Hie-isolde: the scientific opportunities. Technical Report 2, CERN, Geneva, 2007. available via: https://cds.cern.ch/record/1078363/files/HIE-ISOLDE-PROJECT-Note-0002.pdf.

[77] D. Rosiak et al. Enhanced quadrupole and octupole strength in doubly magic ^{132}Sn. *Phys. Rev. Lett.*, 121:252501, Dec 2018.

[78] G.R. Satchler. *Direct Nuclear Reactions*. International series of monographs on physics. Clarendon Press, 1983.

[79] H. Schatz. Trends in nuclear astrophysics. *Journal of Physics G: Nuclear and Particle Physics*, 43(6):064001, may 2016.

[80] J. Schiffer. Transfer reactions: Probing another aspect of nuclear structure. `https://www.phy.ornl.gov/workshops/transfer/docs/jps{_}transfer.pdf`, 2002. [Online; accessed 22-December-2019].

[81] C. Seiffert. *Production of radioactive molecular beams for CERN-ISOLDE*. PhD thesis, Technische Universität Darmstadt, Fachbereich Physik, Institut für Kernphysik, AG Kröll, 6 2015. available at: https://tuprints.ulb.tu-darmstadt.de/id/eprint/4599.

[82] R. Shurtleff et al. The most tightly bound nucleus. *American Journal of Physics*, 57(6):552–552, 1989.

[83] M. S. Smith et al. Nuclear astrophysics measurements with radioactive beams. *Annual Review of Nuclear and Particle Science*, 51(1):91–130, 2001.

[84] R. Surman et al. Neutron capture rates near $a = 130$ that effect a global change to the *r*-process abundance distribution. *Phys. Rev. C*, 79:045809, Apr 2009.

[85] Dassault Systems. Solidworks, 2020. available via https://www.solidworks.com.

[86] I. J. Thompson. Coupled reaction channels calculations in nuclear physics. *Computer Physics Reports*, 7(4):167 – 212, 1988.

[87] I. J. Thompson et al. Face: a tool for three body faddeev calculations with core excitation. *Computer Physics Communications*, 161(1):87 – 107, 2004.

[88] I. J. Thompson et al. *Nuclear Reactions for Astrophysics: Principles, Calculation and Applications of Low-Energy Reactions*. Cambridge University Press, 2009.

[89] M. Traxler et al. A compact system for high precision time measurements (< 14 ps RMS) and integrated data acquisition for a large number of channels. *Journal of Instrumentation*, 6(12):C12004–C12004, dec 2011.

[90] TRIUMF. The advanced rare isotope laboratory. `https://www.triumf.ca/ariel`, 2020. [Online; accessed 07-January-2020].

[91] A. Tumino et al. Nuclear astrophysics with the trojan horse method. *Journal of Physics: Conference Series*, 665:012009, jan 2016.

[92] TWEEP 2016 - Topical Workshop on Electronics for Particle Physics. *SKIROC2_CMS: an ASIC for testing CMS HGCAL*. C. de la Taille, 2016.

[93] N. Warr. Ionisation chamber. Technical report, 2017. available via: https://www.ikp.uni-koeln.de/ warr/doc/ion_chamber.pdf.

[94] N. Warr et al. The miniball spectrometer. *The European Physical Journal A*, 49(3):40, Mar 2013.

[95] Y. X. Watanabe et al. Pathway for the production of neutron-rich isotopes around the $n = 126$ shell closure. *Phys. Rev. Lett.*, 115:172503, Oct 2015.

[96] D. Watson et al. Identification of strontium in the merger of two neutron stars. *Nature*, 574(7779):497–500, 2019.

[97] F. Wenander. Discussion on the ^{132}ba contamination during the ^{133}xe experiment. private communiation, 02 2020.

[98] L. Werner. Details on the frmii spectra. private communiation, 03 2019.

[99] T. I. Westgaard et al. Radiation hardness of punch-through and fet biased silicon microstrip detectors. *Nuclear Instruments and Methods in Physics Research Section A: Accelerators, Spectrometers, Detectors and Associated Equipment*, 377(2):429 – 434, 1996. Proceedings of the Seventh European Symposium on Semiconductor.

[100] K. Wimmer. Nucleon transfer reactions with radioactive beams. *Journal of Physics G: Nuclear and Particle Physics*, 45(3):033002, feb 2018.

[101] K. Wimmer et al. Discovery of the shape coexisting 0^+ state in ^{32}Mg by a two neutron transfer reaction. *Phys. Rev. Lett.*, 105:252501, Dec 2010.

[102] T. Wittig. Details on the sims measurements. private communiation, CiS Forschungsinstitut für Mikrosensorik GmbH, 11 2019.

[103] S. S. M. Wong. *Introductory Nuclear Physics*, volume 1. WILEY-VCH, Weinheim, 2 edition, 2004.

[104] A.H. Wuosmaa et al. A solenoidal spectrometer for reactions in inverse kinematics. *Nuclear Instruments and Methods in Physics Research Section A: Accelerators, Spectrometers, Detectors and Associated Equipment*, 580(3):1290 – 1300, 2007.

[105] A. Yoshida et al. Beam spot temperature monitoring on production target of bigrios seperator. `http://intds.org/TALKS-2010/yoshida-intds2010a.pdf`, 2010. [Online; accessed 20-September-2019].

[106] J. F. Ziegler et al. Srim – the stopping and range of ions in matter (2010). *Nuclear Instruments and Methods in Physics Research Section B: Beam Interactions with Materials and Atoms*, 268(11):1818 – 1823, 2010. 19th International Conference on Ion Beam Analysis.